

Assessment of Non-Contact Induction Heating Characteristics of Metallic Biomaterials

A master thesis

By

T.P. Hartsuijker

4653912

in partial fulfillment of the requirements for the degree of

Master of Science
in Biomedical Engineering

at the Delft University of Technology



Supervisors:

Dr.ir. I. Apachitei
Ir. M. Šalandová,
Prof.dr.ir. L. Abelman,

TU Delft

Keywords: magnetic hyperthermia, biomaterials, induction heating, implant-associated infections, biofilm

Table of Contents

Table of Contents.....	3
Abbreviations & Symbols.....	5
Abbreviations.....	5
Material quantities.....	5
Magnetic / Electric field quantities	5
Constants.....	5
Abstract.....	6
1 Introduction	7
1.1 General Background	7
1.2 Thesis Goal & Research Question.....	9
1.3 Theoretical Background.....	11
Electromagnetism Theory	11
Material Science Theory	12
Side Effects During Induction Heating.....	15
2 Methods & Materials.....	17
2.1 Phase I: IH trials	17
Specimen Geometry Selection.....	17
Material Selection and Preparation	17
Material Properties Analysis	18
Experimental Setup for IH	19
2.2 Phase II: Analytical Modeling.....	21
2.3 Phase III: Targeted IH.....	23
Specimen Geometry and Material Selection	23
Experimental Setup.....	23
3 Results.....	25
3.1 Phase I: Preparatory Research.....	25
Chemical Composition Analysis of the Assessed Materials	25
Physical Properties of the Assessed Materials	25
Induction Trials	27
Statistical analysis.....	29
3.2 Phase II: Analytical Modeling.....	30
IH Predictions Through the Analytical Model.....	30
FEM Analysis	32
Evaluation of the Analytical Model	33
3.3 Phase III: Targeted IH.....	38
4 Discussion	40
4.1 Phase II: Induction Trials.....	40
Material Properties Analysis	40
IH Experiments.....	40

Statistical Analysis.....	42
4.2 Phase II: Analytical Modeling	43
4.3 Phase III: Targeted IH	45
5 Conclusion	47
6 Recommendation	48
7 Acknowledgements	49
References.....	50
8. Appendix.....	54
Appendix I: MagneTherm datasheet.....	54
Appendix II: Planar Coil.....	55
Appendix III: Safety Protocol	58
Appendix IV: Appendix IV: Step-By-Step Derivation of the Analytical Model "Model 1" ..	80
Appendix V: Analytical "Model 1" Python Code	83
Appendix VI: FreeFem++ Code.....	85
Appendix VII: Source Code Calculating and Plotting Vector Potential "Model 1"	89
Appendix VIII: Source Code Calculating and Plotting the Vector Potential of Various Models.....	92

Abbreviations & Symbols

Abbreviations

Definition	Abbreviation
Alternating Current	AC
Alternating Magnetic Field	AMF
Demineralized	DM
Extracellular Polymeric Substance	EPS
Implant-Associated Infections	IAIs
IH	IH
Magnetic Field Hyperthermia	MFH
Magnetic Nanoparticles	MNPs

Material quantities

Physical properties	Symbol	Unit
Density	ρ	$kg \cdot m^{-3}$
Electromagnetic properties		
Electrical conductivity	σ	$\Omega^{-1} \cdot m^{-1}$ or $S \cdot m^{-1}$
Electrical resistivity	$\rho = \sigma^{-1}$	$\Omega \cdot m$
Magnetic properties		
Relative magnetic permeability	μ_r	
Thermal properties		
Thermal conductivity	κ	$W \cdot m^{-1} \cdot K^{-1}$
Specific heat	C	$J \cdot kg^{-1} \cdot K^{-1}$

Magnetic / Electric field quantities

	Symbol	Unit
Magnetic field amplitude	B_0	$kg \ A^{-1} \cdot s^{-2}$ or T
Magnetic field (vector)	\mathbf{B}	T
Frequency	ω	rad
Frequency	f	Hz
Electric field (vector)	\mathbf{E}	$V \cdot m^{-1}$
Power	P	J
Current	I	A
Resistance	R	Ω
Magnetic permeability	μ	$H \cdot m^{-1}$

Constants

	Symbol	Unit
Electromagnetic properties		
Permeability of free space	μ_0	$4\pi \cdot 10^{-7}$
Permittivity of free space	ϵ_0	$8.85418782 \cdot 10^{-12} \ m^{-3} kg^{-1} s^4 A^2$

Abstract

Implant-associated infections are a severe concern affecting 1 – 3 % of patients undergoing primary joint arthroplasty [1]. Magnetic hyperthermia, which can be non-invasively induced by applying an alternating magnetic field (AMF) around a metallic implant, is a new approach with great potential. This research project explores the application of non-contact induction heating (IH) of metallic implants in orthopedic surgery. It focuses on the heating behavior of paramagnetic biomaterials relevant to this application in alternating magnetic fields.

Empirical testing plays an inherent role in research. However, it is often very time-consuming, especially when assessing many specimens. With *in silico* simulations, data can be yielded much faster. An analytical model simulating the heating dynamics of paramagnetic materials in the AMF was constructed to provide a tool for faster suitability assessment of metallic biomaterials for magnetic hyperthermia. The model was then compared with empirical data obtained in a controlled environment.

The empirical data showed a quadratically increasing temperature rise with the field amplitude and a linearly growing temperature rise with the frequency. The constructed analytical model confirmed that the heat generated in the materials increases quadratically with the increasing AMF amplitude. Additionally, increasing the frequency of the AMF also affects heat generation. The model predicted different trends depending on what domain a material is assigned to. However, empirical data indicates a consistent linear relationship across several assessed frequencies and materials.

Based on the obtained knowledge of the material's behavior in AMF, a new hip implant intended for magnetic hyperthermia treatment was designed. It utilized a coating on the neck of the femoral stem, designed to enable targeted IH, particularly to regions most susceptible to bacterial infections. The experiment featured a multi-material specimen consisting of Ti Gr. 23 and ST. 37, which mimicked the neck of a hip implant, the proof of concept was successfully demonstrated, showing a significant temperature increase for specimens with coating compared to the ones without at high magnetic field strength and frequency. However, targeted IH was not detected.

Better computational models can further explore the obtained knowledge, and the proof-of-concept can be further tested to investigate its contribution to treating resistant bacterial biofilms.

1 Introduction

1.1 General Background

Yearly, millions of people receive metallic prosthetic joint replacements as a result of skeletal fractures, osteoarthritis, or other injuries [2]. In the Netherlands alone, over 80.000 joint arthroplasties were performed in 2022 [3]. Although performed under strict safety measures and having a relatively low risk of failure, infections still occur in 1 – 3 % of primary arthroplasties and up to 30 % of orthopedic trauma implants [1], [4], [5]. Due to the increasing demand for receiving implants, the number of people suffering from implant-associated infection (IAI) is rising as well.

Most IAIs are caused by the *Staphylococci* family, most commonly by *Staphylococcus aureus* and *Staphylococcus epidermidis*. Together, they account for two-thirds of infection isolates [6]. In addition, *Pseudomonas aeruginosa* has made a significant contribution to IAIs as well [6]. These infections usually begin with planktonic cells that can migrate through the body in various ways until they adhere to an implant and form a biofilm. This biofilm consists of complex bacterial clusters embedded in an extracellular polymeric substance (EPS), which confers enhanced mechanical stability and protection [7]. The EPS effectively blocks the penetration of antimicrobial agents, making the biofilm substantially more resistant to treatment than individual bacterial cells and requiring potent antibiotics. In cases involving antibiotic-resistant bacterial strains, clinicians face an even more significant challenge [8]. Mainly, *Staphylococcus aureus* is well known for having developed resistance to multiple antibiotics [9]. Epidemics of infections, especially those caused by Methicillin-resistant *Staphylococcus aureus* (MRSA), often begin with a few resilient strains and can spread widely, with MRSA now being a worldwide issue due to its resistance to several common antibiotics [9].

Given these difficulties, there is an active pursuit of alternative methods to treat IAIs, a field that has become increasingly vital in medical research. A novel treatment of IAIs may employ magnetic field hyperthermia (MFH), a technique already established as a treatment method in oncology. In MFH cancer treatments, magnetic nanoparticles (MNPs) are administered into tumor regions. Subsequently, these particles are heated by exposure to an alternating magnetic field (AMF). This induces a rise in temperature within the tumor tissue and affects vital molecules of the cancerous cells, leading to their denaturation and ultimately resulting in cell death [10].

MFH approach can be directly applied to metallic orthopedic implants, which inherently heat up during exposure to AMF [11]. Heat can disrupt biofilms and eliminate bacteria similarly as it does tumorous cells, as has been shown in several studies [11], [12], [13], [14], [15], [16], [17]. These studies utilized non-contact induction heating (IH) to directly increase the surface temperature of metallic implants, effectively breaking down biofilms and eliminating the bacteria attached to the implants. The technique could, therefore, provide additional means for treating biofilm and could be used in combination therapies together with antibiotics to improve the treatment outcomes in challenging cases of IAIs [11], [13], [14], [15].

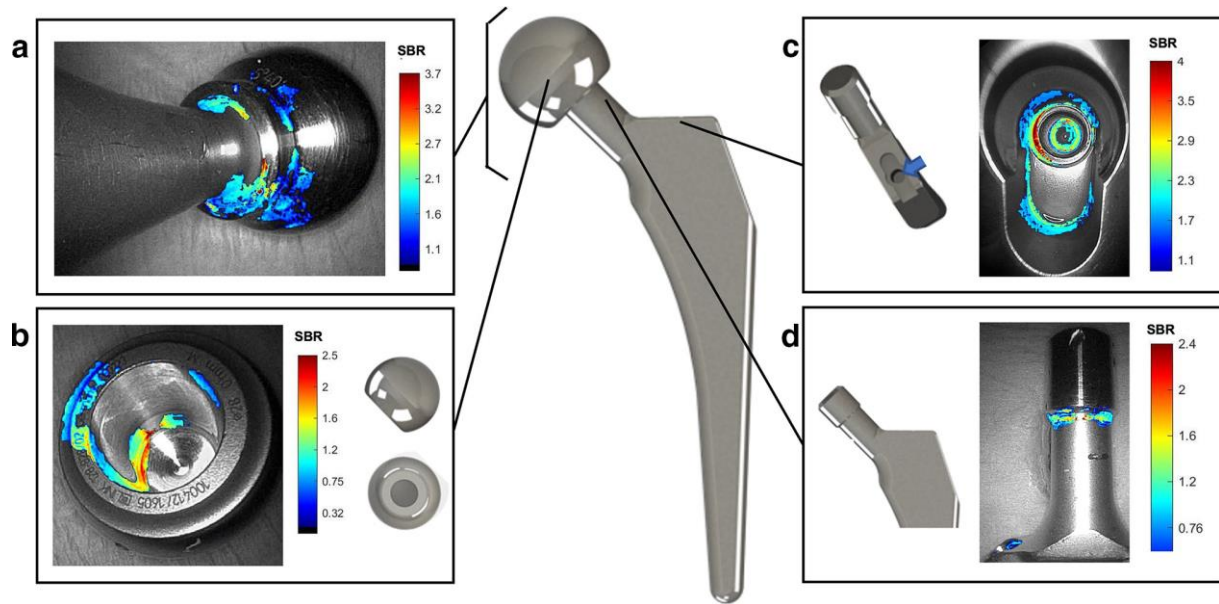


Figure 1.1 Infection regions on femoral component of a hip implant visualized with pseudo fluorescence imaging [18].

If proven sufficiently effective alone, MFH treatments could also be used to eliminate biofilms in regions that systemically administered antibiotics cannot reach due to no contact with bone tissue, such as the neck of a hip implant. Research by Welling *et al.* [18] demonstrated that biofilms are more likely to develop in specific regions of artificial hips, such as the transition zone between the head and neck and within the screw holes of the femoral component, shown in Figure 1.1. Therefore, incorporating an induction-susceptible material into these critical areas and using AMF to induce hyperthermia may represent a new treatment approach.

Little is reported, however, in the literature about the heating behavior of orthopedic biomaterials in AMF. Large-scale experimental testing of various biomaterials can be very time-consuming, especially when comparing several specimens, offering an opportunity window for *in silico* studies. Although literature studying the heating behavior of orthopedic implants in AMF through computational finite element method (FEM) exists [17], these models are often not validated, and their analytical foundations yielding the output are missing. In addition, FEM models do not give insight into how parameters exactly influence the thermal response of the implant. Therefore, analytical models validated by empirical data, which would then accelerate the selection of biomaterials, are stringently needed. Moreover, such models would also strengthen the understanding of the parameters relevant to MFH and thereby assist in optimizing the method for clinical use.

1.2 Thesis Goal & Research Question

This study aims to identify the influence of material properties and AMF parameters on the heating of biomaterials when exposed to AMF by developing an analytical model. An analytical approach applied to a simple geometry is preferred over a complex geometry solved in a FEM model. The analytical solution offers better control over the parameters affecting the thermal response and avoids complex calculations inherent in FEM. This understanding will then be used to optimize implant IH by selecting well responsive materials and appropriate field parameters, thereby increasing the efficiency of treatments and reducing adverse effects, such as tissue damage. Therefore, the following research question was formulated:

"How can magnetic field hyperthermia be applied to metallic implants to treat and prevent implant-associated infections?"

The primary research question will be addressed by exploring the following sub-questions:

- What is the analytical solution describing the heating response of an implant during IH in AMF?
- What is the relationship between the heating responses of various (metallic) biomaterials and the AMF parameters (frequency and amplitude)?
- What parameters and materials should be selected for MFH treatment for high infection-risk areas of orthopedic implants?

The thesis is divided into three phases (Figure 1.2). In Phase I, the experimental groundwork is laid by defining the experimental setup and collecting empirical data on the behavior of different materials exposed to AMF under different magnetic field amplitudes and frequencies.

In Phase II, the focus shifts to building and validating the analytical model. The main goal is to deepen the understanding of how magnetic field strength and frequency influence the IH process. This phase is crucial for identifying key material properties variables (*e.g.*, electrical resistivity) and assessing their effects, providing vital insights to refine the model further.

Phase III of the project extends the groundwork laid in the earlier phases, shifting focus to clinical application. A new design is proposed, introducing an implant equipped with an iron coating on the neck of the femoral stem, designed to enable targeted IH. It aims to deliver magnetic field hyperthermia to the most susceptible bacterial infection region. A prototype mimicking the implant's neck was constructed and tested for a proof-of-concept assessment. This is critical for demonstrating that the theoretical models developed in Phase II can be successfully used for extensive scale testing of biomaterials in AMF. By implementing a targeted heating mechanism within the hip implant, the project seeks to offer a novel therapeutic approach that could improve post-surgical outcomes and increase the overall success of hip replacements.

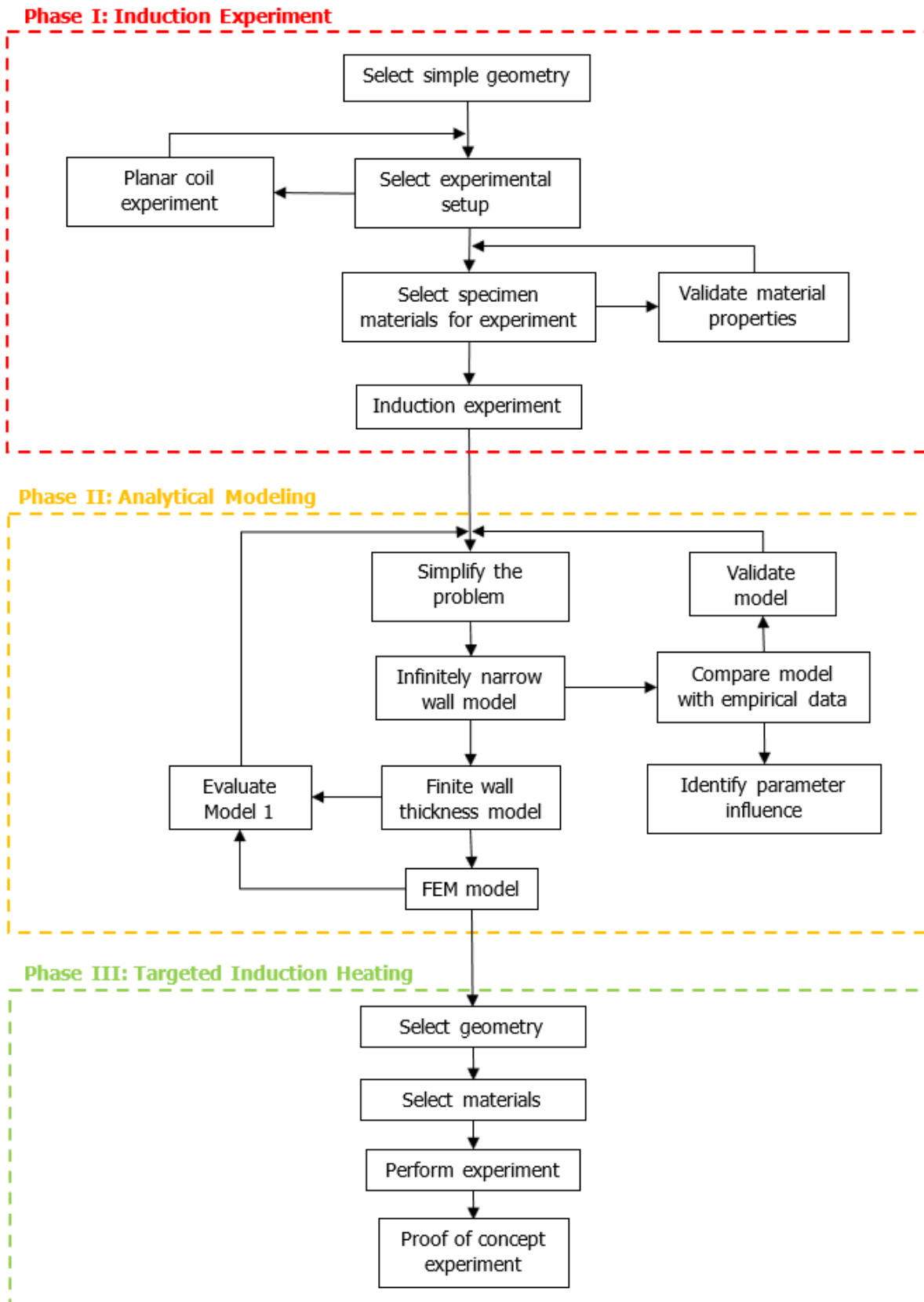


Figure 1.2 Research flowchart describing the individual phases of the research: Phase I) Setup selection and collection of experimental data; Phase II) Construction of an analytical model and its validation with the experimental data from Phase I; Phase III) Application of the model in the assessment of proposed implant design.

1.3 Theoretical Background

Magnetic field hyperthermia is a form of IH, which is a multifaceted process involving a combination of electromagnetism, heat transfer, and material science, each contributing to the performance [19]. The upcoming section aims to provide essential insights into electromagnetic phenomena and the influence of material properties, laying the groundwork for understanding IH simulations.

Electromagnetism Theory

Maxwell's equations lay the electromagnetic foundation for the IH process [20]. They describe how an alternating current (AC) in an induction coil generates a fluctuating magnetic field, a principle central to this technology. While all of Maxwell's equations contribute to our understanding of IH, the third equation is primarily used in this study to construct the analytical model. Nonetheless, a brief overview of the other equations is presented for completeness.

Gaus's law (Equation 1.1) postulates that electric charges produce electric fields,

$$\nabla \cdot \mathbf{E} = \frac{\rho}{\varepsilon_0} \quad (1.1)$$

Gaus's law for magnetism (Equation 1.2) clarifies that magnetic monopoles do not exist, indicating the absence of isolated magnetic charges,

$$\nabla \cdot \mathbf{B} = 0 \quad (1.2)$$

Faraday's law (Equation 1.3) describes how a varying magnetic field induces a circulating electric field and vice versa,

$$\nabla \times \mathbf{E} = \frac{\delta \mathbf{B}}{\delta t} \quad (1.3)$$

Ampère's law with Maxwell's correction (Equation 1.4) reveals that magnetic fields are generated by electric currents and changing electric fields,

$$\nabla \times \mathbf{B} = \mu_0 \mathbf{J} + \mu_0 \varepsilon_0 \frac{\delta \mathbf{E}}{\delta t} \quad (1.4)$$

where, \mathbf{E} is the electric field, ρ is the electric charge density, ε_0 is the permittivity of free space, \mathbf{B} is the magnetic field, \mathbf{J} is the current density and μ_0 is the permeability of free space, t represents time. This framework underpins the theoretical analysis of IH mechanisms explored in this study.

IH involves induced current in a conductor via an inductor [19]. The efficiency of the IH process largely depends on the uniformity of the magnetic field generated within the workpiece. This uniformity is influenced by the dimensions and material properties of the coil (inductor) and the workpiece (conductor). Consequently, the induced current may not be uniformly distributed across the workpiece's surface, leading to uneven heating patterns on the workpiece's surface [19]. When a workpiece is placed near this coil, it is subjected to the magnetic field, inducing currents within it. The induced heating of the workpiece is primarily driven by two mechanisms: eddy current losses and magnetic hysteresis [19]. Eddy current heating is the predominant mechanism of the two. They can be induced in any conductive material, while hysteresis losses, on the other hand, are relevant only for ferromagnetic materials. The coil's magnetic field induces Eddy currents in the workpiece, which have the same frequency as the coil current but flow in the opposite direction. The Eddy currents generate heat due to the material's resistance [21]. Heat is generated by the eddy currents due to the material's resistance (*i.e.*, resistive loss), given by Equation 1.5,

$$P = I^2 \cdot R \quad (1.5)$$

where P is the generated power, I is the current, and R is the resistance.

Material Science Theory

In this thesis, attention is dedicated mainly to the electromagnetic properties of materials, especially magnetic susceptibility, electrical resistivity, and magnetic permeability. These represent the most critical properties affecting both the electromagnetic attributes of metals and the IH process. The most relevant material properties are highlighted and explained in the upcoming paragraphs. These properties are crucial for predicting and explaining why one material might react differently from another material [19].

Magnetic susceptibility

Magnetic susceptibility indicates how a material responds to an external magnetic field. Three primary types have been identified: ferromagnets, diamagnets, and paramagnets, each displaying unique behaviors [22]. An overview of the magnetic susceptibility and the alignment of the magnetic domains is given in Figure 1.3.

This property is a reason why hysteresis loss takes place only in ferromagnets. Due to the permanent magnetization of these materials, the domains in a ferromagnetic material realign with the magnetic field, leading to energy dissipation in the form of resistive losses, which manifest as heat within the material [21]. Ferromagnetic materials exhibit a non-linear relationship between B and H , characterized by the hysteresis loop shown in Figure 1.4. This loop represents the energy lost during one complete cycle per unit volume of the material. This loss is significant only in ferromagnetic materials due to their domain structure and the substantial internal resistance to domain movement [23].

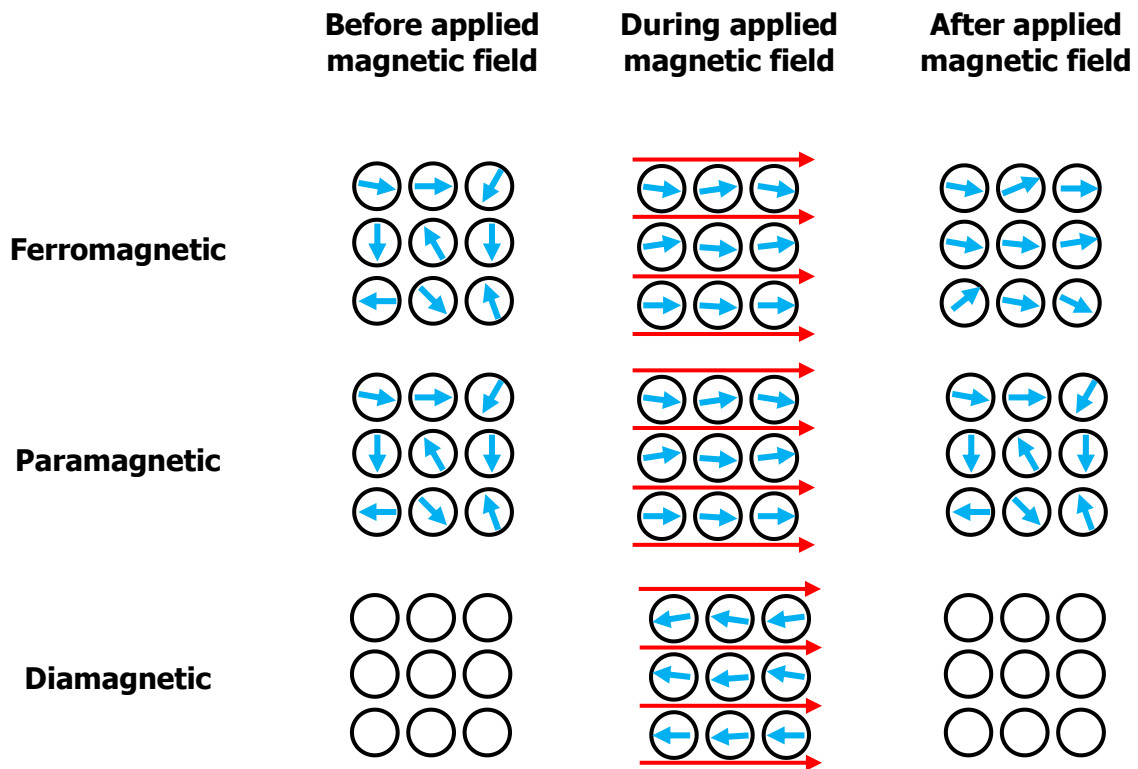


Figure 1.3 Overview of the magnetic susceptibility and the alignment of the magnetic domains: Ferromagnets (e.g. iron, nickel, and cobalt) show a strong attraction to magnetic fields and retain magnetization even after the external field is removed due to the persisting alignment of their magnetic domains; Diamagnets (e.g. copper, gold, and lead) are characterized by their development of a magnetization opposite to the applied magnetic field, leading to a weak repulsion against it. They do not retain magnetization outside an external field; Paramagnets (e.g. titanium and aluminum) are weakly attracted to magnetic fields and become magnetized in the direction of the field, but their magnetization disappears when the field is removed.

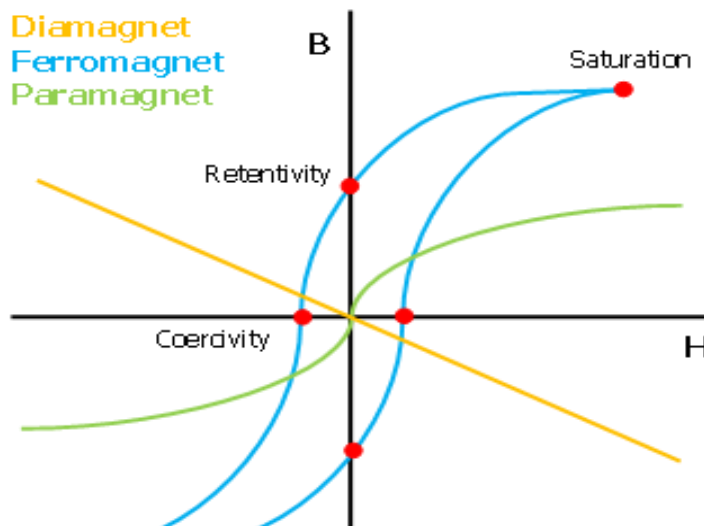


Figure 1.4 Ferromagnetic materials exhibit a non-linear relationship between B and H , characterized by the hysteresis loop shown in Figure 1.4. This loop represents the energy lost during one complete magnetic field application and removal cycle. The area within the hysteresis loop on a B - H curve represents the energy lost per cycle per unit volume of the material. This loss is significant only in ferromagnetic materials due to their domain structure and the substantial internal resistance to domain movement.

Electrical Resistivity (Conductivity)

Metals and alloys are generally relatively good electrical conductors, offering significantly lower electrical resistance than non-metallic materials like ceramics or plastics. While most metals are conductive, they can be categorized into different groups based on their electrical resistivities. Some metals and alloys, such as silver, copper, gold, magnesium, and aluminum, are known for their low resistivity ($\rho < 5.0 \cdot 10^{-8} \Omega \cdot m$). In contrast materials including titanium, carbon steel, stainless steel, and Ni-based superalloys are recognized for their higher resistivity ($\rho > 5.0 \cdot 10^{-8} \Omega \cdot m$) [19].

Several factors influence the electrical resistivity of metallic materials, including temperature, chemical composition, microstructure, and grain size. Typically, the resistivity of metals increases with rising temperature [19].

Relative Magnetic Permeability

Relative magnetic permeability μ_r reflects a capacity to conduct magnetic flux more effectively than a vacuum or air. A non-dimensional parameter indicates how a material compares to a vacuum or air in conducting magnetic and electric fields. Relative magnetic permeability significantly influences the choice of process parameters in electrical phenomena, such as the skin effect, electromagnetic edge and end effects, and ring effects [19].

Additionally, the product of the magnetic permeability μ_r and the constant permeability of free space μ_0 is equal to the ratio between the magnetic flux density (B) and magnetic field intensity H [19]:

$$\frac{B}{H} = \mu = \mu_r \cdot \mu_0 \quad (1.6)$$

Although relative magnetic permeability plays an essential role in the IH process, this constant will be mostly neglected since the main focus is identifying paramagnetic materials with a relative permeability of almost equal to 1.0. However, when considering ferromagnetic materials, this property cannot be overlooked.

Specific Heat

Specific heat c is defined as the heat capacity per unit mass of a material, indicating the energy needed to raise the temperature by one degree Celsius. It is typically measured in $J/(kg \cdot ^\circ C)$. A Material with a higher specific heat value requires more energy to heat a unit mass by a unit temperature increment. Thermal conductivity κ and specific heat c are influenced by various factors, including chemical composition, residual elements, grain size, plastic deformation, previous heat treatments, and similar aspects [24]. In addition, the specific is temperature dependent.

Thermal Conductivity

Thermal conductivity κ measures the speed at which heat moves through a thermally conductive material. Materials with higher κ -values transfer heat more quickly than those with lower κ -values and facilitate the achievement of a uniform temperature distribution throughout the workpiece, which is crucial in applications that require heating the material through its entire thickness [19].

Side Effects During Induction Heating

This section discusses the most relevant side effects during the induction heating process. These effects are crucial for explaining the object's behavior exposed to the AMF.

Skin Effect

Alternating current (AC) tends to concentrate at the surface of a workpiece, a phenomenon known as the skin effect. For instance, the current does not flow at the center of a cylindrical workpiece. Instead, the current intensity decreases exponentially from the surface towards the center [19]. The current distribution through the thickness of a cylindrical billet, as shown in Figure 1.5, can be calculated using equations 1.7 and 1.8:

$$I = I_0 \cdot e^{-\frac{r}{\delta}} \quad (1.7)$$

$$\delta = 503 \cdot \sqrt{\frac{\rho}{\mu_r \cdot f}} \quad (1.8)$$

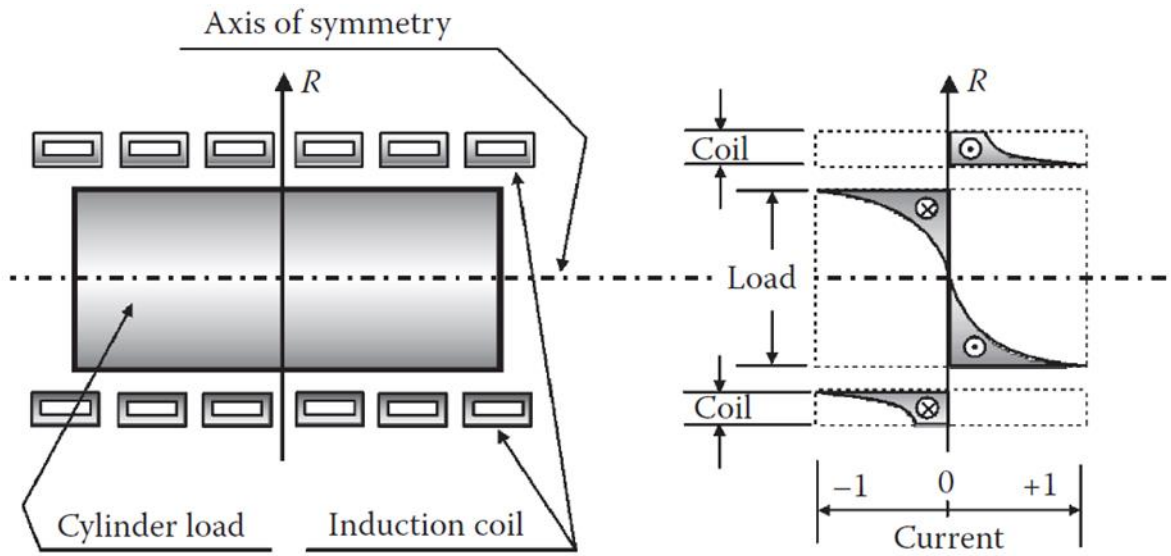
The skin effect is characterized by the reference depth δ , indicating the depth at which the current strength decreases by a factor of e . The penetration depth δ is determined by various factors, including the electrical resistivity ρ , the relative magnetic permeability μ_r , and the frequency f . Since these material properties can vary with temperature, the value of δ also changes as the workpiece is heated [19].

End & Edge effect

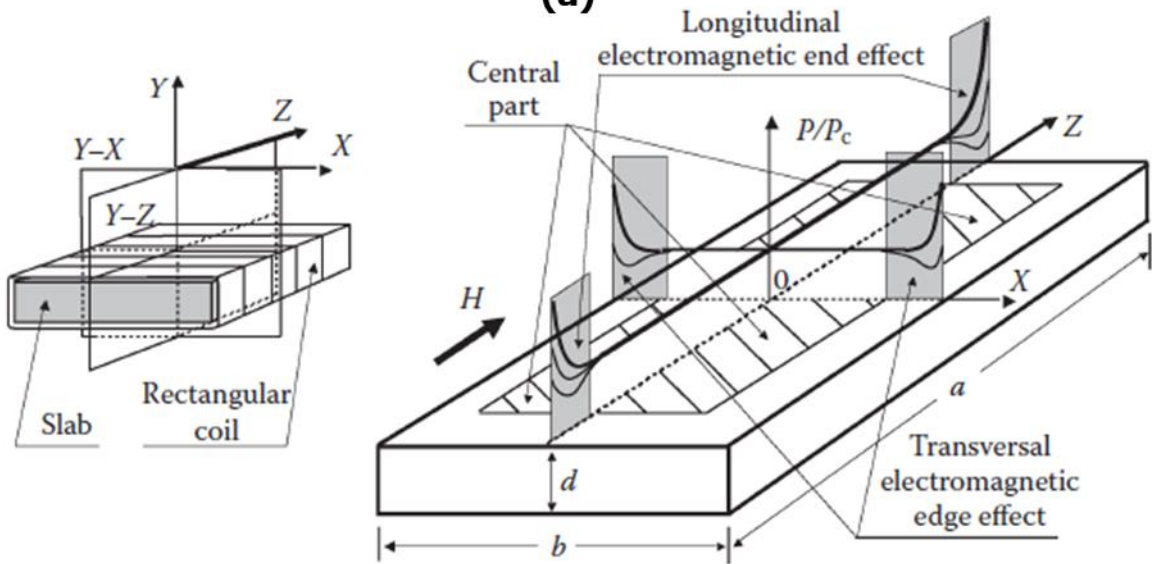
A similar effect can be seen in the ends and edges of the workpiece (Figure 1.6). The end effect arises from the spreading of the electromagnetic field at the ends of the workpiece leading non-uniform heating profile, with higher temperatures reached at the ends and edges. The edge effect often causes more concentrated heating at the edges due to the electromagnetic field interactions. The end and edge effect create challenges in achieving uniform heating, necessitating careful system design and adjustments in coil design, power settings, frequency, and workpiece positioning to mitigate these uneven heating patterns and ensure effective and consistent heating throughout the workpiece [19].

Ring Effect

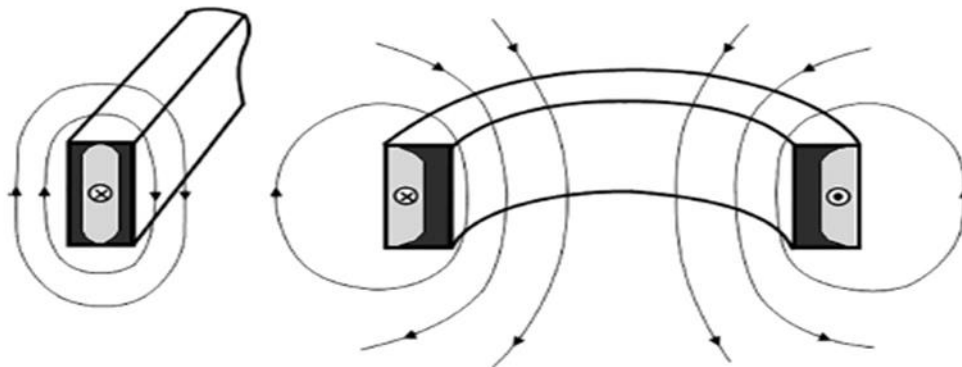
If we insert a workpiece shaped like a ring/tube, its current distribution shifts (Figure 1.8). In this new configuration, the magnetic flux lines become more concentrated within the inner part of the ring, leading to an increase in magnetic flux density there. Conversely, outside the ring, these flux lines are more dispersed. Consequently, most of the current prefer to travel along the thin inner surface layer of the ring. This preference arises due to this path's shorter distance and lower impedance. This phenomenon is known as the ring effect. In the ring, the currents on the inner surfaces of the ring's opposite sides flow in opposing directions, attracting each other due to their orientation [19].



(a)



(b)



(c)

Figure 1.5 Side effects during induction heating: (a) The skin effect is demonstrated by AC distribution in coils and workpieces with higher current concentrations on the workpiece's surface [19], (b) Sketch of a rectangular slab with a coordinate system demonstrating the end and edge effect demonstrated by an increase in the power density concentration at the ends and edges of the slab [19], (c) Schematic drawing demonstrating the ring effect magnetic field lines and current distribution [19].

2 Methods & Materials

2.1 Phase I: IH trials

Specimen Geometry Selection

The analytical model defined in this thesis was applied to a symmetrical, one-dimensional, infinitely long cylindrical coordinate model. This geometry was approximated for the experiments with a thin-walled, quasi-endlessly long hollow cylinder. This geometry (Figure 2.1), is characterized by a length-to-outer-diameter ratio of 10:1 and a wall thickness of 0.5 mm (4:1 ratio of radius to wall thickness), can be aligned with the analytical model and thus is more suitable for validation.

Figure 1.5(b) demonstrates that edges and other sharp features lead to a non-uniform heating pattern due to disturbances in the magnetic field. Consequently, the geometry chosen for this experiment is cylindrical, which can be accurately described using cylindrical coordinates and lacks sharp edges. Additionally, the elongated geometry ensures that the central portion is relatively far from any edges, further promoting uniform heating conditions. This proposed analytical model considers edge effects negligible, as temperature measurements are conducted centrally away from the specimen's edges. Additionally, the thin walls allow us to assume uniform current density across the wall thickness in the analytical solution.

This proposed model considers edge effects negligible, as temperature measurements are conducted centrally away from the specimen's edges. The slim, thin walls also enable the assumption of uniform current density across the wall thickness, facilitating a more straightforward analytical approach.

Material Selection and Preparation

In this study, four metallic materials were compared. Copper SF-Cu / Cu-DHP was selected to explore the thermal response of metals with lower electrical resistance. Low-carbon ST.37 steel was used as a substitute for pure iron, a potentially new biodegradable biomaterial. Stainless steel 316L and CP titanium Gr. 2 were included due to their everyday use in orthopedic applications. The SF-Cu / Cu-DHP, Stainless steel 316L, CP titanium Gr. 2 were supplied by (Salamon's Metalen B.V, The Netherlands), Low-carbon ST. 37 steel was supplied by (CM Staal, The Netherlands).

Before the experiments, each specimen was cleaned using a two-step ultrasonication process. First, it was sonicated in isopropanol for five minutes, followed by another cleaning in demineralized (DM) water for five minutes. Afterward, it was air-dried.

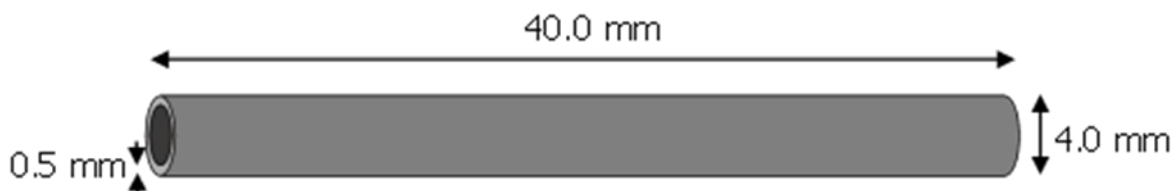


Figure 2.1 Specimen geometries quasi-endless thin-walled hollow cylinder for validation experiment.

Material Properties Analysis

To ensure the model's accuracy, the assessed materials were characterized to compare, and the values obtained were compared with the values of their properties obtained from the literature.

X-ray fluorescence (XRF) spectroscopy was used to validate the chemical composition of all samples. The measurements were performed with an Axios Max WD-XRF spectrometer, and data analysis was done with SuperQ5.0i/Omnian software (Malvern Panalytical, United Kingdom).

Due to the narrow geometry, even minor dimension deviations can affect the results of the analytical model predictions. Therefore, the specimen's outer diameter was measured at three random locations and averaged. The specimens were weighed, and the results were used to calculate the density and resistivity. The diameter of the specimens was measured using the Digital ABS AOS Caliper (Mitutoyo, Japan), with an accuracy of 0.01 mm. The scale used for weighing the specimens was an EMS 6K0.1 digital scale (Kern, Germany), with an accuracy of 0.1 grams.

A four-point resistance test was performed to validate the resistivity values found in the literature. This method applies a known current between two outer probes placed on the material, and the potential difference (voltage) is measured between two inner probes. The four-point resistance test minimizes the impact of contact resistance, which is particularly beneficial when assessing materials with very low resistivity. A schematical representation of the four-point resistivity test is shown in Figure 2.2. A power supply D 050_10 (DELTA ELEKTRONIKA, The Netherlands) generated the current for the four-point resistivity test. Two digital multimeters, GDM-8135 (GW Instek, Taiwan), were used to measure the current with an accuracy of 0.01 A and voltage with an accuracy of 0.001 V.

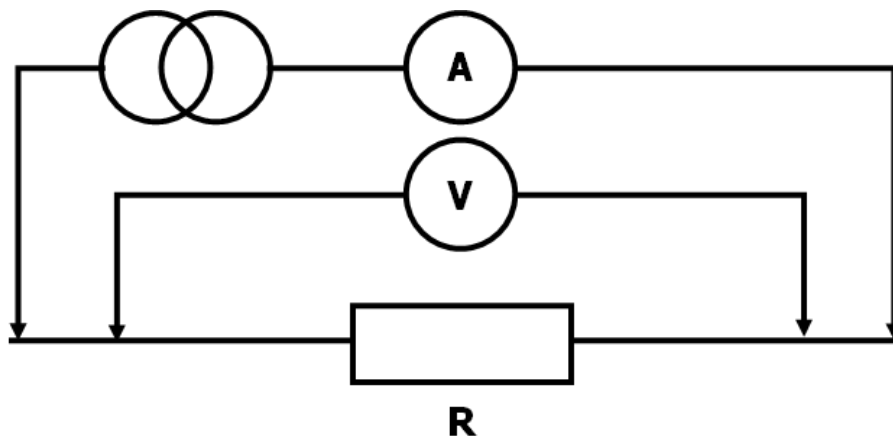


Figure 2.2 schematical four-point resistivity test setup.

Experimental Setup for IH

This study selected the MagneTherm device (Nanothermics, United Kingdom) for the validation experiments (Figure 2.3(f)). The device offers three coil configurations: an external planar coil with a core composed of three copper wires (Figure 2.3A), which can be used for live imaging (*e.g.*, by employing a thermal camera), an eighteen-turn solenoid coil (Figure 2.3(b)), and a nine-turn solenoid coil (Figure 2.1(c)). The system offers a set of frequencies and magnetic field strengths predetermined by combining the selected capacitor and the coil. The available parameters are listed in Appendix I.

For these experiments, an 18-turn coil configuration was used (Figure 2.3(g)). The temperature generation by the specimens was tested at magnetic field strengths of 2, 4, and 8.0 mT and frequencies of 103.5, 155.3, 262.7, 371.6, and 601.6 kHz (Table 2.1). Each specimen was exposed to the AMF for 300 seconds, with the temperature recorded every 6 seconds using optic fiber probes (part of the MagneTherm system). These probes were arranged as depicted in the schematics in Figure 2.3(d) and(e). One probe (T1) was positioned centrally inside the specimen, and the other (T2) at the wall of the tube, both at the same height and away from the specimen's edges, to minimize the edge heating effects neglected in the analytical model. Moreover, it is essential to note that the probes have an upper limit of temperature detection at 80 °C.

Every combination of field parameters and materials was tested in triplicates ($n = 3$). The average \pm standard deviation was calculated to compare the data with the analytical model predictions.

Each cleaned specimen was positioned inside a tube to keep the specimens centered and upright. The tube was then filled with 3.15 mL of demi water to submerge the specimen fully. This full submersion was crucial to ensure that the optical probes could accurately measure temperature since they do not perform well in air and to allow water to circulate the specimen, preventing any heat buildup in water trapped within any hollow sections of the specimen. The analytical model relied on the assumption of complete submergence for accurate heat flow calculations. Finally, the tube assembly was carefully placed at the center of the induction coil and secured by an insulating specimen holder. A safety protocol for handling these materials is included in Appendix II.

Table 2.1 Alternating magnetic field parameters

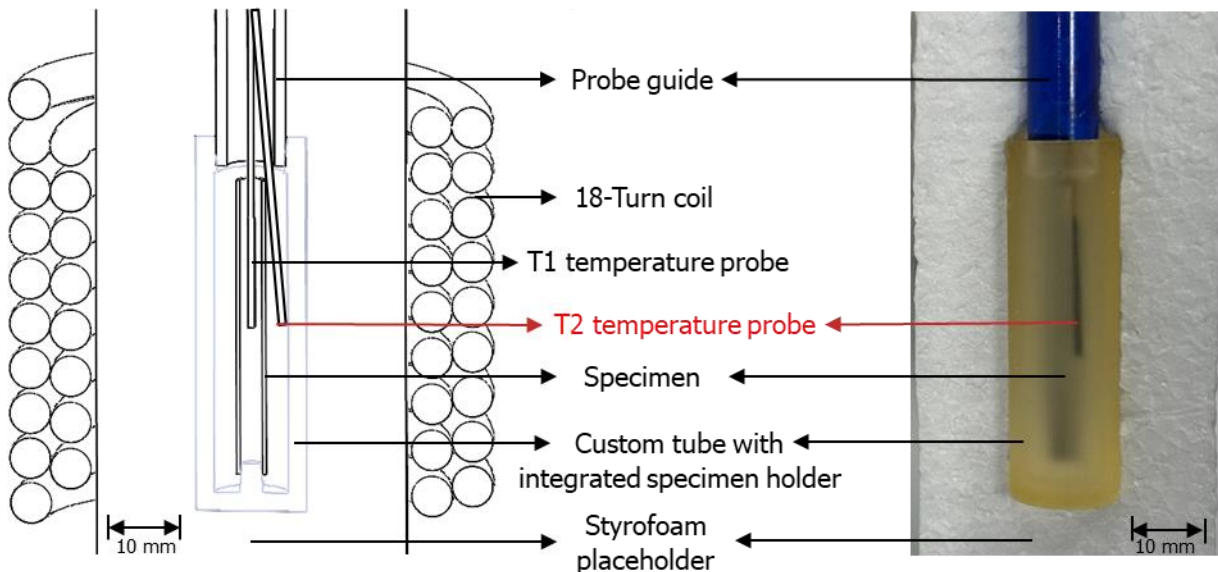
Field Amplitude (mT)	AMF frequency (kHz)				
	103.5	155.3	262.7	371.6	601.6
2	X	X	X	X	X
4	X	X	X	X	X
8	X	X	X	X	X



(a)

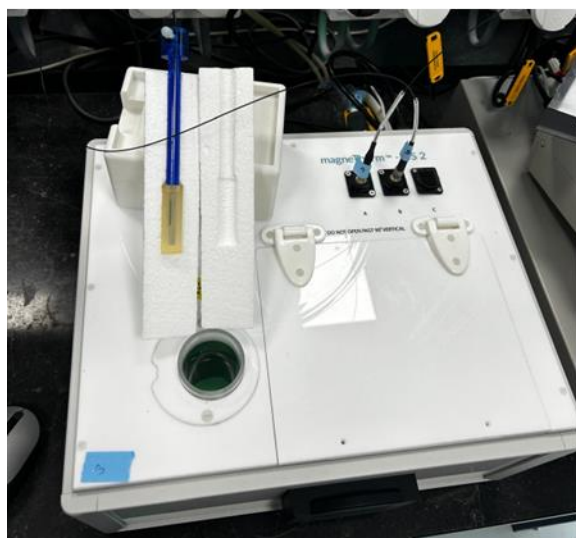
(b)

(c)



(d)

(e)



(f)



(g)

Figure 2.3 Experimental setup for IH trials: (a) planar coil option (eight-turn three core planar coil), (b) eighteen-turn double wound solenoid coil, (c) nine-turn double wound solenoid coil, (d) schematical cross-section of the experimental setup, (e) custom designed tube filled with demi water, the specimen and temperature probes, (f) MagneTherm test setup, (g) close-up of the eighteen-turn configuration on the MagneTherm.

2.2 Phase II: Analytical Modeling

Modeling Methods and Assumptions

An analytical method was chosen instead of the finite element method (FEM). Although FEM is frequently employed to simulate these disturbances, it cannot often offer detailed insights into the specific parameters that influence the thermal response. The analytical model was developed using Python within Anaconda's Spyder environment.

The analytical model considered only the phenomenon of Eddy current heating to maintain simplicity and clarity. Furthermore, a steady state was assumed, neglecting the influence of the transient. Secondary effects, such as hysteresis, were intentionally excluded. Regarding the geometry of the specimen, two models were created. The first model, "Model 1" was based on an infinitely long tube with an infinitely narrow wall, neglecting the edge effects. The second model, referred to as "Model 2", considered a geometry with a finite wall thickness and served as a validation of "Model 1". The validation FEM analysis was performed in FreeFem++ [25]. A summarized derivation of the analytical model is described below. A complete step-by-step derivation can be found in Appendix IV and the Python code of this model can be found in Appendix V.

Equation 2.1 describes the magnetic field inside the specimen.

$$B(t) = B_0 \sin(\omega t) + \mu_0 j(t)d \quad (2.1)$$

The magnetic field inside the specimen consists of two parts. The first part is the external magnetic field applied by the MagneTherm function generator. It has the field amplitude (B_0) of a sinus waveform and a frequency ω in radians (*i.e.*, $\omega = f2\pi$). Because the specimen is exposed to a constantly changing magnetic field, it generates a counteracting magnetic field. The magnetic permeability of free space describes this. μ_0 , Multiplied by the current density that runs through the specimen wall and is a function of time. Multiplied by the thickness of the tube d .

Equation 2.2 describes the electric field. $E(t)$,

$$E(t) = -\frac{1}{2}R \frac{dB(t)}{dt} \quad (2.2)$$

Which is given by the factor -0.5 multiplied by the radius of the specimen. Since an infinite narrow tube thickness is assumed the average radius of the specimen is selected $R = 0.5 \cdot (R_{outer} + R_{inner})$. The equation's last component is the magnetic field's time derivative. $\frac{dB(t)}{dt}$.

Equation 2.3 is the equation for the current density $j(t)$,

$$j(t) = E(t) \sigma = -\frac{\frac{B_0 \sigma R}{2} \omega}{\sqrt{\left(\frac{\mu_0 \sigma R d}{2}\right)^2 \omega^2 + 1}} \cos\left(\omega t + \tan^{-1}\left(\frac{-1}{\frac{\mu_0 \sigma R d}{2} \omega}\right)\right) \quad (2.3)$$

which is given by the electric field $E(t)$, multiplied by the electrical conductivity of the specimen. Once all the variables of this equation are filled in, this formula becomes an ordinary differential equation. This formula is rather complicated because it is a solution of a differential equation.

Finally, the power density P_d can be calculated in equation 2.4,

$$P_d(t) = j(t)^2 \frac{1}{\sigma} \quad (2.4)$$

which is essentially the same as the equation 1.5 given in chapter 1. However, since our model assumes an infinite tube length, the power density is calculated instead of the power. The power density is a product of the current density $j(t)$ squared multiplied by the electrical resistivity (in equation 2.4 it is expressed as its inverse relationship with electrical conductivity $\frac{1}{\sigma}$). With the power density, the power produced by the specimen can be calculated by multiplying it with its volume. Note that this model only describes a steady state; it does not describe the initial state (transient state).

The model's accuracy in representing an infinitely narrow tube was evaluated by comparing it against the model developed by James R. Nagel [26], which describes a cylinder with finite wall thickness. This comparison focuses specifically on vector potentials because using vector potentials simplifies the analysis by reducing the number of equations and unknowns involved, thus making comparison easier. The vector potential $A_\varphi(r)$ of "Model 1" was defined by equations 2.5 and 2.6 respectively,

$$\text{if } r < R, \quad A_\varphi(r) = \frac{rB_0}{2 + i\mu_0\sigma\omega d r} \quad (2.5)$$

$$\text{if } r > R, \quad A_\varphi(r) = \frac{1}{2}rB_0 + \frac{R^2B_0}{2r} \frac{i\mu_0\sigma\omega d R}{2 + i\mu_0\sigma\omega d R} \quad (2.6)$$

where B_0 is the field amplitude, R is the radius of the tube, μ_0 is the permeability of free space, σ is the electrical conductivity, ω is the field frequency in radians, d is the thickness of the tube.

Additionally, Prof. Dr. Ir. L. Abelmann has developed a simplified version of a solid cylinder model and has implemented a FEM analysis in Freefem++ [25]. This FEM analysis extends the complexity of the scenario by considering not only finite wall thicknesses but also finite lengths, which introduces a closer approximation to real-world conditions.

By comparing the outcomes from Abelmann's FEM analysis, which includes both finite wall thicknesses and finite lengths, with those from the analytical models, which assume infinite length, the analytical models were critically assessed on how accurately they represent finite physical systems. The comparison aimed to identify potential discrepancies and provide insights into whether modifications to the traditional models were necessary to better mirror real-world systems' behavior.

The final step of Phase III was the verification of the analytical models by comparing the computationally generated data of temperature increase with the experimental data obtained in Phase I.

2.3 Phase III: Targeted IH

This study aimed to investigate whether hyperthermia can be applied locally in the regions of interest, *i.e.*, the neck of an implant, through the combination of materials with different heating responses. This would limit the undesired heating of the whole implant, which may result in tissue damage. In the proposed strategy, a low-carbon steel ST. 37 coating with a high thermal response was integrated into the critical regions of an implant.

Specimen Geometry and Material Selection

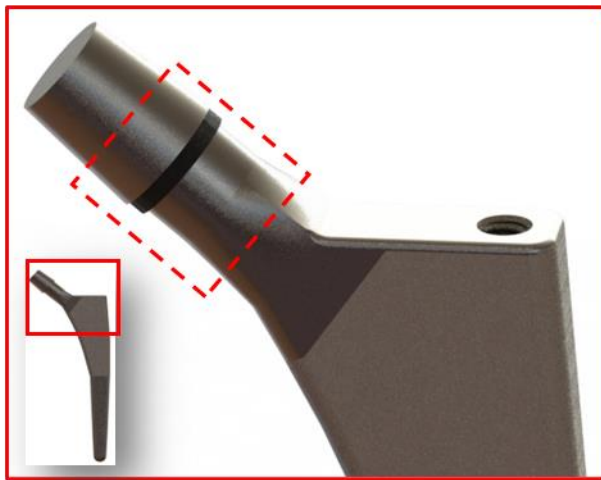
The neck of a hip implant has a cylindrical geometry, which can be translated into the analytical model constructed to describe that geometry. The results from the previous phases of this study were used to select suitable materials for this targeted heating strategy.

The proposed strategy integrates a material with high IH-susceptibility into these critical areas as a coating. An alternative approach to coating was placing a ferromagnetic element in the core of the neck and heating it from within. However, this approach is more technologically challenging and was not further investigated in this study. Figure 2.4(a) further illustrates the proposed concept of a hip implant with integrated ST. 37 coating. A medical-grade Ti6Al4V alloy (Gr. 23) round bar (ACNIS International, France) was used to mimic the neck. Low-carbon steel ST. 37 (CM Staal, The Netherlands) was used as a ferromagnetic coating material. The diameter and height of the sample were both 10 mm. The ring coating was fitted around the sample, as depicted in Figure 2.4(b). The dimensions of the ring coating are 10 x 0.3 x 2 mm (inner diameter x thickness x height). The components were machined to their required dimensions and then press-fitted together. After assembly, the samples were sintered at 1200 °C for two hours with argon gas to prevent oxidation and form a solid structure. The same titanium specimen lacking the St. 37 ring was used as a negative control.

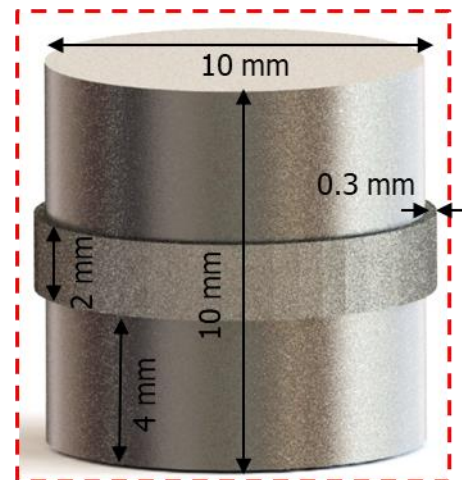
Experimental Setup

The specimens were placed in MagneTherm with the eighteen-turn coil and exposed to the AMF at several combinations of magnetic field strengths (2.0 and 4.0 mT) and field frequencies (103, 371, and 601 kHz) for 60 seconds. After that, the specimens were removed from the coil, and the temperature was immediately measured using a thermal camera. To account for any differences in emissivity that could lead to misreading with the thermal camera, the specimens were coated with Hammerite heat-resistant mat black paint. Figure 2.4(d),(e) shows the real-life test setup.

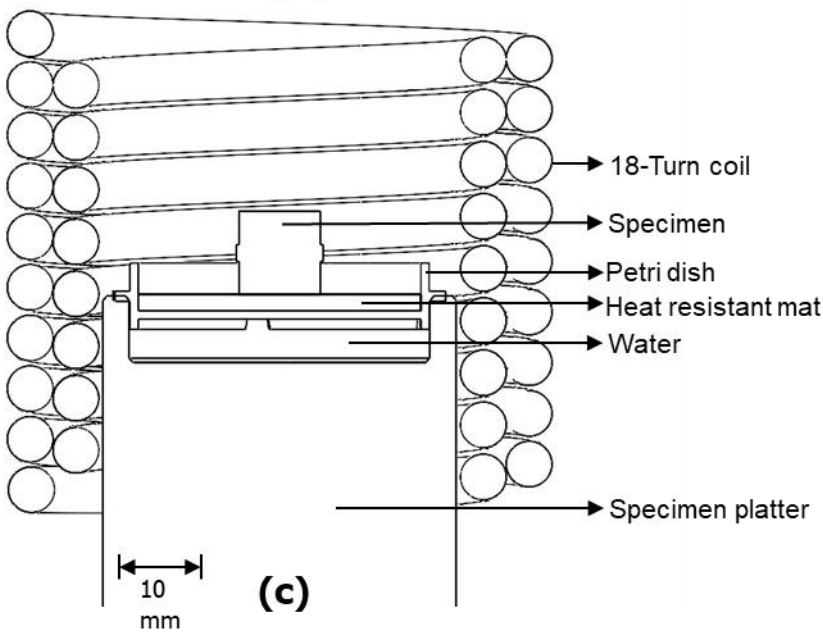
Figure 2.4(c) depicts a schematic cross-section showing the placement of the specimen within the MagneTherm. A specially designed specimen platter ensured the specimen remained centered within the coil, where the magnetic field is most uniform. The platter included a pocket designed to accommodate a 36 mm Petri dish. This dish is positioned in a water pocket, which cools the plastic petri dish and prevents overheating due to the induced heating in the specimen. A heat-resistant rubber mat was also placed on the bottom of the dish to provide further insulation from the induced heat.



(a)



(b)



(c)



(d)



(e)

Figure 2.4 (a) neck of femoral stem with a ferromagnetic iron coating applied to the critical region for infection, (b) specimen for the targeted induction heating, (c) schematical cross-section of the experimental setup, (d) real-life experimental setup close up, (e) real-life experimental setup.

3 Results

3.1 Phase I: Preparatory Research

Chemical Composition Analysis of the Assessed Materials

The elemental compositions of the investigated materials (copper, Stainless steel, Low-carbon steel, CP titanium Gr. 2) obtained from the X-ray fluorescence (XRF) analysis are presented in Table 3.1. All material compositions were standardized to a total weight percentage of 100 %. It must be noted that carbon cannot be detected through XRF analysis and, therefore, is not reflected in the obtained results.

Physical Properties of the Assessed Materials

Table 3.2 presents the material properties of the specimen materials as documented in the literature, while Table 3.3 shows the material properties obtained through direct measurements. The two data sets have a noticeable discrepancy, particularly in the density and electrical resistivity values.

Table 3.1 XRF analysis: chemical composition per specimen material (without carbon): (a) Copper SFU-CU / DHP-CU, (b) Stainless steel 316L, (c) Low-carbon steel ST. 37, (d) CP titanium Gr. 2.

(a) Copper SF-Cu / DHP-Cu		
Sum before normalization: (109.8 wt%)		
Element	Conc. (wt%)	Absolute Error (wt%)
Cu	97.634	0.4
Al	1.811	0.04
Si	0.138	0.01
Cl	0.1	0.01
Ca	0.084	0.01
P	0.065	0.008
Fe	0.063	0.008
Ti	0.053	0.009
S	0.052	0.007

(b) Stainless steel 316L		
Sum before normalization: (98.7 wt%)		
Element	Conc. (wt%)	Absolute Error (wt%)
Fe	69.14	0.5
Cr	16.098	0.2
Ni	10.576	0.3
Mo	1.979	0.04
Mn	0.71	0.04
Si	0.524	0.02
Co	0.353	0.03
Cu	0.327	0.04
Ta	0.105	0.04
V	0.096	0.01
Al	0.092	0.009

(c) Low-carbon steel ST. 37		
Sum before normalization: (88.2 wt%)		
Element	Conc. (wt%)	Absolute Error (wt%)
Fe	99.287	0.5
Mn	0.487	0.04
Si	0.104	0.01
Cr	0.044	0.008
Al	0.036	0.006
S	0.028	0.005
P	0.015	0.004

(d) CP titanium Gr. 2		
Sum before normalization: (105.6 wt%)		
Element	Conc. (wt%)	Absolute Error (wt%)
Ti	99.314	0.4
Fe	0.291	0.04
Al	0.205	0.01
Cl	0.082	0.009
Si	0.05	0.007
Ca	0.029	0.005
S	0.023	0.005
P	0.005	0.002

Table 3.2 Thermal, electric, and magnetic material properties at 20°C, obtained from literature [27]

Material	Density (Kg·m⁻³)	Thermal conductivity (W·m⁻¹·K⁻¹)	Specific heat (J·kg⁻¹ K⁻¹)	Electrical resistivity (mΩ·mm)	Magnetic Permeability (H·m⁻¹)	Magnetic Susceptibility
Copper SF-Cu / Cu-DHP	8890	388	385.0	$1.70 \cdot 10^{-2}$	0.999994	Diamagnetic
Low-carbon steel ST.37	7850	56.9 ^[1]	461 ^[1]	$1.83 \cdot 10^{-1[1]}$	x	Ferromagnetic
Stainless steel 316L	8000	16.3	500.0	$7.40 \cdot 10^{-1}$	1.008	Paramagnetic
CP titanium Gr. 2	4510	16.4	523.0	$5.60 \cdot 10^{-1}$	1.00005	Paramagnetic

Table 3.3 Experimentally obtained thermal, electric, and magnetic material properties at 20°C.

Material	Density (Kg·m⁻³)	Thermal conductivity (W·m⁻¹·K⁻¹)	Specific heat (J·kg⁻¹ K⁻¹)	Electrical resistivity (mΩ·mm)	Magnetic Permeability (H·m⁻¹)	Magnetic Susceptibility
Copper SF-Cu / Cu-DHP	8683	x	x	$2.14 \cdot 10^{-2}$	x	x
Low-carbon steel ST.37	7892	x	x	$1.54 \cdot 10^{-1}$	x	x
Stainless steel 316L	7942	x	x	$7.48 \cdot 10^{-1}$	x	x
CP titanium Gr. 2	4614	x	x	$4.64 \cdot 10^{-1}$	x	x

[1] source: <https://matmatch.com/materials/minfm94285-en-10025-grade-rst-37-2-untreated>

Induction Trials

This section presents the outcomes of the heat induction trials. Table 3.4 and Figures 3.3 and 3.4 show the experimental results. It is important to note that some results are highlighted in the table in specific colors for clarity. Results highlighted in orange were obtained through extrapolation. The data for the row marked in red could not be obtained because the temperature rapidly exceeded the 80 °C limit, thereby preventing any possibility of extrapolation.

Table 3.4 4 Experimental results from AMF induced heating of the assessed materials. The results present the mean value (n=3) ±standard deviation.

Material	Field Amplitude (mT)	ΔT (°C) over 300 seconds					
		103.5 KHz	155.3 KHz	261.7 KHz	371.6 KHz	601.6 KHz	
Stainless steel 316L	2	2.2 ± 0.4	3.3 ± 0.2	5.9 ± 0.4	7.6 ± 0.5	11.0 ± 0.7	
	4	7.4 ± 0.4	13.3 ± 0.2	23.9 ± 0.3	31.9 ± 1.5	45.3 ± 0.6	
	8	28.6 ± 1.1	44.6 ± 1.9	65.3 ± 4.3	95.7 ± 2.2	168.3 ± 5.4	
SF-Cu / DHP-Cu	2	0.6 ± 0.2	0.8 ± 0.2	1.0 ± 0.2	1.2 ± 0.2	1.5 ± 0.4	
	4	2.4 ± 0.2	2.4 ± 0.1	4.2 ± 0.2	4.3 ± 1.0	8.0 ± 0.4	
	8	11.2 ± 0.2	12.8 ± 0.5	17.7 ± 0.3	22.3 ± 0.7	35.2 ± 1.2	
Low-carbon steel St.37	2	28.4 ± 0.3	28.3 ± 2.0	34.4 ± 1.4	37.2 ± 0.8	47.6 ± 1.0	
	4	103.2 ± 3.6	122.7 ± 6.9	154.2 ± 7.6	184.9 ± 3.9	321.2 ± 36.5	
	8	X	X	X	X	X	
CP titanium Gr. 2	2	2.3 ± 0.6	3.3 ± 0.5	5.7 ± 0.7	7.3 ± 0.3	9.9 ± 0.4	
	4	7.6 ± 0.3	9.0 ± 0.2	15.8 ± 0.3	20.8 ± 0.6	30.2 ± 2.3	
	8	28.2 ± 0.7	46.1 ± 1.2	63.2 ± 0.9	91.4 ± 1.0	176.5 ± 11.6	



Mean value obtained by extrapolation
 Mean value could not be obtained

There is a clear difference among the materials. Each material demonstrated a rise in temperature as the frequency and field amplitude increased. Results indicate that copper is the least responsive among the four tested materials. The copper specimen reached a peak temperature rise of 47.6 °C at the maximum field amplitude and frequency, while the other three materials achieved similar temperature increases at significantly lower amplitudes and frequencies.

CP titanium and Stainless steel 316L exhibited similar patterns in temperature response. Although these materials showed nearly identical behaviors at 2.0 and 8.0 *mT* amplitudes, the response of titanium at 4.0 *mT* was markedly less than that of Stainless steel 316L, with a maximum temperature difference of 15.1 °C at the highest frequency of 601.6 *kHz*.

Low-carbon steel was found to be the most responsive material. Due to its high reactivity, temperature measurements exceeded the 80 °C detection limit already at 2.0 and 4.0 *mT*, preventing further data extrapolation. The extrapolation of the data showed an extreme temperature increase of 321.23 °C at just 4.0 *mT* and a frequency of 601.6 *kHz*; however, the data were burdened by a high standard deviation.

Statistical analysis

To identify the influence of the three parameters, a three-factor ANOVA was performed to explore the interactions between these three factors. Through this statistical analysis, the main effects of each independent variable (material, frequency, and amplitude) can be determined on the dependent variable (the temperature increase)

If any factor or interaction had a high p-value, it would suggest that changes in that factor do not significantly affect the response variable. However, the p-values for all factors (material, frequency, amplitude) independently indicate a statistically significant effect on the response variable. In the three-factor ANOVA (Table 3.5), the effects of material, frequency, amplitude, and two-way interactions were assessed to determine their impact on the response variable. The analysis revealed the following significant results:

Independent factors:

- Material: The effect of material was highly significant ($F(3,20) = 49.06, p < 0.00001$), suggesting substantial variability in the response depending on the material type used.
- Frequency: Frequency also showed a significant effect ($F(4,20) = 11.40, p < 0.0001$), indicating that the response variable is sensitive to changes in frequency.
- Amplitude: The effect of amplitude was significant ($F(2,20) = 43.68, p < 0.00001$), demonstrating that different amplitudes affect the response variable notably.

Interactions:

- Material and frequency: The interaction between material and frequency was not statistically significant ($F(12,20) = 2.16, p = 0.061$), suggesting that the effect of material on the response does not differ across frequencies.
- Material and amplitude: There was a significant interaction between material and amplitude ($F(6,20) = 14.16, p < 0.00001$), indicating that the impact of amplitude on the response varies with different materials.
- Frequency and amplitude: The interaction between frequency and amplitude was also significant ($F(8,20) = 3.59, p = 0.009$), showing that the response to amplitude changes depending on the frequency.

Table 3.5 Three-factor ANNOVA results

	sum_sq	df	F	PR(>F)
C(Material)	76292.12974	3.0	49.05575	2.098917E-09
C(Frequency)	23647.76824	4.0	11.40412	5.503604E-05
C(Amplitude)	45285.18196	2.0	43.67748	5.035919E-08
C(Material):C(Frequency)	13465.976	12.0	2.164652	6.115023E-02
C(Material):C(Amplitude)	44029.66876	6.0	14.15551	5.467926E-06
C(Frequency):C(Amplitude)	14886.86824	8.0	3.58959	9.664482E-03
Residual	10368.08455	20.0	NaN	NaN

3.2 Phase II: Analytical Modeling

IH Predictions Through the Analytical Model

Based on the analytical solution, two domains for optimal conditions for the highest power densities can be identified, each characterized by equations 3.1 and 3.2, respectively:

$$\text{if } \mu_0 \sigma d r \omega \gg 2, \quad \text{then} \quad \langle p \rangle = \frac{B_0^2}{2 \cdot \mu_0^2 \cdot d^2 \cdot \sigma} \quad \omega \gg \omega_c \quad (3.1)$$

$$\text{if } \mu_0 \sigma d r \omega \ll 2, \quad \text{then} \quad \langle p \rangle = \frac{B_0^2 \cdot \sigma \cdot R^2 \cdot \omega^2}{8} \quad \omega \ll \omega_c \quad (3.2)$$

$$\omega_c = \frac{2}{\mu_0 \cdot \sigma \cdot d \cdot R} \quad (3.3)$$

In the presented scenario, μ_0 was a constant, and with the assumption of a constant geometry for all the specimens throughout phase I, parameters R and d were also constants. Thus, the only variables were B_0 and ω . Note that the power density is independent of the frequency in the first domain but grows quadratically with the field amplitude. In contrast, the second domain is quadratically dependent on the frequency and field amplitude. Assigning materials to specific regimes enables a more accurate prediction of their behavior under varying frequencies and field strengths. The equation 3.3 describes the critical frequency ω_c .

Each material and frequency combination could be assigned to the correct domain depending on the selected frequency. Note that SF-Cu / DHP-Cu could be assigned to Domain 1, since $\omega \gg \omega_c$ for all available frequencies in this experiment. Also, note that the critical frequency was never exceeded for Stainless steel 316L and CP Titanium Gr.2; therefore, they can be assigned to Domain 2. Low-carbon steel ST.37 was in the same range of the used frequencies and, therefore, fell between the two domains. The overview of the ω_c for each material is in Table 3.6.

Table 3.7 displays the results from the analytical model with parameters found in the literature and experimentally determined parameters, respectively. These tables present the temperature rise of the assessed materials over 300 *seconds* of AMF exposure. Each entry corresponds to a specific condition of a material exposed to a combination of a particular magnetic field strength and frequency. The data in those tables indicate that Stainless steel 316L is expected to undergo the most significant temperature rise over 300 *seconds*. CP titanium also shows a considerable increase in temperature. Low-carbon steel generates about one-third of such a temperature increase. Copper exhibits the least overall temperature increase and a frequency-independent trend. Both data sets showed a similar trend in temperature rise with increasing frequency and magnetic field strength; however, the material properties caused some discrepancies in the results between the two models.

Table 3.6 Domain differentiation of the included materials.

Material	Critical frequency (kHz)
SF-Cu / DHP-Cu	61.11
Stainless steel 316L	$2.137 \cdot 10^3$
Low-carbon steel ST.37	440.0
CP titanium Gr.2	$1.326 \cdot 10^3$

Table 3.7 Analytical model predictions with parameter values found in the literature, predictions with experimentally obtained material properties and the error

Material	Magnetic Field strength [mT]	<i>ΔT</i> (°C) over 300 seconds																	
		103.5 KHz			155.3 KHz			262.7 KHz			371.6 KHz			601.6 KHz					
		literature values	measured values	error	literature values	measured values	error	literature values	measured values	error	literature values	measured values	error	literature values	measured values	error			
Stainless steel 316L	2	4.12	3.31	±0.11	7.17	6.05	±0.21	11.68	10.61	±0.36	14.05	13.30	±0.45	16.06	15.78	±0.53			
	4	16.47	13.26	±0.45	28.69	24.21	±0.82	46.71	42.44	±1.44	56.19	53.21	±1.80	64.25	63.10	±2.14			
	8	65.88	53.03	±1.80	114.76	96.84	±3.28	186.83	169.77	±5.75	224.76	212.85	±7.21	256.99	252.42	8.55			
	2	0.41	0.51	±0.02	0.41	0.51	±0.02	0.41	0.51	±0.02	0.41	0.51	±0.02	0.41	0.51	±0.02			
SF-CU / DHP-CU	4	1.63	2.05	±0.06	1.63	2.06	±0.06	1.63	2.06	±0.06	1.63	2.06	±0.06	1.63	2.06	±0.06			
	8	6.52	8.21	±0.25	6.53	8.23	±0.25	6.53	8.23	±0.25	6.54	8.24	±0.25	6.54	8.24	±0.25			
	2	3.65	3.11	±0.02	4.03	3.41	±0.03	4.25	3.58	±0.03	4.32	3.64	±0.03	4.36	3.67	±0.03			
	4	14.61	12.44	±0.10	16.10	13.63	±0.11	17.01	14.34	±0.11	17.27	14.54	±0.12	17.43	14.67	±0.12			
Low Carbon Steel	8	58.42	49.77	±0.39	64.40	54.52	±0.43	68.02	57.36	±0.45	69.07	58.17	±0.46	69.73	58.69	±0.46			
	4	14.61	12.44	±0.10	16.10	13.63	±0.11	17.01	14.34	±0.11	17.27	14.54	±0.12	17.43	14.67	±0.12			
	2	4.76	4.22	±0.19	7.46	6.48	±0.29	10.60	8.98	±0.40	11.95	10.02	±0.44	12.97	10.79	±0.48			
CP titanium Gr. 2	4	19.02	16.88	±0.75	29.85	25.93	±1.15	42.39	35.93	±1.59	47.79	40.09	±1.77	51.87	43.17	±1.91			
	8	76.08	67.54	±2.99	119.39	103.71	±4.59	169.56	143.72	±6.36	191.14	160.34	±7.10	207.46	172.69	±7.64			

FEM Analysis

Although FEM (Finite Element Method) analysis is typically complex and can be challenging to interpret, an FEM analysis of the geometry used in Phase I was conducted. This analysis allows for the evaluation of the analytical models by comparing their outcomes with those derived from the FEM model. Figure 3.1(a) depicts the simulation space. The geometry is modeled in 2D, with a cross-section of half the hollow cylinder displayed; since the specimen is symmetrical around the central axis (the left border of the simulation space shown in Figure 3.1(a)), the image can be rotated around this axis, to give the full 3D analysis. The source code for the FreeFEM++ is given in Appendix VI.

Figure 3.1(b) shows the vector potential and magnetic field. Note that the vector potential increases as it moves away from the center (*i.e.*, the center of the cylindrical specimen).

Figure 3.1(c) shows the magnetic field distribution around the specimen. Inside the specimen, the magnetic field shows uniformity (cyan blue region). However, it becomes nonuniform around the ends and edges.

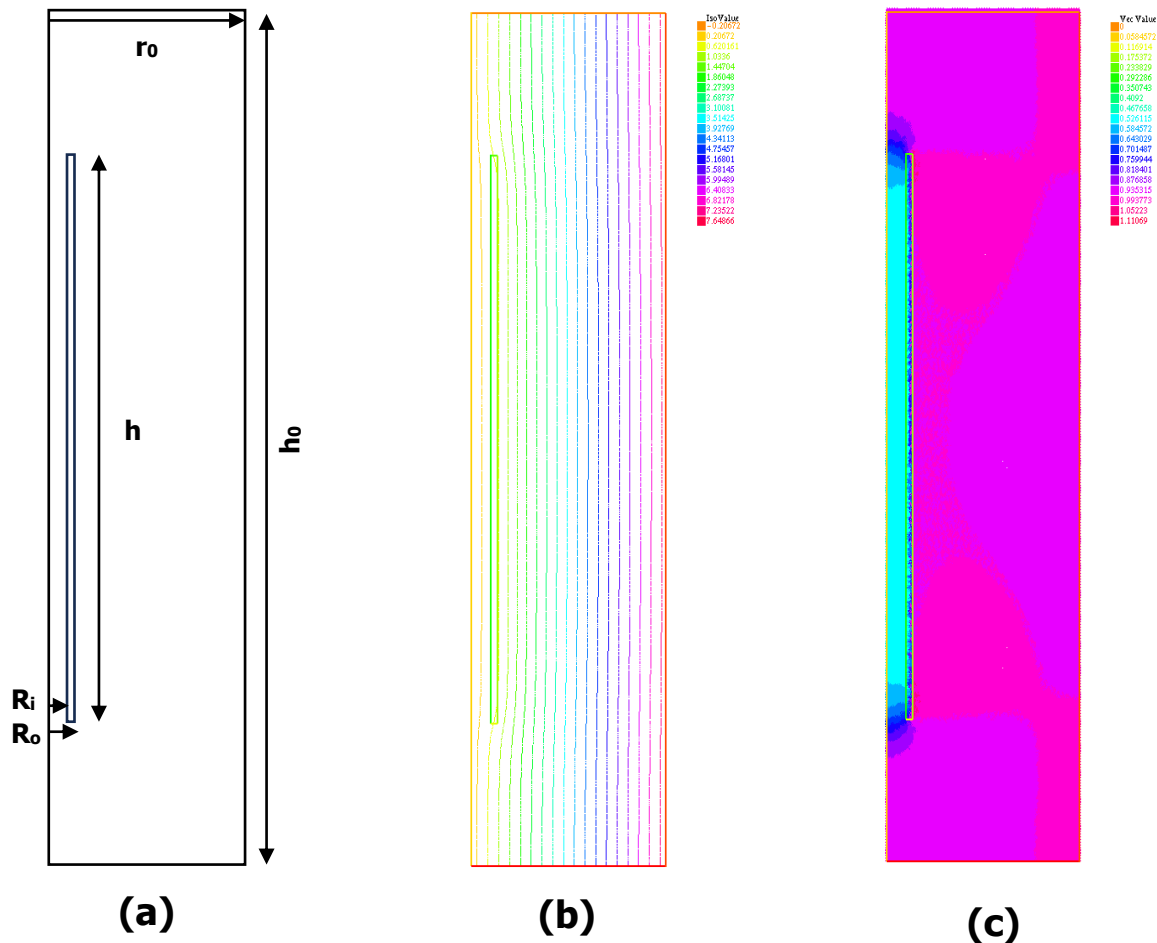


Figure 3.1 FEM of the specimen geometry used in Phase 1: (a) Simulation space and cross-section of the specimen, where r_0 is the radius of the simulation space, h_0 is the length of the simulation space, h is the height of the specimen, R_i is the inner radius of the specimen, and R_o is the outer radius of the specimen, (b) Vector potential distribution, (c) Magnetic field distribution

Evaluation of the Analytical Model

The vector potentials of the FEM analysis, "Model 2" and the "Solid rod model" mentioned in section 2.2 are plotted in Figure 3.2(a), and the vector potentials of "Model 1" and "Model 2" are plotted in Figure 3.2(b). In both figures, the schematical wall is plotted with the value for R_{inner} at $r = 1.5 \text{ mm}$ and R_{outer} at $r = 2.0 \text{ mm}$. Note that for the infinitely narrow wall thicknesses $R = 0.5 \cdot (R_{outer} + R_{inner}) = 1.75 \text{ mm}$.

Examining the graphs in Figure 3.2(a), it is evident that the vector potentials of the FEM analysis, "Model 2," and the "Solid Rod Model" all follow the same trend. Similarly, Figure 3.2(b) shows that "Model 1" and "Model 2" exhibit similar vector potentials. However, "Model 1" displays a sudden drop in vector potential. The source code for calculating and plotting the powerdensit

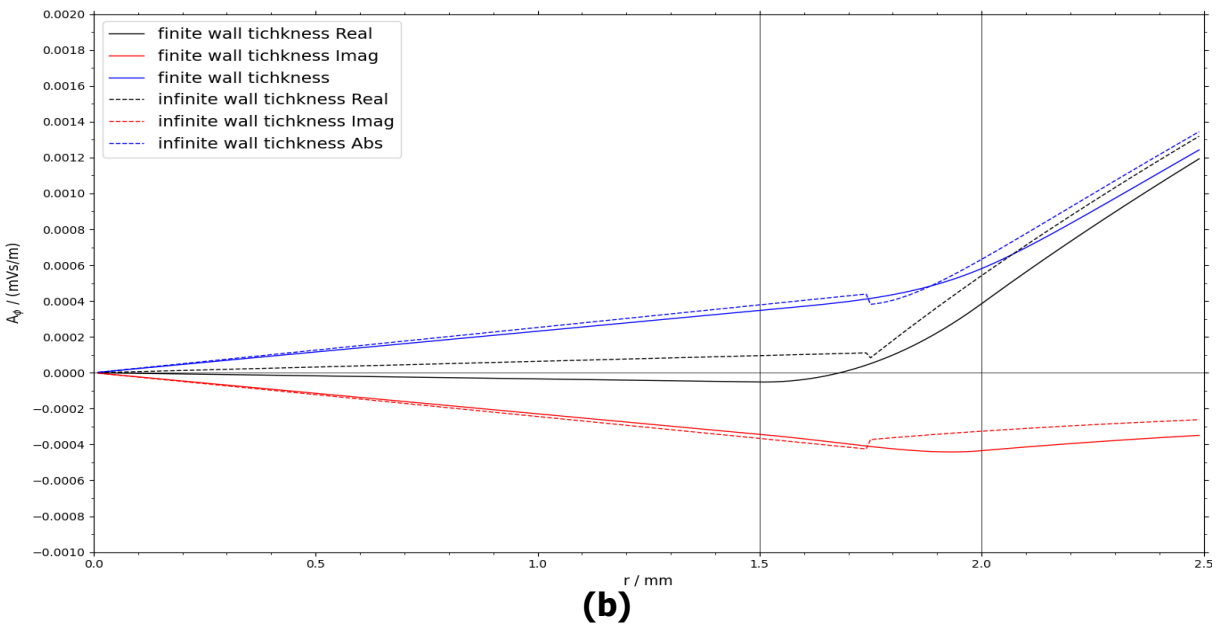
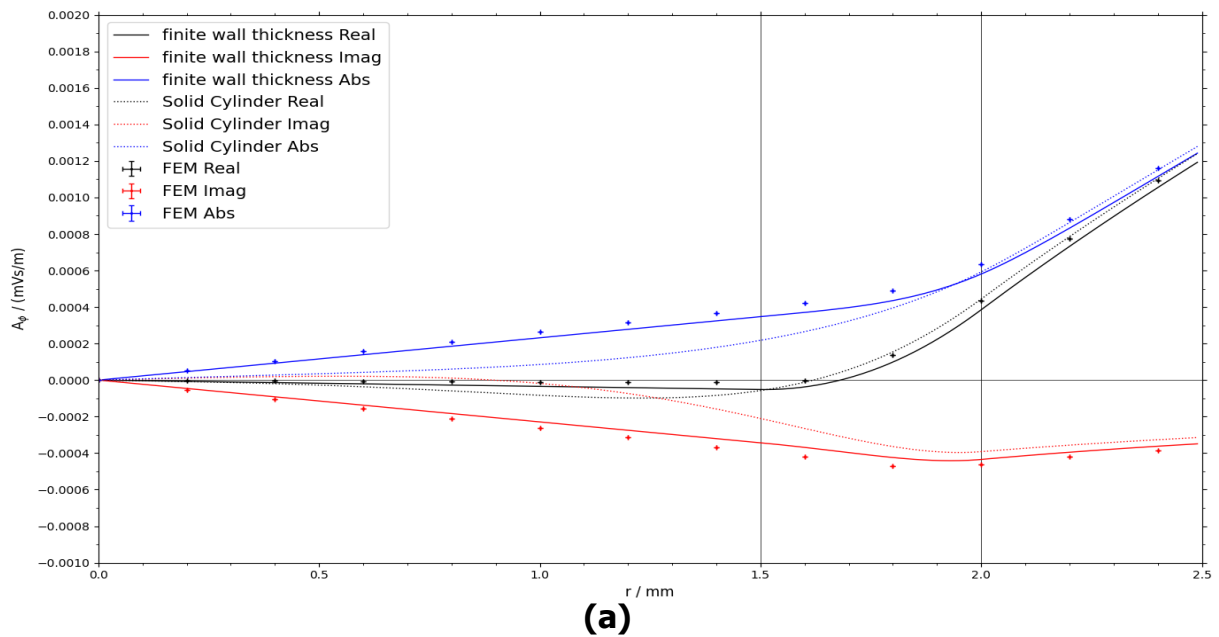


Figure 3.2 Vector potential plots with field parameters for Copper at 2.0 mT and 601 kHz (Real, Imaginary, and Absolute part): (a) Vector potential of the finite wall thickness model "Model 2", the FEM analysis and a Solid rod model, (b) Vector potential of the infinite wall thickness model "Model 1" and finite wall thickness model.

Accuracy of the Analytical Model: Factorial Comparison with the Experimental Data

To validate the accuracy of the analytical model in predicting the temperature rise, the obtained computational data was compared with the experimental data presented in section 3.1 (and summarized in Table 3.4).

The data obtained from the experiments were compared with the analytical model “Model 1”. The comparison is shown via the factorial difference of the experimental data divided by the analytical model results (Table 3.8). Note that the data for Low-carbon steel St.37 at 8mT could not be obtained. With a perfectly accurate model, the values in Table 3.8 would all equal one, indicating a match between predicted and observed temperature increases. However, the actual results deviated from this ideal.

For the materials Stainless steel and CP titanium, the factorial difference showed some consistency, with the model overestimating the temperature increase by a factor ranging between 1.5 and 3. This implies that while the model did not perfectly predict the outcomes, it consistently estimated the temperature increase to be two to three times higher than experimentally observed. As the magnetic field frequency increased, the model's predictions showed a slight improvement in accuracy, with the factors moving closer to one. In contrast, the model significantly underestimated the temperature increases for Low-carbon steel, with deviation factors ranging from 8 to 18. The discrepancy between the model's predictions and the actual measurements for these materials grew as the frequency increased. The analytical model predicted frequency-independent values for copper, while the experiment's results clearly show frequency-dependent behavior. This is demonstrated in the factorial difference for copper, in which temperature and frequency rise.

To further evaluate the discrepancies between the analytical and experimental data, the temperature rise was plotted against the field frequency (Figure 3.3) and magnetic field strength (Figure 3.4).

Table 3.8 Factorial difference (experimental values / analytical model values)

Material	Field Amplitude [mT]	Factorial difference (experimental/analytical model values)				
		103.5 kHz	155.3 kHz	262.7 kHz	371.6 kHz	601.6 kHz
Stainless steel 316L	2	0.66	0.55	0.55	0.57	0.70
	4	0.56	0.55	0.56	0.60	0.72
	8	0.54	0.46	0.38	0.45	0.67
SF-Cu / DHP-Cu	2	1.20	1.51	1.93	2.29	2.92
	4	1.15	1.18	2.05	2.10	3.87
	8	1.36	1.55	2.15	2.71	4.27
Low-carbon steel St.37	2	9.12	8.31	9.58	10.24	12.98
	4	8.29	9.00	10.76	12.72	21.89
	8	x	x	x	x	x
CP titanium Gr.2	2	0.53	0.51	0.64	0.72	0.92
	4	0.45	0.51	0.65	0.76	1.06
	8	0.42	0.44	0.44	0.57	1.02

The plotted data in Figure 3.3 confirm that the trends vary as the factorial difference indicates. The trends predicted by the model do not correspond with the experimental observations. For Stainless steel, Low-carbon steel, and CP titanium (Figure 3.2 A, (c), and (d), respectively), the model (dotted lines) predicts sublinear growth. In contrast, the experimental data (solid lines) show linear growth. This discrepancy in trends becomes more pronounced at 8.0 mT .

Similarly, the same methodology is applied to Figure 3.4, plotting temperature against the field amplitude. The data suggest that the trend predicted by the analytical model does align with the experimental results. Both the model and the experimental results show superlinear growth. However, discrepancies between the analytical model and the experimental results can be identified.

Due to the inconsistencies in the factorial difference, the correction factor could not be implemented in this model.

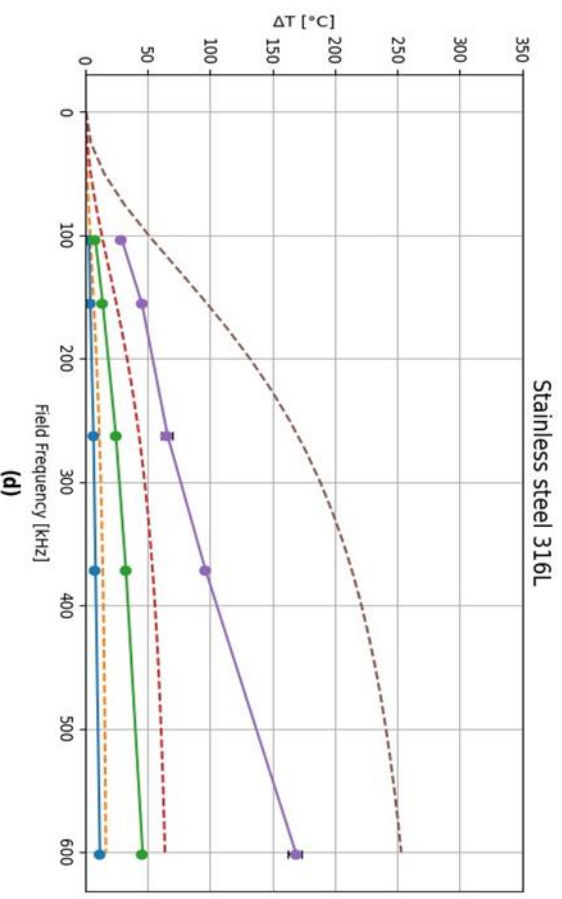
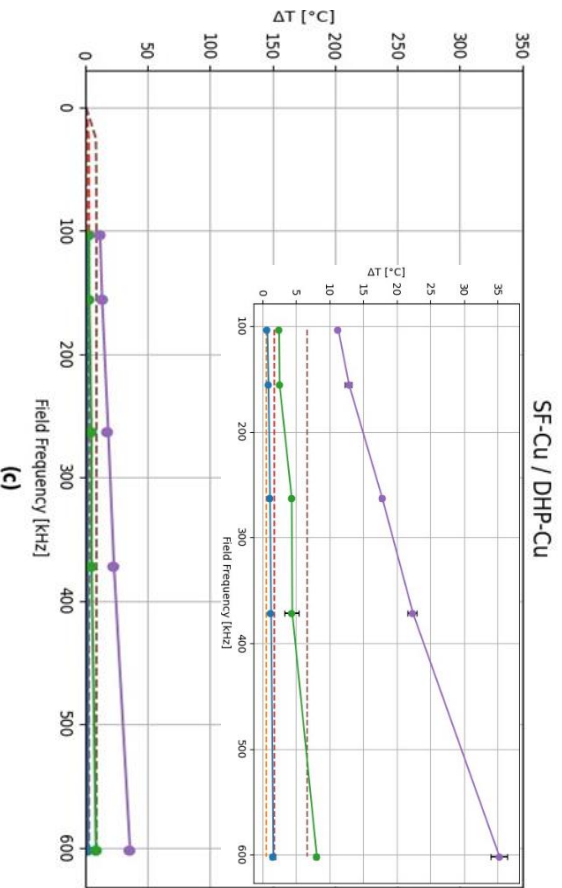
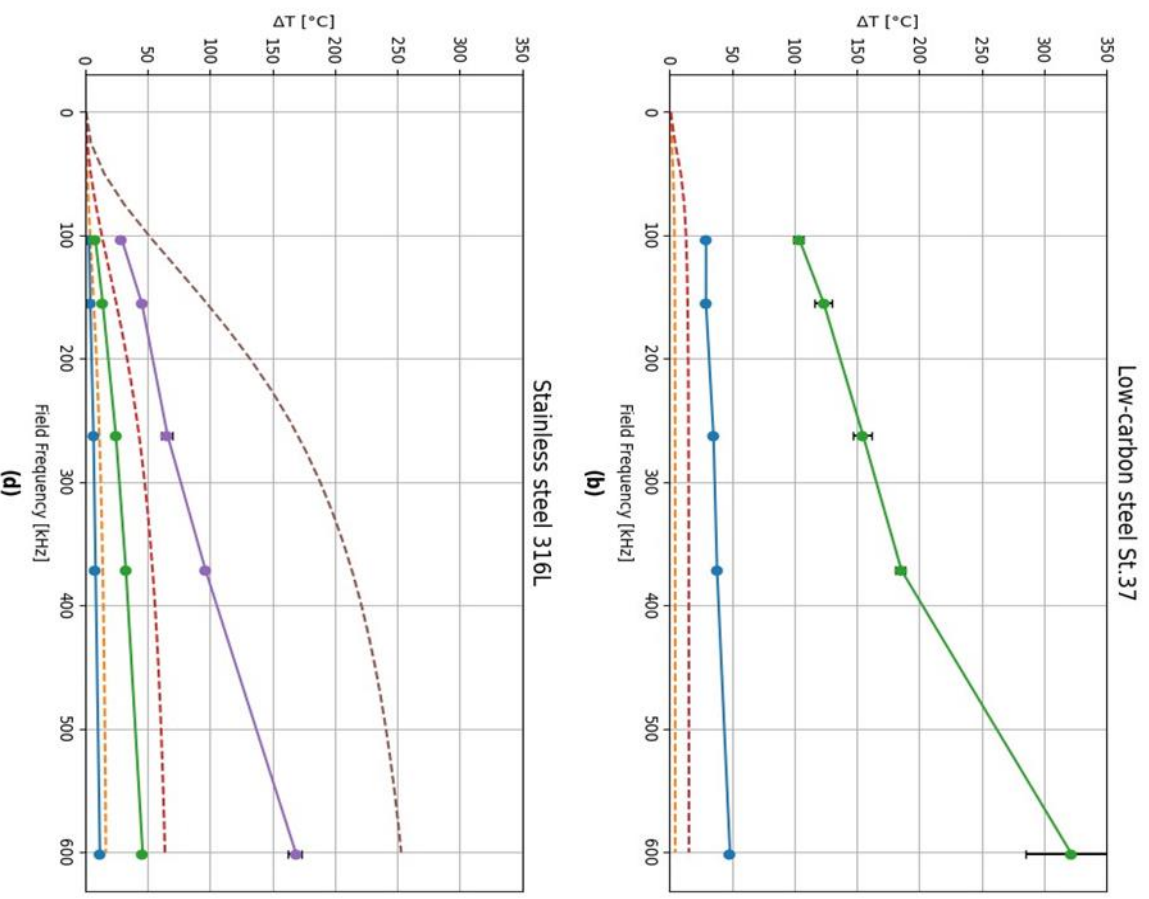
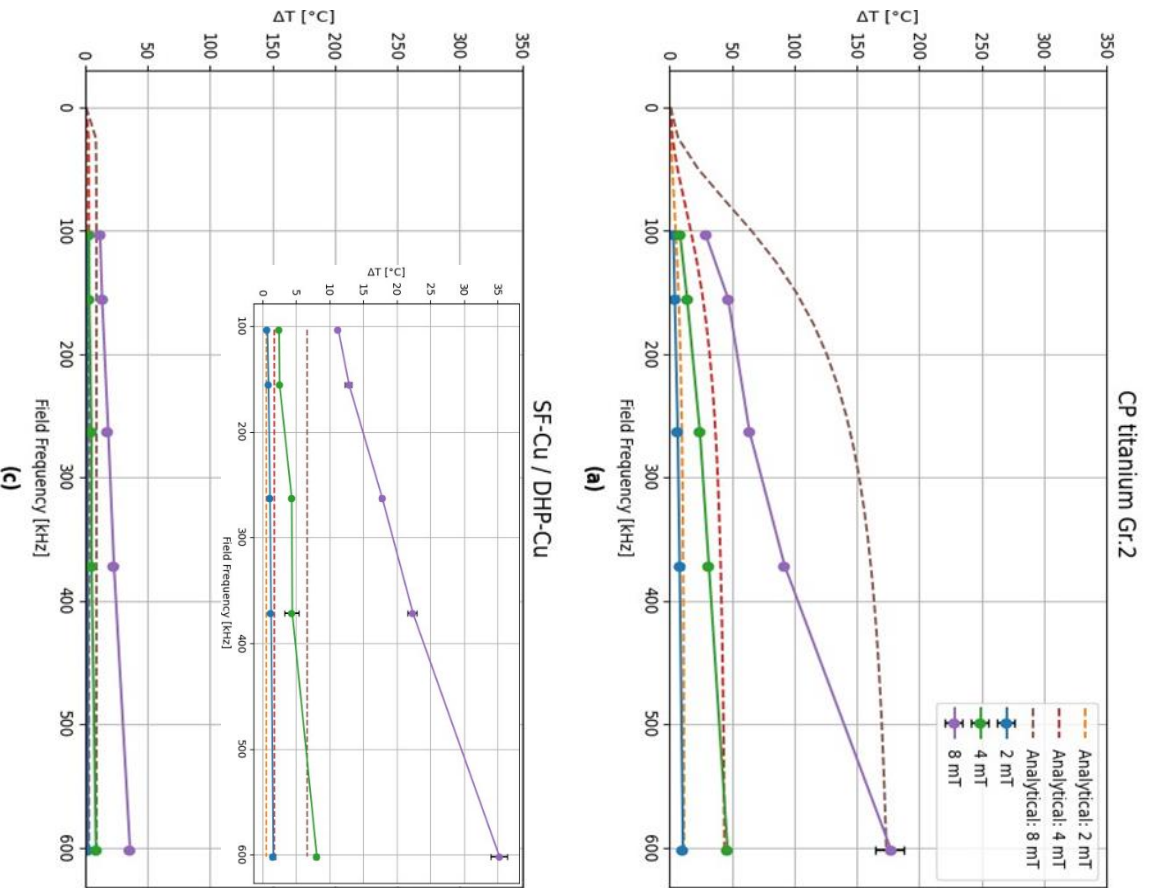


Figure 3.3 Temperature increase over the field frequency for different materials: (a) Stainless steel, (b) SF-Cu / DHP-Cu, (c) Low-carbon steel ST. 37 (Note that the values for 8.0 mT could not be obtained), (d) CP titanium Gr. 2.

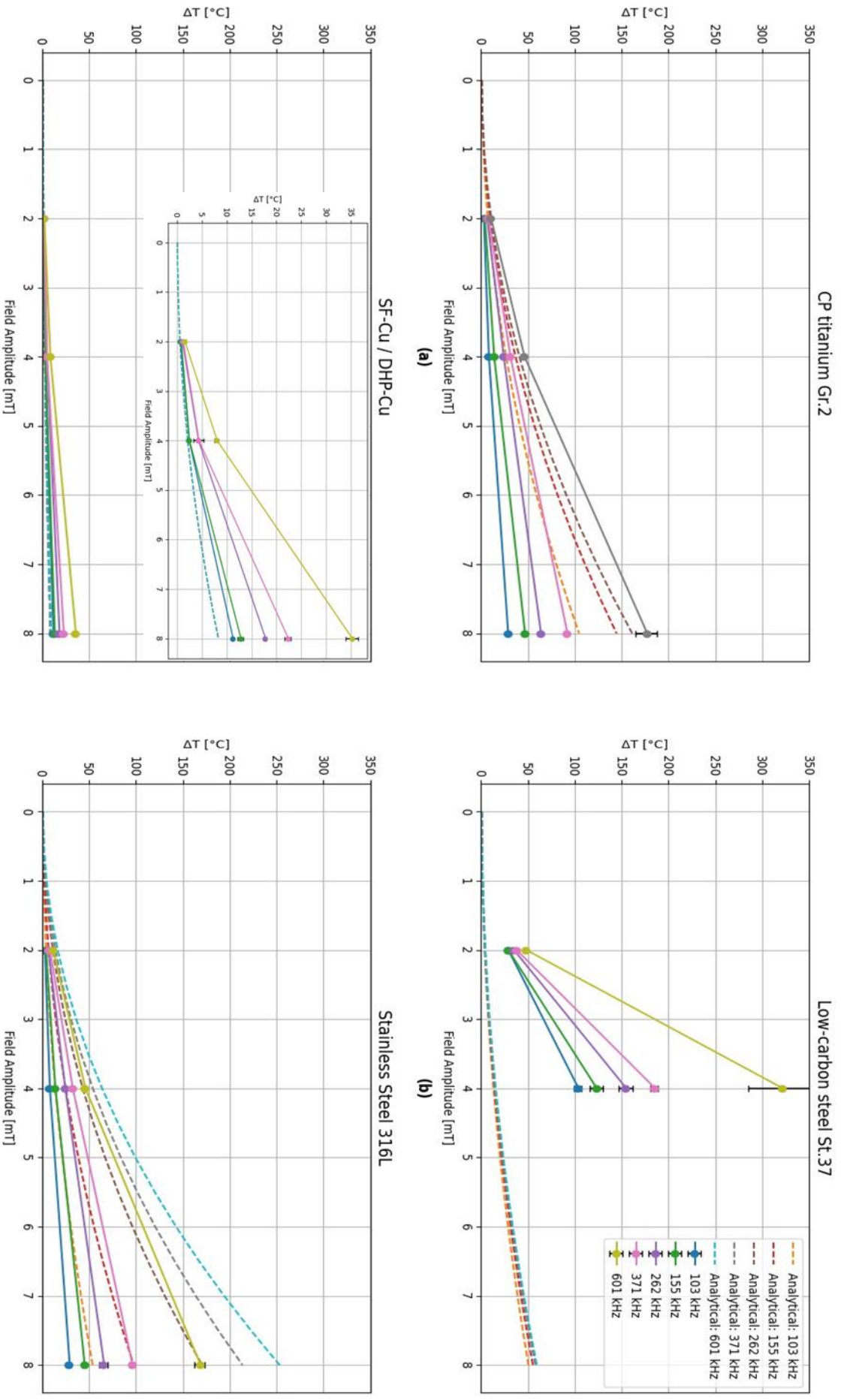


Figure 3.4 Temperature increase over the amplitude for different materials: (a) Stainless steel, (b) SF-Cu / DHP-Cu (Only one line is presented for the analytical solution of SF-Cu / DHP-Cu since the model assumes constant frequency-independent temperature increases), (c) Low-carbon steel ST. 37, (d) CP titanium Gr. 2

3.3 Phase III: Targeted IH

This section presents the results from the targeted induction experiment. The procedure involved recording the initial temperature of the specimen (titanium rod with low-carbon steel ST. 37 ring) and comparing it with a temperature after a *60 seconds* exposure to an AMF. The corresponding field parameters are also provided. The experiment utilized a multi-material specimen of Titanium Grade 23 and Low-carbon steel ST. 37. A control test was conducted using a pure Titanium Gr. 23 cylinder without any Low-carbon steel St. 37 ring. The results are shown in Figure 3.5.

The experimental data reveals temperature differences between the negative control test and the multi-material specimen. The most significant differences were with higher field parameters. At the settings 4.0 mT and 371 kHz , the temperature difference surpasses $11\text{ }^{\circ}\text{C}$. This difference between the negative control and the multi-material specimen becomes even more noticeable with the settings 4.0 mT and 601 kHz , here the difference is more than $22\text{ }^{\circ}\text{C}$. These differences were calculated based on the average surface temperatures recorded for each specimen.

The temperature response to magnetic fields is intensity-dependent. However, significant temperature differences were only discernible at the highest field settings explored in this study. At lower field settings, the temperature variations between the negative control and the multi-material specimens were either negligible or completely absent.

Although a temperature gradient across the multi-material specimen was also hypothesized, thermal readings over *60 seconds* demonstrated even temperature distribution across its surface. This uniformity indicates that the multi-material specimen does not exhibit localized heating or cooling in response to the applied field conditions within the observed time frame.

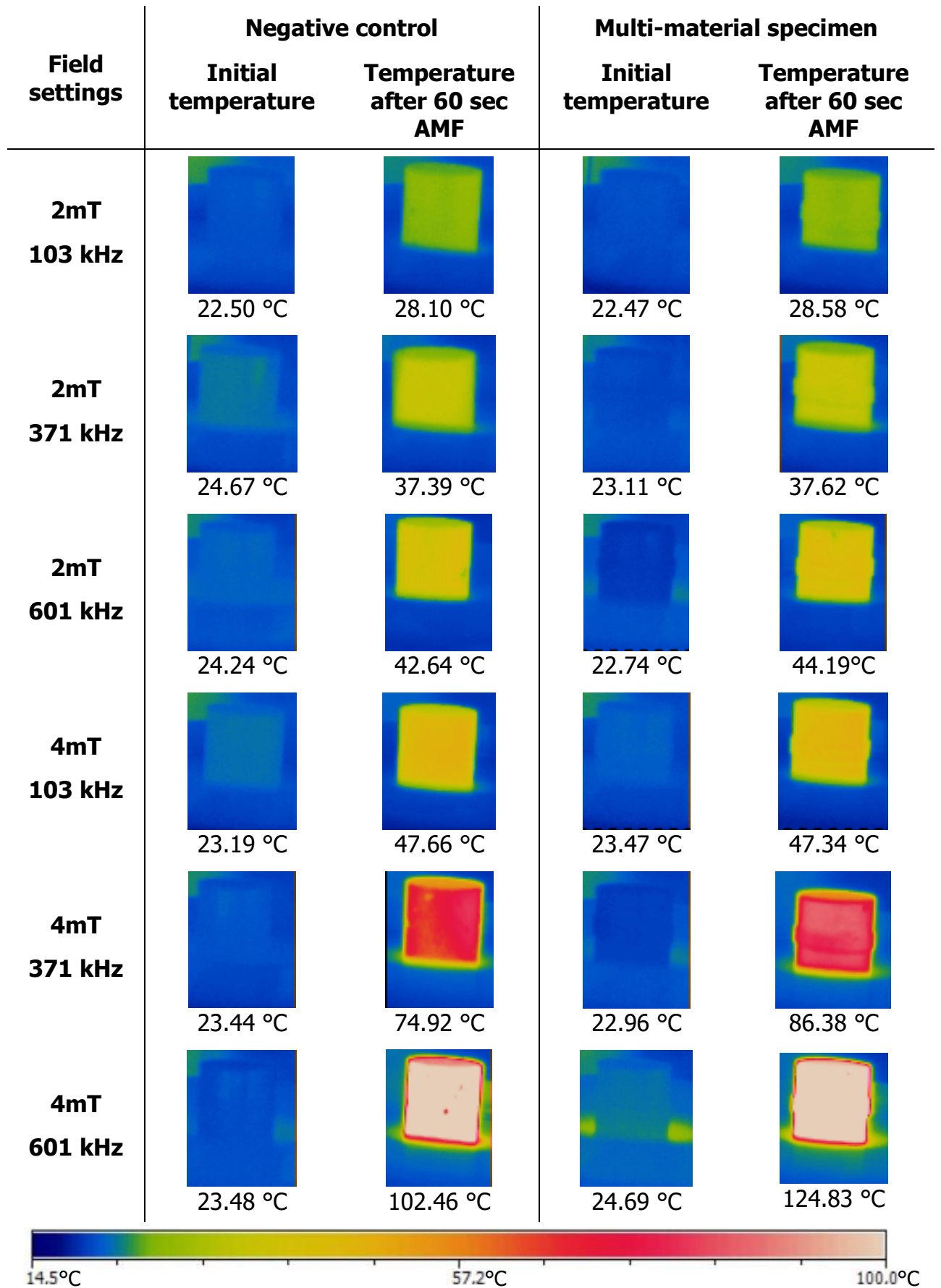


Figure 3.5 Thermal readings with mean value of the surface temperature of the targeted induction heating experiment before the exposure and after the AMF exposure at various magnetic field strengths and frequencies.

4 Discussion

4.1 Phase II: Induction Trials

Material Properties Analysis

The observed deviations between documented material properties and experimental measurements are a stark reminder of the importance of comprehensive characterization and understanding of material behavior. In scientific literature, material properties are often generalized based on average compositions and processing methods, overlooking the inherent variability introduced by different suppliers and manufacturing processes. This underscores the necessity for further research in this area [28].

The discrepancy in copper specimens, where higher aluminum content was detected through XRF analysis, underscores the necessity for thorough material analysis. The presence of aluminum, as an impurity, significantly impacts the electrical resistivity of the alloy [29]. This finding aligns with the well-established principle that impurities in metals can hinder electron mobility, thereby reducing conductivity [30]. The higher resistivity observed in the experimental measurements compared to literature values can be attributed to this deviation in chemical composition [31].

Furthermore, the influence of heat treatments on material properties might also explain the observed deviations between the reported and experimentally determined properties in CP titanium Gr. 2 specimens [32]. Heat treatments can induce changes in microstructure and crystallographic properties, affecting mechanical, thermal, and electrical characteristics [33]. In the case of CP titanium, the lower resistivity observed may be attributed to the specific heat treatment regimen employed, altering the material's conductivity [32].

Incorporating measured material properties into the analytical model can achieve a more accurate model of the system's behavior. This emphasizes the importance of experimental validation and calibration, ensuring that models accurately reflect the experimental conditions.

IH Experiments

The induction trials were performed with Stainless steel 316L, Low-Carbon Steel ST. 37, SF-Cu/DHP-Cu, and CP titanium Gr. 2. Other relevant biomaterials, such as medical-grade CoCr alloy and Ti6AL4V (Ti Grade 23) [34], were not included due to limited specimen availability.

SF-Cu/DHP-Cu was the least thermally responsive among the four tested materials. This low responsiveness can be attributed to copper's low electrical resistivity [35]. In equation 1.5, resistivity linearly influences the power generated by a workpiece during the IH process. Copper's measured resistivity at $2.14 \cdot 10^{-2} \text{ } \Omega \cdot \text{m}$, is lower than the resistivity of other materials included in the study (Table 3.3).

CP titanium and Stainless steel 316L exhibited similar behavior during the IH process, although titanium, on average, had 9.89 % lower response than stainless steel. The electrical conductivities of these two materials are within the same order of magnitude, with the measured resistivity of CP titanium at $4.64 \cdot 10^{-1} \text{ } \Omega \cdot \text{m}$ and that of stainless steel at $7.48 \cdot 10^{-1} \text{ } \Omega \cdot \text{m}$. Therefore, their comparable responses may be attributed to the similarity in resistivity levels, later demonstrated by the analytical "Model 1," with CP titanium showing a slightly lower overall response.

However, a closer examination reveals a more pronounced discrepancy at a field amplitude of 4.0 mT . This variation suggests that other factors beyond resistivity, possibly involving CP titanium's magnetic properties or microstructural characteristics, may influence its heating behavior at specific field amplitudes [36], [37].

Low-carbon steel ST. 37 exhibited the most significant thermal response among the four materials tested in this study. Despite having a lower electrical resistivity than stainless steel and CP titanium, which, according to equation 1.5, would typically result in a lower power output and consequently less temperature increase, low-carbon steel demonstrated the highest thermal response. This higher response can be attributed to low-carbon steel being the only ferromagnetic material in this study, paramagnetic stainless steel, CP titanium, and diamagnetic copper. Ferromagnetic materials are subject to Eddy current heating and magnetic hysteresis [16]. Combining these two mechanisms contributes to the substantial heat production in low-carbon steel.

As a material for MFH, low-carbon steel ST. 37 (as a substitute for pure iron) could enhance the efficiency of MFH in eradicating bacterial biofilms. Research indicates that achieving a temperature of $70\text{ }^{\circ}\text{C}$ for 210 seconds is necessary to kill a colony of *Staphylococcus aureus*, *Staphylococcus epidermidis*, *Pseudomonas aeruginosa*, *Bacillus cereus*, and yeast *Candida albicans* completely [13]. The experimental data confirm that low-carbon steel 37 most swiftly achieves this $70\text{ }^{\circ}\text{C}$ thermal threshold. The exposure time also dramatically influences the efficiency of the MFH treatment. Research showed that at $60\text{ }^{\circ}\text{C}$ *Candida albicans* can be reduced with factor $8 - \log$ after 30 seconds [13]. This same reduction (factor $8 - \log$) of pathogens can be achieved after 120 seconds for *Staphylococcus epidermidis*, *Pseudomonas aeruginosa*, and *Bacillus cereus* (at $60\text{ }^{\circ}\text{C}$) [13]. *Staphylococcus aureus* could be reduced with factor $8 - \log$ after 180 seconds [13]. The reduction of *Staphylococcus epidermidis* was even more efficient with the combination of MFH and antibiotics [11].

Not all materials included in this study could reach the limit of $60\text{ }^{\circ}\text{C}$ after 300 seconds ; The SF-CU / DHP-Cu specimen could only achieve a temperature of $35.2 \pm 1.2\text{ }^{\circ}\text{C}$ at the amplitude of 8.0 mT and frequency of 601.6 kHz . Stainless steel 316L and CP titanium Gr. 2 reached this threshold with medium settings of amplitude 8 mT and frequency 261.7 kHz after 300 seconds , Low-carbon steel ST. 37, however, reached this limit amply, with an amplitude of only 4.0 mT and frequency of 103.5 kHz . Therefore, ST. 37 proved to be the most responsive material.

A temperature range of $60\text{ to }80\text{ }^{\circ}\text{C}$ is most effective for killing bacteria while minimizing tissue damage [11], [12], [13], [17]. Theoretically, all the materials studied can achieve this optimal temperature with sufficient exposure time. However, the duration of exposure is also crucial in determining the extent of tissue damage, which can be calculated using the CEM(Temp) for different tissues [12], [38]. Therefore, materials with a higher thermal response, such as CP titanium Gr.2, Stainless steel 316L, and ST. 37, are preferred over SF-Cu / DHP-Cu. Although all these materials can reach temperatures exceeding the optimal range of $60\text{ to }80\text{ }^{\circ}\text{C}$ applying a pulsed AMF can help maintain the desired temperature. This approach allows the implant to cool down between pulses, reducing the risk of overheating and enabling the dissipation of possible hot spots into the bulk of the implant.

It is critical to note that this study's conclusions are drawn under assuming the geometry described in Figure 2.1 specifically. This assumption is a notable limitation, as an implant's thermal response can vary significantly with changes in its geometry and volume [19].

Moreover, magnetic hyperthermia's applications extend beyond thermal ablation, such as drug release mechanisms [14]. For these applications, a lower thermal response might be preferable to prevent the denaturation of the released drugs [39]. In addition, studies have demonstrated the efficacy of treatments that employ lower temperatures with longer exposure times in combination with antibiotics [11], [15], suggesting that high thermal responsive materials might not always be the most appropriate choice. Thus, while ST. 37 shows high thermal responsiveness; this does not imply that it is universally the best material for all types of implants and applications.

Furthermore, during the IH experiments conducted in this study, a catalyzed corrosion process was observed in low-carbon steel, raising concerns about its long-term viability and performance in clinical settings. In using pure iron as a biomaterial, it is considered that it corrodes and eventually dissolves in the human body [40]. The process of magnetic hyperthermia raises the corrosion rate due to the raised temperature, which increases electron movement and, thus, corrosion [41]. This increased corrosion rate should be taken into account. This finding underscores the complexity of material selection for magnetic hyperthermia and highlights the necessity of a comprehensive evaluation that includes thermal properties and the material's behavior under operational conditions.

Statistical Analysis

The significant main effect of material on the response confirms that different materials can have different thermal responses with the same field parameters. This underlines the importance of selecting a suitable biocompatible material for orthopedic implants.

The lack of a significant interaction between Material and Frequency suggests that biocompatible materials' response to different AMF frequencies is stable. This stability is particularly beneficial in a medical context, as it allows for greater flexibility in choosing operating frequencies that minimize interference with other medical devices or patient discomfort without requiring extensive recalibration for different implant materials.

The significant interaction between Material and Amplitude highlights the critical need to adjust amplitude settings to the specific material properties of the implant. In the sensitive environment of a living patient, precise control over the amplitude is necessary to prevent overheating, which can lead to tissue damage or other adverse effects.

This interaction underlines the need to carefully coordinate these factors to optimize heating efficiency without compromising patient safety. For orthopedic implants, where uniform heating is critical for therapeutic effectiveness, adjusting these parameters to match the specific thermal characteristics of the implant material can enhance treatment outcomes and minimize risks.

For medical applications involving IH of orthopedic implants, advanced control systems that can dynamically adjust both frequency and amplitude based on real-time feedback regarding the temperature of the implant and surrounding tissues are recommended. Multiple studies presented an example of such a system [17], [42]. This system acts as an automatic safety switch when boiling is detected, preventing thermal damage to biological tissues and potentially leading to implants specifically designed for optimal response to IH.

4.2 Phase II: Analytical Modeling

The results in section 3 stress the criticality of precise parametric inputs in accurately predicting outcomes. Such inputs include the specimen's geometries, chemical composition, and postprocessing techniques (such as heat treatment), which may then profoundly influence other material physical properties like resistivity and thermal conductivity [18]. Even minor quantities of alloying elements can dramatically alter these properties [18]. This study's model predictions aligned more closely with the experimental results observed in the induction trials by measuring these parameters.

The evaluation of the models via vector potentials allows for comparing all included models. Since all models followed similar trends, it can be assumed that the models are correctly derived. Furthermore, as the FEM analysis best represents the real-world scenario, the comparison between "Model 2" and the FEM analysis demonstrates how well the analytical model matches the real-world scenario. Given the similarity in vector potentials, it can be concluded that "Model 2" is a good approximation of the real-world problem. Additionally, since the vector potential of "Model 1" aligns well with "Model 2," it is also considered a good approximation.

The comparison between the induction trials and analytical "Model 1" aimed to assess the accuracy of a one-dimensional analytical model describing the heating of an infinitely long and infinitely thin-walled tube. While the model theoretically describes this ideal geometry, it is essential to note that our experimental setup approached this by selecting a quasi-endless long tube with a ratio of 1:10 diameter x length with a thin wall ratio of 1:4 wall thickness x outer diameter, but inevitably deviated from it. Consequently, differences between the analytical model and real-life experiments are to be expected. Reducing the discrepancies observed between the models could potentially be achieved by using a specimen that is both longer and has thinner walls. However, practical constraints posed by the inner setup of MagneTherm and the limitations of the fabrication processes did not allow it.

Analyzing the factorial difference, it becomes evident that the model performs most accurately for Stainless steel and CP titanium. The values for these two materials are approaching 1.0 as the frequency increases, this suggests the model becomes more reliable at higher frequencies, although it still does not achieve perfect accuracy. This alignment is logical since stainless steel and CP titanium are the only two paramagnetic materials considered. Still, the model exhibited discrepancies with factorial differences ranging from 1.0 to 3.0. This is expected given the model's simplified nature for these two materials. However, upon inspecting the graphs in Figure 3.2 (a) and (d), it is apparent that the correlation between frequency and temperature increase for both the analytical model and real-life measurements is wrong. This discrepancy indicates that the model is unsuitable for precise predictions. A more in depth comparison study on these two particular materials is presented in Jusoh *et al.* [43].

Since the material properties used in this study have inherent uncertainties, the propagated error in the calculation of the temperature increase is also provided. Consequently, the factorial difference can vary based on the actual error. This variation underscores the importance of considering measurement uncertainties when interpreting the results, as they can significantly impact the accuracy and reliability of the thermal response predictions.

Notably, the analytical model doesn't incorporate hysteresis, leading to underestimating the Low-carbon steel experiment due to its ferromagnetic nature. The low-carbon steel specimen undergoes two different heating mechanisms, namely Eddy current heating and hysteresis loss, for which hysteresis loss is not accounted. This explains why the model underestimates the temperature increase for this particular material. The experimental results exhibited significant deviations from the predicted values, with a maximum factorial difference of 18.0, underscoring the model's inadequacy for ferromagnets.

The model predicts a frequency-independent temperature increase for copper, consistent with its placement in the first domain as described in Equation 3.1. However, the real-life experiments demonstrated frequency-dependent behavior in temperature increase, as evidenced by both the factorial difference table (Table 3.7) and the temperature increase over the frequency graph (Figure 3.3 (b)).

Moving on to Figure 3.4, the model demonstrates its ability to predict the correlation between field amplitude and temperature increase. Nonetheless, variations are still observable, suggesting that while the model captures the general trend, it lacks precision in predicting specific outcomes. This trend indicates that the model's predictive capability varies significantly across different materials and is influenced by the frequency of the applied magnetic field, with notable implications for its applicability and reliability in accurately forecasting temperature dynamics under varying conditions.

When analyzing the factorial difference, it becomes evident that the model performs most accurately for Stainless steel and CP titanium. The values for these two materials are approaching 1.0 as the frequency increases, this suggests the model becomes more reliable at higher frequencies, although it still does not achieve perfect accuracy. This alignment is logical since stainless steel and CP titanium are the only two paramagnetic materials considered. Still, the model exhibited discrepancies with factorial differences ranging from 1.0 to 3.0. This is expected given the model's simplified nature for these two materials. However, upon inspecting the graphs in Figure 3.2 (a) and (d), it is clear that there is very little correlation between the analytical model and real-life measurements. This discrepancy indicates that the model is unsuitable for precise predictions of this scenario.

One of the likely limitations is the absence of a hysteresis mechanism in the analytical model, leading to an underestimated heating potential of Low-carbon steel. Due to its ferromagnetic nature, the low-carbon steel specimen undergoes both heating mechanisms: Eddy current heating and hysteresis loss [44]. The experimental results of this material exhibited significant deviations from the predicted values, with a maximum factorial difference of 18.0, featuring the model's inadequacy for ferromagnets.

The model predicts a frequency-independent temperature increase for copper, consistent with its placement in the first domain as described in Equation 3.1. However, the real-life experiments demonstrated frequency-dependent behavior in temperature increase, as evidenced by both the factorial difference table (Table 3.7) and the temperature increase over the frequency graph (Figure 3.3 (b)).

Finally, the model demonstrates its ability to predict the correlation between field amplitude and temperature increase. Nonetheless, variations are still observable, suggesting that while the model captures the general trend, it lacks precision in predicting specific outcomes for various materials of different properties.

4.3 Phase III: Targeted IH

This phase aimed to explore the feasibility of applying targeted IH to hip implants, explicitly focusing on the neck of the femoral component. However, this technique could also be used for other (cylindrical) metallic implants, e.g., external fixators.

This research introduces a refined method for selectively heating specific regions of an implant, building on the foundational work of Pijls *et al.* [12]. Their study demonstrated the effectiveness of concentrating the magnetic field on designated areas. However, that approach's precision to target specific regions remains relatively low, affecting more extensive areas than intended. Additionally, their method requires invasive surgery to position a coil close to the targeted area. The concept proposed in this thesis aimed to concentrate the heated region into smaller areas by materials selection, thereby reducing the potential for damage to surrounding tissues. Additionally, this enhanced method could be implemented non-invasively.

An alternative approach to achieve localized implant heating involves strategically placing ridges, edges, or other structural modifications. These features are designed to induce current peaks, which result in localized hotspots due to the edge effect, as outlined in section 1.3 of our analysis. This effect has been shown through both FEM analysis and practical experiments conducted in the study by Chopra *et al.* [17], but has not yet been strategically used for targeted induction heating. Such targeted heating may improve the precision of thermal therapies and minimize the thermal impact on adjacent non-targeted tissues [12].

In the thermal data illustrated in Figure 3.5, the control test demonstrated a similar pattern of increased heating with rising field frequency and amplitude, with field amplitude exerting a more pronounced influence on the thermal response. This observation aligns with theoretical expectations, as field amplitude impacts the thermal response quadratically (a relationship confirmed through induction trials and Analytical "Model 1"). However, a notable divergence of over 11 °C was observed between the negative control and the multi-material specimen under higher field settings, especially at 4.0 mT amplitude and frequencies of 371 and 22 °C at 601 kHz with the same amplitude, where the multi-material specimen exhibited a significantly higher thermal response than the control.

This more significant response was anticipated due to the ferromagnetic coating on the multi-material specimen, which benefits from a dual heating mechanism detailed in Section 4.1. The ferromagnetic properties of the coating enable it to respond more robustly under higher field amplitudes. The total power generated by the hysteresis loop is proportional to the area enclosed by this loop (Figure 1.4). The hysteresis loss is maximized at saturation, which for ST. 37 lies around 2.2 T [45], because the loop area is the largest. As in this study, the hysteresis loss is minimal when operating at small amplitudes, well below saturation. However, as the amplitude increases towards saturation, the loop area expands, leading to more significant energy loss as heat [46]. This relationship highlights the increasing impact of hysteresis loss with higher amplitudes.

However, it is crucial to consider specific safety limits when applying an alternating magnetic field (AMF) to patients. The Atkinson–Brezovich limit, which sets a maximum product of AMF frequency and field amplitude at $4.85 \cdot 10^8 \text{ A} \cdot \text{m}^{-1} \cdot \text{s}^{-1}$, is generally accepted as a threshold for human application without causing discomfort [47]. Other research suggests that this limit can be increased to $9.59 \cdot 10^9 \text{ A} \cdot \text{m}^{-1} \cdot \text{s}^{-1}$ [48]. However, these studies do not account for scenarios involving larger metallic implants, which could significantly affect the treatment's safety and efficacy. These limits will need to be established.

Although an increased temperature rise was observed, a differentiation in temperature between the Ti bulk and ST. 37 was not observed. This lack of observed temperature differentiation at low field parameters could be attributed to several factors. Firstly, the absence of real-time thermal imaging meant that any transient heat generated by the ferromagnetic coating could have rapidly dissipated into the titanium bulk and vice versa, given the coating's thinness and high thermal conductivity. Therefore, while the initial hypothesis has not been proven untrue, the experimental setup may have been inadequate to detect such subtle variations in temperature. Further investigations, possibly incorporating real-time thermal imaging, are necessary.

Moreover, the coating's volume was significantly lower than the overall specimen. The efficiency of IH depends on material responsiveness and the volume of the material present [19]. The reduced volume of the low-carbon steel coating meant that even if the induction process adequately heated it, the absolute quantity of heat generated would be insufficient to show a significant effect compared to the larger mass of the titanium cylinder.

While there are significant benefits to combining ST. 37 with an implant to locally heat the area via IH, there are also notable downsides. One primary concern is the risk of galvanic corrosion when pure iron is combined with Ti6Al4V [49]. The different electrochemical potentials of these metals create a significant risk of galvanic corrosion [49], especially under induction heating conditions [50].

This corrosion risk is catalyzed by induction heating, which increases the flow of electrons and raises the temperature of the implant. The elevated electron flow accelerates the anodic reaction on the iron's surface, leading to a faster corrosion rate [50]. Additionally, the localized heating can enhance the reactivity of the metals and increase the conductivity of the electrolyte, further accelerating the corrosion process [50].

The formation of corrosion products, particularly iron oxide, can significantly weaken the structural integrity of the implant [51]. This weakening can compromise the implant's mechanical stability and longevity [51]. Moreover, high doses of iron oxide released into the body can have local toxic effects [52].

In summary, while the use of ST. 37 for induction heating in implants shows potential in achieving targeted induction heating; it is crucial to address and mitigate the risks associated with galvanic corrosion to ensure the safety and effectiveness of the implant. Options might include using ferromagnetic materials with closer electrochemical properties (standard electrode potentials), applying protective coatings to inhibit corrosion, or redesigning the implant to minimize direct electrical contact between the different metals [49]. These measures would help ensure the durability and safety of implants under conditions where IH is used.

5 Conclusion

To apply magnetic field hyperthermia for biofilm eradication in IAI, understanding the thermal response of implants under various conditions is essential. Critical parameters, including field amplitude, field frequency, and implant material, significantly affect the technique's effectiveness and safety. This study used *in silico* models, analytical models, and FEM analysis to investigate these influences.

The study found that simplified analytical models could approximate the thermal response of metallic implants, especially those made of paramagnetic materials with simple geometries. For instance, Low-carbon steel ST. 37 demonstrated rapid heating, with a temperature rise of $321.2 \pm 36.51 \text{ }^\circ\text{C}$ at 4.0 mT and 601.6 kHz , making it highly suitable for magnetic hyperthermia. However, materials with lower electrical resistivity, such as copper, produced forty times less heat (a temperature increase of only $8.0 \pm 0.4 \text{ }^\circ\text{C}$ at the same settings).

The study highlighted that analytical models could only predict simple implant geometries within two to three orders of magnitude, recommending FEM analysis for more complex geometries and precise predictions. The amplitude and frequency of the AMF play crucial roles, with increasing field amplitudes increasing heat generation quadratically.

Furthermore, while a temperature difference between the coating and bulk material was not observed in targeted induction heating experiments, more research with real-time thermal imaging is necessary to validate the hypothesis. The effectiveness of AMF for non-contact induction heating of metallic implants depends on carefully selected frequencies and amplitudes, as well as the specific geometrical attributes of the implant.

6 Recommendation

Thermal ablation of biofilms through non-contact IH is viewed as a promising solution for enhancing the antimicrobial properties of implants. Yet, to fully harness its potential, further research is necessary. Insights gained from understanding the impact of material properties and field parameters on the thermal response of workpieces are invaluable. A focused research effort should be undertaken where both the coil and the implant are designed simultaneously. The implant's geometry can be tailored to suit selected materials. At the same time, the coil should be capable of generating a sufficiently strong magnetic field at the right frequency to induce the desired thermal response.

Moreover, it is imperative to study the potential side effects of magnetic hyperthermia for the application of thermal ablation of biofilms with implants in a living organism (in vivo). One critical concern is the tissue damage from the implant heating up. The optimal conditions for magnetic hyperthermia must be carefully selected to maximize bacterial eradication efficiency. This involves determining whether IH should be applied in short pulses at higher frequencies or as continuous periods at lower frequencies. Despite several studies exploring these parameters, more research is needed to refine these approaches.

Patient safety considerations are paramount. Before advancing the design of any magnetic IH system, it is crucial to establish and adhere to safety limits. These limits must encompass all potential biological effects and ensure that the thermal management of the implant does not compromise patient health.

Expanding the range of materials studied could significantly benefit this research. It is recommended that Titanium Gr. 23 and Cobalt-Chromium (CoCr) alloys prevalent in orthopedic implants be included. Moreover, exploring the use of 3D-printed titanium is suggested, given the potential of additive manufacturing to create patient-specific implant designs that could also optimize IH properties.

Despite initial setbacks with targeted IH experiments, this technique is believed to be successfully implemented. Targeted IH might be achieved by strategically utilizing the 'edge effect,' where grooves or edges on an implant increase the current density and thus create localized hot spots. This approach, however, requires careful consideration, as bacteria tend to colonize these grooves as well. Proper design and testing are crucial to balance the thermal properties with geometric modifications to prevent unintended biofilm formation in these new niches.

Finally, while the path forward involves complex challenges, the integration of tailored material properties, optimized geometric designs, and precise control of induction parameters may pave the way for breakthroughs in implant technology that can effectively combat implant-associated infections.

7 Acknowledgements

I am sincerely grateful for the opportunity to work on a project that perfectly aligns with my interests in orthopedic implants from a theoretical perspective. This thesis would not have been possible without the guidance and supervision I received.

Foremost, I extend my most profound appreciation to my primary supervisor, Dr. Ir. I. Apachitei, whose outstanding supervision and comprehensive oversight were instrumental throughout the project. His expertise steered this research effectively and enriched my learning experience immensely.

I am equally thankful to my daily supervisor, Ir. M. Šalandová. Her diligent guidance through the thesis process and personal support motivated me. From her, I have gained significant insights into scientific writing, learned how to establish the correct protocols, and acquired the proper methods required for my field.

Additionally, my heartfelt thanks go to Prof. Dr. Ir. L. Abelmann, whose assistance was crucial in overcoming the challenges I faced with the electrical and physics aspects of my topic, "Thermal Ablation of Biofilm on Metallic Implants with Non-Contact Induction." Prof. Abelmann patiently taught me the fundamental principles of IH and contributed directly to my thesis by helping me derive equations for the analytical model and construct a Freefem++ analysis.

I want to thank Sander Leeflang for his expert guidance in ensuring the experiments were conducted safely. His oversight was indispensable in maintaining a secure environment throughout the experimental process. I also thank Ruud Hendrix for his skilled execution of the XRF analysis. His meticulous work was crucial in providing detailed insights that significantly enhanced the understanding of our results.

Finally, I want to thank my two good friends, Bart Klootwijk and Wouter Bentvelsen, for helping me with some Python coding and supporting me throughout the thesis.

The knowledge and skills I acquired under their mentorship have filled the gaps I felt during my master's program. I am genuinely grateful to have learned so much about this topic, which has fulfilled my primary goal of undertaking this thesis.

References

- [1] R. P. Runner *et al.*, "Prosthetic Joint Infection Trends at a Dedicated Orthopaedics Specialty Hospital," *Adv Orthop*, vol. 2019, pp. 1–9, Feb. 2019, doi: 10.1155/2019/4629503.
- [2] H. Maradit Kremers *et al.*, "Prevalence of Total Hip and Knee Replacement in the United States," *The Journal of Bone and Joint Surgery-American Volume*, vol. 97, no. 17, pp. 1386–1397, Sep. 2015, doi: 10.2106/JBJS.N.01141.
- [3] G. Denissen, P. Defesche, and A. Spekenbrink, "LROI Jaarrapportage 2021," 's-Hertogenbosch, 2021.
- [4] Q. Cui, W. M. Mihalko, J. S. Shields, M. Ries, and K. J. Saleh, "Antibiotic-Impregnated Cement Spacers for the Treatment of Infection Associated with Total Hip or Knee Arthroplasty," *J Bone Joint Surg*, vol. 89, no. 4, pp. 871–882, Apr. 2007, doi: 10.2106/JBJS.E.01070.
- [5] R. M. Birlutiu, V. Birlutiu, M. Mihalache, C. Mihalache, and R. S. Cismasiu, "Diagnosis and management of orthopedic implant-associated infection: a comprehensive review of the literature.," *Biomedical Research*, 2017.
- [6] D. Campoccia, L. Montanaro, and C. R. Arciola, "The significance of infection related to orthopedic devices and issues of antibiotic resistance," *Biomaterials*, vol. 27, no. 11, pp. 2331–2339, Apr. 2006, doi: 10.1016/j.biomaterials.2005.11.044.
- [7] D. G. Kennedy, A. M. O'Mahony, E. P. Culligan, C. M. O'Driscoll, and K. B. Ryan, "Strategies to Mitigate and Treat Orthopaedic Device-Associated Infections," *Antibiotics 2022, Vol. 11, Page 1822*, vol. 11, no. 12, p. 1822, Dec. 2022, doi: 10.3390/ANTIBIOTICS11121822.
- [8] H.-C. Flemming and J. Wingender, "The biofilm matrix," *Nature Publishing Group*, 2010, doi: 10.1038/nrmicro2415.
- [9] H. F. Chambers and F. R. DeLeo, "Waves of Resistance: Staphylococcus aureus in the Antibiotic Era," *Nat Rev Microbiol*, vol. 7, no. 9, p. 629, 2009, doi: 10.1038/NRMICRO2200.
- [10] R. K. GILCHRIST, R. MEDAL, W. D. SHOREY, R. C. HANSELMAN, J. C. PARROTT, and C. B. TAYLOR, "Selective Inductive Heating of Lymph Nodes," *Ann Surg*, vol. 146, no. 4, pp. 596–606, Oct. 1957, doi: 10.1097/00000658-195710000-00007.
- [11] B. G. Pijls, I. M. J. G. Sanders, E. J. Kuijper, and R. G. H. H. Nelissen, "Induction heating for eradicating Staphylococcus epidermidis from biofilm," *Bone Joint Res*, vol. 9, no. 4, p. 192, Apr. 2020, doi: 10.1302/2046-3758.94.BJR-2019-0274.R1.
- [12] B. G. Pijls, I. M. J. G. Sanders, E. J. Kuijper, and R. G. H. H. Nelissen, "Segmental induction heating of orthopaedic metal implants," *Bone Joint Res*, vol. 7, no. 11, p. 609, Nov. 2018, doi: 10.1302/2046-3758.711.BJR-2018-0080.R1.
- [13] B. G. Pijls, I. M. J. G. Sanders, E. J. Kuijper, and R. G. H. H. Nelissen, "Non-contact electromagnetic induction heating for eradicating bacteria and yeasts on biomaterials and possible relevance to orthopaedic implant infections: In vitro findings," *Bone Joint Res*, vol. 6, no. 5, pp. 323–330, May 2017, doi: 10.1302/2046-3758.65.BJR-2016-0308.R1/LETTERTOEDITOR.
- [14] J. C. Kwan, R. S. Flannagan, M. Vásquez Peña, D. E. Heinrichs, D. W. Holdsworth, and E. R. Gillies, "Induction Heating Triggers Antibiotic Release and Synergistic Bacterial Killing on Polymer-Coated Titanium Surfaces," *Adv Healthc Mater*, May 2023, doi: 10.1002/adhm.202202807.
- [15] Q. Wang *et al.*, "Alternating magnetic fields and antibiotics eradicate biofilm on metal in a synergistic fashion," *NPJ Biofilms Microbiomes*, vol. 7, no. 1, p. 68, Aug. 2021, doi: 10.1038/s41522-021-00239-y.
- [16] V. Sadaphal *et al.*, "Feasibility of heating metal implants with alternating magnetic fields (AMF) in scaled up models," *International Journal of Hyperthermia*, vol. 39, no. 1, pp. 81–96, Dec. 2022, doi: 10.1080/02656736.2021.2011434.

- [17] R. Chopra *et al.*, "Employing high-frequency alternating magnetic fields for the non-invasive treatment of prosthetic joint infections," *Sci Rep*, vol. 7, no. 1, p. 7520, Aug. 2017, doi: 10.1038/s41598-017-07321-6.
- [18] M. M. Welling *et al.*, "A radio- and fluorescently labelled tracer for imaging and quantification of bacterial infection on orthopaedic prostheses," *Bone Joint Res*, vol. 12, no. 1, pp. 72–79, Jan. 2023, doi: 10.1302/2046-3758.121.BJR-2022-0216.R1.
- [19] V. Rudnev, D. Loveless, and R. Cook, *Handbook of Induction Heating*, 2nd ed., vol. 1. Taylor & Francis Group, 2017.
- [20] S. Lupi, M. Forzan, and A. Aliferov, "Theoretical Background," in *Induction and Direct Resistance Heating*, Cham: Springer International Publishing, 2015, pp. 1–22. doi: 10.1007/978-3-319-03479-9_1.
- [21] E. E. Kriezis, H. D. Tsiboukis, S. M. Panas, and J. A. Tegopoulos, "Eddy Currents: Theory and Applications," *Proceedings of the IEEE*, vol. 80, no. 10, pp. 1559–1589, 1992, doi: 10.1109/5.168666.
- [22] A. A. Kaufman, R. O. Hansen, and R. L. K. Kleinberg, "Chapter 6 Paramagnetism, Diamagnetism, and Ferromagnetism," *Methods in Geochemistry and Geophysics*, vol. 42, pp. 207–254, Jan. 2008, doi: 10.1016/S0076-6895(08)00006-1.
- [23] W. J. Carr, "Energy Loss Resulting from Domain Wall Motion," *J Appl Phys*, vol. 30, no. 4, pp. S90–S91, Apr. 1959, doi: 10.1063/1.2185979.
- [24] M. Ashby, H. Shercliff, and D. Cebon, *Materials*, 3rd ed. Elsevier, 2019. doi: 10.1016/C2016-0-04242-0.
- [25] F. Hecht, "New development in FreeFem++," *Journal of Numerical Mathematics*, vol. 20, pp. 251–265, 2012.
- [26] J. R. Nagel, "Induced Eddy Currents in Simple Conductive Geometries: Mathematical Formalism Describes the Excitation of Electrical Eddy Currents in a Time-Varying Magnetic Field," *IEEE Antennas Propag Mag*, vol. 60, no. 1, pp. 81–88, Feb. 2018, doi: 10.1109/MAP.2017.2774206.
- [27] n.d., "Matweb." Accessed: Mar. 05, 2024. [Online]. Available: <https://www.matweb.com/index.aspx>
- [28] "Advanced Techniques for Materials Characterization," *Materials*, vol. 17, 2024, Accessed: May 20, 2024. [Online]. Available: https://www.mdpi.com/journal/materials/sections/struct_analysis
- [29] n.d., "Online Materials Information Resource - MatWeb." Accessed: Mar. 20, 2024. [Online]. Available: <https://www.matweb.com/index.aspx>
- [30] L. Mari, "Conduction Properties of N-Type and P-Type Semiconductors - Technical Articles." Accessed: May 20, 2024. [Online]. Available: <https://eepower.com/technical-articles/understanding-the-conduction-properties-of-semiconductors/>
- [31] P. J. Ding, W. A. Lanford, S. Hymes, and S. P. Murarka, "Effects of the addition of small amounts of Al to copper: Corrosion, resistivity, adhesion, morphology, and diffusion," *J Appl Phys*, vol. 75, no. 7, pp. 3627–3631, Apr. 1994, doi: 10.1063/1.356075.
- [32] A. Settefrati *et al.*, "Precipitation in a near Beta Titanium Alloy on Ageing: Influence of Heating Rate and Chemical Composition of the Beta-Metastable Phase," *Solid State Phenomena*, vol. 172–174, pp. 760–765, Jun. 2011, doi: 10.4028/www.scientific.net/SSP.172-174.760.
- [33] T. Lipiński, "Quality, Microstructure, and Properties of Metal Alloys," *Materials*, vol. 16, no. 8, p. 3019, Apr. 2023, doi: 10.3390/ma16083019.
- [34] N. J. Hallab and J. J. Jacobs, "Orthopedic Applications," *Biomaterials Science: An Introduction to Materials in Medicine*, pp. 1079–1118, Jan. 2020, doi: 10.1016/B978-0-12-816137-1.00070-2.

- [35] S. Devillers, Q. Lemineur, J. Delhalle, and Z. Mekhalif, "Exploratory study of copper particles electrodeposition on nickel by induction heating," *Electrochim Acta*, vol. 56, no. 14, pp. 4953–4959, May 2011, doi: 10.1016/J.ELECTACTA.2011.03.130.
- [36] I. A. Smolyanov, V. Kotlan, and I. Doležal, "Optimal heat induction treatment of titanium alloys," *COMPEL - The International Journal for Computation and Mathematics in Electrical and Electronic Engineering*, vol. 39, no. 1, pp. 53–65, Mar. 2020, doi: 10.1108/COMPEL-05-2019-0212/FULL/PDF.
- [37] R. Przyłucki and S. Golak, "The Stress Effects Occurring During Induction Heating of Titanium," *Solid State Phenomena*, vol. 211, pp. 149–154, 2014, doi: 10.4028/WWW.SCIENTIFIC.NET/SSP.211.149.
- [38] G. C. Van Rhoon, T. Samaras, P. S. Yarmolenko, M. W. Dewhurst, E. Neufeld, and N. Kuster, "CEM43°C thermal dose thresholds: a potential guide for magnetic resonance radiofrequency exposure levels?," *Eur Radiol*, vol. 23, no. 8, p. 2215, Aug. 2013, doi: 10.1007/S00330-013-2825-Y.
- [39] G. Yang, J. Trylska, Y. Tor, and J. A. McCammon, "Binding of aminoglycosidic antibiotics to the oligonucleotide A-site model and 30S ribosomal subunit: Poisson-Boltzmann model, thermal denaturation, and fluorescence studies," *J Med Chem*, vol. 49, no. 18, pp. 5478–5490, Sep. 2006, doi: 10.1021/JM060288O/ASSET/IMAGES/LARGE/JM060288OF00009.JPEG.
- [40] N. E. Putra, V. Moosabeiki, M. A. Leeflang, J. Zhou, and A. A. Zadpoor, "Biodegradation-affected fatigue behavior of extrusion-based additively manufactured porous iron–manganese scaffolds," *Acta Biomater*, vol. 178, pp. 340–351, Apr. 2024, doi: 10.1016/J.ACTBIO.2024.02.024.
- [41] K. Alasvand Zarasvand and V. R. Rai, "Microorganisms: Induction and inhibition of corrosion in metals," *Int Biodeterior Biodegradation*, vol. 87, pp. 66–74, Feb. 2014, doi: 10.1016/J.IBIOD.2013.10.023.
- [42] B. Cheng *et al.*, "Remote acoustic sensing as a safety mechanism during exposure of metal implants to alternating magnetic fields," *PLoS One*, vol. 13, no. 5, p. e0197380, May 2018, doi: 10.1371/journal.pone.0197380.
- [43] N. M. Jusoh, A. F. M. Noor, S. M. Tajudin, M. H. Din, M. E. Aziz, and W. A. Kamil, "Magnetic remanence of stainless steel and titanium alloy orthopaedic implants," *Malaysian Journal of Fundamental and Applied Sciences*, vol. 17, no. 5, pp. 504–513, Sep. 2021, doi: 10.11113/MJFAS.V17N5.2122.
- [44] C. L. Dennis and R. Ivkov, "Physics of heat generation using magnetic nanoparticles for hyperthermia," *International Journal of Hyperthermia*, vol. 29, no. 8, pp. 715–729, Dec. 2013, doi: 10.3109/02656736.2013.836758.
- [45] A. Hashemi, P. Yazdanpanah Qaraei, M. Dehghani, and H. Taheri, "Optimum design and manufacturing of the lifting cylindrical electromagnets considering magnetic, thermal, and mechanical limitations," *International Journal on Interactive Design and Manufacturing*, May 2023, doi: 10.1007/S12008-023-01491-6.
- [46] A. Muzaffar, K. Deshmukh, and M. B. Ahamed, "MXene-based multifunctional polymer composites for electromagnetic interference shielding applications," *MXenes and their Composites: Synthesis, Properties and Potential Applications*, pp. 649–686, Jan. 2021, doi: 10.1016/B978-0-12-823361-0.00006-X.
- [47] W. J. Atkinson, I. A. Brezovich, and D. P. Chakraborty, "Usable Frequencies in Hyperthermia with Thermal Seeds," *IEEE Trans Biomed Eng*, vol. BME-31, no. 1, pp. 70–75, 1984, doi: 10.1109/TBME.1984.325372.
- [48] B. Herrero de la Parte *et al.*, "Proposal of New Safety Limits for In Vivo Experiments of Magnetic Hyperthermia Antitumor Therapy," *Cancers 2022, Vol. 14, Page 3084*, vol. 14, no. 13, p. 3084, Jun. 2022, doi: 10.3390/CANCERS14133084.

- [49] J. Creus, H. Idrissi, and H. Mazille, "Galvanic corrosion behaviour of mild steel, Al, and Ti in 3%NaCl solution: Application to PVD coatings on steel substrate," *Surface Engineering*, vol. 13, no. 5, pp. 415–419, Jan. 1997, doi: 10.1179/sur.1997.13.5.415.
- [50] K. Kobayashi and N. Banthia, "Corrosion detection in reinforced concrete using induction heating and infrared thermography," *J Civ Struct Health Monit*, vol. 1, no. 1–2, pp. 25–35, Jun. 2011, doi: 10.1007/S13349-010-0002-4/FIGURES/20.
- [51] D. F. Williams, "Corrosion of Implant Materials," *Annual Review of Materials Science*, vol. 6, no. 1, pp. 237–266, Aug. 1976, doi: 10.1146/annurev.ms.06.080176.001321.
- [52] M. Salama, M. F. Vaz, R. Colaço, C. Santos, and M. Carmezim, "Biodegradable Iron and Porous Iron: Mechanical Properties, Degradation Behaviour, Manufacturing Routes and Biomedical Applications," *Journal of Functional Biomaterials 2022, Vol. 13, Page 72*, vol. 13, no. 2, p. 72, Jun. 2022, doi: 10.3390/JFB13020072.
- [53] M. Subramanian, A. Miaskowski, G. Pearce, and J. Dobson, "A coil system for real-time magnetic fluid hyperthermia microscopy studies," *International Journal of Hyperthermia*, vol. 32, no. 2, pp. 112–120, Feb. 2016, doi: 10.3109/02656736.2015.1104732.

8. Appendix

Appendix I: MagneTherm datasheet

nanoTherics		MagneTherm ® Matrix Sheet					Date:	15/12/2022	nanoTherics Ltd.	
MagneTherm Serial #:	1800115-DS2	Single Fibre Optic Cond. Serial#	1122100084	Customer:	Delft University of Technology, Biomaterials and Tissue Biomechanics Section, Department of Biomechanical Engineering, Faculty of Mechanical, Maritime and Materials Engineering Mekelweg 2, 2628 CD Delft, The Netherlands					Brookside Farm, Dig Lane Warrington, Cheshire WA2 0SH United Kingdom
PSU Serial #:	QPX1200SP/571026	Fibre Opt. Probes Serial #	21110276/2110272	Contact:	Dirk Julian Apachei L.Apachei@tudelft.nl					Tel: +44 1925 812554
FG Serial #:	TG2000/562861	Capacitor Set ID	DS2-0031							
OS Serial #:	N/A	VT Pump	163675							
HeatChill Serial#	082245002/0D2239002									
Country:	Netherlands									
Mains V.	230V	18 Turn 50 Coil Serial #	GH1850-0830	HFS Coil Serial #	N/A	External Petri Coil	N/A	e: enquiry@nanotherics.com		
		9 Turn 50 Coil Serial #:	GH950-0832	Supplementary fan unit	N/A	Other:		www.nanotherics.com		
		IR Coil (external)	N/A	Live Cell	LC9009	Rat Coil	N/A			
Seq	Coil turns	Capacitor array Type/Value	Oscilloscope VOLTS/DIV setting, mV	Range Switch	Nominal frequency KHz	DC Power Supply Current	Max peak to peak voltage Vp-p (Volts actual V and Oscilloscope mV)	Coil ID, mm	mT (milli Tesla) at max Current	
1	9	200 nF	20	N/A	169.90	17.00	100 mV (2000 Vp-p)	44	23	
2	9	88 nF	20	N/A	254.90	17.40	100 mV (2000 Vp-p)	44	23	
3	9	30 nF	50	N/A	430.40	16.00	150 mV (3000 Vp-p)	44	19	
4	9	15 nF	50	N/A	608.50	14.00	150 mV (3000 Vp-p)	44	15	
5	9	6.2 nF	50	N/A	986.90	12.50	250 mV (5000 Vp-p)	44	12	
6	18	200 nF	20	N/A	103.50	16.00	100 mV (2000 Vp-p)	44	30	
7	18	88 nF	20	N/A	155.30	11.50	100 mV (2000 Vp-p)	44	22	
8	18	30 nF	20	N/A	262.70	10.60	150 mV (3000 Vp-p)	44	19	
9	18	15 nF	20	N/A	371.60	9.65	150 mV (3000 Vp-p)	44	16	
10	18	6.2 nF	20	N/A	601.60	9.25	250 mV (5000 Vp-p)	44	12	
11	Live Cell	200 nF	10	N/A	210.80	13.75	100 mV (2000 Vp-p)	10	30	
12	Live Cell	88 nF	20	N/A	315.70	12.00	100 mV (2000 Vp-p)	10	25	
13	Live Cell	30 nF	50	N/A	534.10	10.75	150 mV (3000 Vp-p)	10	20	
14	Live Cell	15 nF	50	N/A	754.60	9.75	150 mV (3000 Vp-p)	10	16	
15	Live Cell	6.2 nF	N/A	N/A	N/A	N/A	N/A	N/A	N/A	

Appendix II: Planar Coil

According to theoretical expectations, thicker specimens should generate more heat when exposed to a uniform alternating magnetic field due to greater volume [19]. However, since non-uniformity of the magnetic field was expected, a worry about non-uniform heating arose. The hypothesis was that the nonuniform field heats only the bottom part of the specimen, while the upper part, subjected (absorbing a weaker magnetic field), acts as a heat sink.

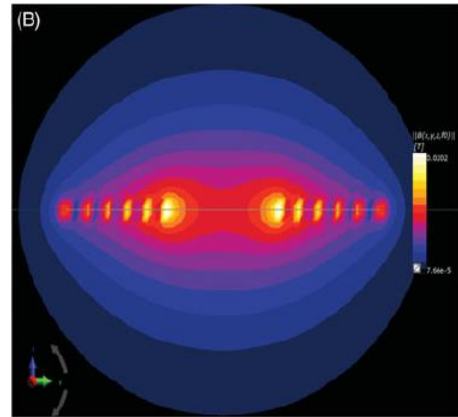


Figure 2.2 Magnetic flux density simulation of the Nanotherics 8-turn planar coil [53]

Materials and Methods

To prove this hypothesis, a dedicated validation experiment assessed whether the planar coil could reliably meet the study's requirements for generating a magnetic field with enough uniformity. The thickness of the specimens was systematically varied, while all the other parameters, such as exposure time, placement, field frequency, and field amplitude, were kept consistent. The specimens were exposed to a 756 kHz AMF with a field amplitude of 5.0 mT for one minute. The different thicknesses that were tested were 0.5 and 1.5 mm . In addition, a non-conductive spacer was used to create the same thickness without the influence of additional material heating up. Figure 2.3 shows the specimens respectively. The hypothesis is rejected when the situation with the spacer can generate the same amount of heat as the situation with only the thin metallic disk because slight variations in the Z-direction would not matter. However, if the hypothesis of this experiment were confirmed with this experiment, the planar coil attachment would not suffice for Analytical Modeling since thicker specimens will be used to validate the model.

An experiment with samples of varying heights was conducted to assess the uniformity of the magnetic field (in the z-direction) generated by the planar coil. Cylindrical samples with dimensions of 8.0 mm in diameter and different heights (0.5 and 1.5 mm) were tested in the planar coil setup with a thermal camera (Figure 2.3). To assess the uniformity of the magnetic field in the z-direction, the 0.5 mm high sample was additionally tested with an insulating 1.0 mm rubber spacer to prevent overheating of the plastic dish. All samples were tested in the center of a Petri dish, where they were placed on top of a rubber mat with a thickness of 1.5 mm . The specimens were exposed to a 756 kHz AMF with a field amplitude of 5.0 mT for one minute. Thermal camera PI450i (Optris, Germany) was used for live imaging. It was mounted on an extended tripod, which ensured a constant distance of 50 mm between the camera's lens and the specimen. Additionally, a cap was placed over the lens, preventing the camera from picking up emissivity noise from the surroundings.



Figure II.2 Real-life experimental setup

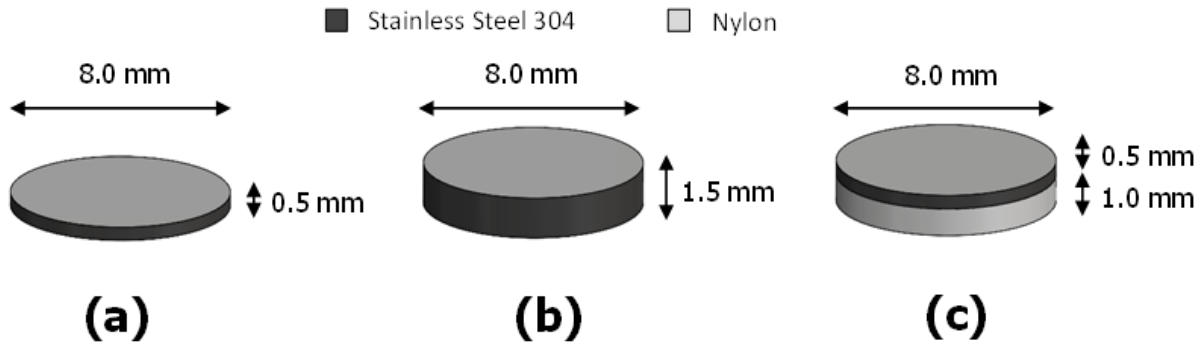


Figure II.1 Schematical representation of the specimen setup: (a) thin single metallic disk, (b) thick single metallic disk, (c) thin metallic disk with non-conductive spacer

The specimens were placed in the center of a Petri dish that fitted in the external coil option of the MagneTherm by Nanotherics (United Kingdom) equipped with the live-cell option, which features a three copper wire core eight-turn planar coil. Since high temperatures could be reached, an insulating 1.5 mm rubber mat was placed in the Petri dish to prevent the Petri dish from melting. Above the specimen is the PI450i thermal camera by Optris (Germany), mounted on an extended tripod. The camera was mounted so that the distance between the lens of the camera and the specimen would be 50 mm. This ensured the magnetic field would not disturb the functionality of the thermal camera. The distance was ensured by placing a cap over the lens, which prevented the camera from picking up emissivity noise for more reliable measurements.

Results

The results from the measurement with the planar coil are depicted below. Figure 3.1 illustrates the average temperature within the region enclosed by the white circle, which is visually aligned to match the contour of the specimen. Three scenarios are presented: heating of a 0.5 mm Stainless steel disk, heating of a 1.5 mm Stainless steel disk, and heating of a 0.5 mm Stainless steel disk with a 1.0 mm nylon spacer placed between. It is evident that the 0.5 mm disk exhibits the highest average temperature, followed by the 0.5 mm Stainless steel disk with the spacer, and finally, the 1.5 mm Stainless steel disk displays the lowest average temperature.

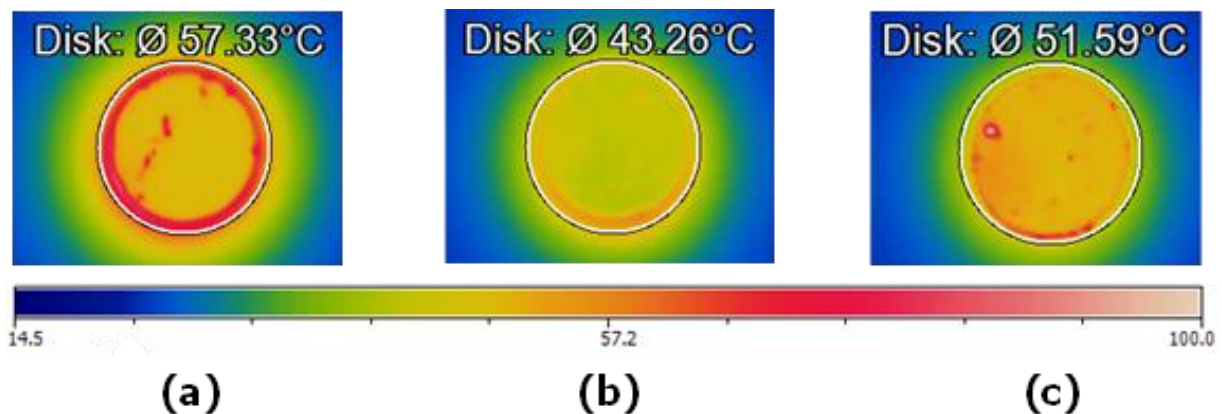


Figure II.3 Planar coil non-uniform magnetic field test: (a) 0.5 mm Stainless steel disk, (b) 1.5 mm disk Stainless steel disk, (c) 1mm nylon (spacer) disk + 0.5 mm Stainless steel disk

Discussion

The experimental results examining the heating behavior of Stainless steel disks under the influence of a planar coil attachment provide valuable insights into the intricacies of magnetic field uniformity and its impact on heat generation within a specimen. The 0.5 mm Stainless steel disk with a spacer exhibited significantly less heating than the 0.5 mm disk alone. Moreover, thicker disks would be anticipated to generate more heat due to their increased material volume under a uniform magnetic field. The experimental findings indicate, however, that the distribution of heat within the specimen is influenced by the non-uniform magnetic field generated by the planar coil. This validation experiment demonstrates that subtle variations in magnetic field uniformity can have pronounced effects on heat generation and distribution.

The experimental results confirmed the hypothesis: proposing that only the bottom part of the specimen is significantly heated while the upper part acts as a heatsink. In light of those findings, it was decided to discontinue the external planar coil attachment in favor of a solenoid coil configuration. The solenoid coil offers a more favorable magnetic field uniformity profile, which can be better represented through the analytical model.

Appendix III: Safety Protocol

PROTOCOL CODE: 231127 SAFETY CATEGORY: 2

Name author: Tijmen Hartsuijker
Name supervisor: Monika Šalandová / Iulian
Name approver: Apachitei
Date approved: Sander Leeflang
27 11 2023

Signature approver:



Title:

Testing the influence of magnetic hyperthermia on different biomaterials

Introduction:

In this experimental procedure, metallic specimens are subjected to heating using the MagneTherm apparatus with the aim of determining the most effective operational parameters for each material in the context of magnetic hyperthermia. The ultimate goal is to mitigate the thermal effects induced by orthopedic implants instead of magnetic nanoparticles. The metallic specimens are prepared and subsequently positioned within the MagneTherm apparatus to undergo magnetic hyperthermia treatment. Throughout this treatment process, the temperature is systematically monitored through the utilization of an infrared camera and/or temperature probe(s). Multiple configurations and settings will be systematically explored to ascertain the optimal magnetic field parameters specific to each material, thereby minimizing the resultant temperature.

1. Requirements

1.1. Substances

- **Isopropanol (C₃H₈O)**

Supplier:	T.B.D.
Product code:	T.B.D.
Phase:	Liquid
Storage location:	34.J-0-440B (Bio Functionalisation lab) cabinet C3
CAS no.	67-63-0
Hazard statements:	H225 - Highly flammable liquid and vapor. H319 - Causes serious eye irritation. H336 - May cause drowsiness or dizziness.

- **Ti grade 2 (cpTi)**
 - Supplier: Salamon's Metalen B.V.
 - Product code: Titaan Naadloze buis "Grade 2"
 - Phase: Solid
 - Storage location: 34.F-0-221 (Bio Characterisation Laboratory) cabinet
 - CAS no. 7440-32-6
 - Hazard statements: **H228** - Flammable solid.
H251 - Self-heating: may catch fire.

- **Ti grade 5 ((Ti6Al4V) (3D-printed))**
 - Supplier: AP&C
 - Product code: N/A
 - Phase: Solid (fused powder)
 - Storage location: 34.F-0-221 (Bio Characterisation Laboratory) cabinet
 - CAS no. 99906-66-8
 - Hazard statements: N/A.

- **Stainless steel 316L (FeCr18Ni10Mo3)**
 - Supplier: Salamon's Metalen B.V.
 - Product code: 316(L) naadloos buis / capilair
 - Phase: Solid
 - Storage location: 34.F-0-221 (Bio Characterisation Laboratory) cabinet
 - CAS no. 65997-19-5
 - Hazard statements: **H332** - Harmful if inhaled.
H317 - This may cause an allergic skin reaction.
H350 - May cause cancer.
H372 - Causes damage to organs through prolonged or repeated exposure.
H412 - Harmful to aquatic life with long-lasting effects

- **Copper**
 - Supplier: Salamon's Metalen B.V.
 - Product code: DIN: SFCu - ECu57 industriepijp
 - Phase: Solid
 - Storage location: 34.F-0-221 (Bio Characterisation Laboratory) cabinet
 - CAS no. 7440-50-8
 - Hazard statements: **H411** - Toxic to aquatic life with long lasting effects

All the solid materials are biomaterials and are suitable to be placed within the human body in stable conditions.

1.2. Equipment

- MagneTherm from Nanotherics + accessories
- Infrared camera + accessories
- Laptop/computer
- Sonicate machine
- Wire cutters
- Tweezers
- Air extraction tube/fume hood

1.3. Labware

- Eppendorf tubes
- beakers
- Petri dishes
- Pipet

1.4. Personal protection equipment

- Lab coat
- Disposable gloves, Nitrile
- Safety glasses

1.2. Equipment

- MagneTherm from Nanotherics + accessories
- Infrared camera + accessories
- Laptop/computer
- Sonicate machine
- Wire cutters
- Tweezers
- Air extraction tube/fume hood

2. Procedure

2.1 Preparing the samples

The samples undergo preparation within the Bio-Functionalization laboratory. Adherence to safety protocols is imperative within this laboratory setting, necessitating the use of a lab coat at all times while working in this area. Additionally, the mandatory utilization of disposable gloves is enforced when handling substances. Given the use of wire cutters, the mandatory use of eye protection or safety goggles is enforced during the manipulation of specimen materials. These materials are systematically reduced to the required size using wire cutters and subsequently stored in hermetically sealed zip-bags.

Following the cutting process, each specimen undergoes individual rinsing within beakers containing isopropanol alcohol. During this rinsing step, the use of eye protection is once again obligatory, and caution must be exercised to avoid proximity to open flames and other potential heat sources, while also refraining from inhaling isopropanol fumes. It is recommended to carry out this process in a well-ventilated area.

Subsequent to the isopropanol alcohol rinse, the specimens are subjected to a 5-minute sonication process within the same isopropanol alcohol-filled beaker. Following sonication, the used isopropanol is appropriately disposed of in the designated "waste without halogens" container. The specimens are then rinsed in a beaker containing demi water and subjected to an additional 5-minute sonication. The contaminated demi water resulting from this step is also disposed of in the "waste without halogens" container.

Upon completion of the cleaning procedures, the specimens are left to air dry on a paper towel. Ensure to affix a warning note prominently as the specimens undergo the air-drying process, alerting other laboratory users to potential risks.

2.2 Performing the experiment

When operating the MagneTherm, familiarize yourself with the instruction manual prior to usage, and take heed of the subsequent warnings:

Do not operate this equipment or approach within two meters if you are wearing a heart pacemaker or other implanted bio-medical device with high voltage!

The unit contains hazardous and potentially lethal voltages. There is an interlock system that prevents the unit from operating unless the Front panel and Lid are in place. **Do not** attempt to bypass this interlock or operate the unit without the front panel and lid fixed in position.

Do not heat samples in closed containers as they may rupture due to steam or gas build-up

Do not place metallic objects in the sample aperture of the magneTherm. Be especially careful not to bring rings, bracelets, watches, etc. close to the aperture or near any external coils—metal will heat VERY rapidly!

Do not switch off the power at the end of your experiment without first returning the DC Power Supply voltage setting to zero.

Protocol: [MagneTherm Coil Setup and Operation in the Bio Characterisation Laboratory](#)

Objective:

Ensure safe and controlled operation of the MagneTherm with specific attention to the coil setup in the Bio Characterisation Laboratory.

Coil Setup Options:

The MagneTherm provides three coil setup options: two internal and one external. To mitigate risks and prevent hazards, the following protocol is established.

Safety Precautions:

- a. Warning Sign Placement: Affix a warning sign on the door of the Bio Characterisation Laboratory to alert individuals about the generated magnetic field.
- b. Machine Activation: Turn on the MagneTherm following the labelled order on the equipment itself.
- c. Ensure at least one experienced person with knowledge of MagneTherm operations is present in the room during machine activation.
- d. Magnetic Field Generation: Once activated, a magnetic field is generated around the coil.

Machine Tuning:

- a. Always tune the machine before use.
- b. Double-check that both the capacitor set and coil match with the settings in the software.

Specimen Placement:

- a. For the internal coil option, place specimens in Eppendorf tubes.
- b. For the external coil option, use a petri dish.
- c. Containers must not be completely sealed to prevent explosion hazards.

Safety Gear:

- a. Wear a lab coat and disposable gloves during testing.
- b. For experiments involving CoCr alloys and Tantalum specimens, safety glasses are mandatory.

Temperature Monitoring:

- a. Heat generated during testing can be observed using heat probes or a thermal camera.
- b. If temperatures exceed 200 °C, turn off the device by clicking the stop button in the software.
- c. Expected maximum temperatures are around 120 °C; all specimens are stable within this limit.

Fume Extraction:

For testing with stainless steel, CoCr alloys, and Tantalum, place an air extraction tube over the test setup to extract potential fumes.

Safety Signage:

Hang a safety sign on the door when the MagneTherm is in operation (available in the protocol folder).

By strictly adhering to this protocol, the safe utilization of the MagneTherm in the Bio Characterisation Laboratory is ensured, minimizing potential risks and promoting a secure laboratory environment.

It is crucial to underscore the following guidelines for handling materials outlined in this protocol:

- Refrain from inhaling or ingesting any substances listed in the materials.
- Avoid exposing materials to open flames under any circumstances.
- Extract the fumes, particularly when working with CoCr, Stainless Steel, and Tantalum.
- Wear the designated Personal Protective Equipment (PPE) for enhanced safety.

3. *Disposal*

- Organic solvents (isopropanol) used for cleaning should be disposed of in the organic waste without halogens container.
- All chromium-containing waste must go into the acidic and neutral inorganic waste.

4. *Transportation*

Specimens should be transported in sealed zip bags at all times.

5. *Safety Category*

This experiment protocol involves materials with certain health hazards and involves high current devices as well as a generated high frequency (low amplitude) alternating magnetic field. I would categorize this experiment as Category 2.

	CATEGORY 1 <i>zero risk</i>	CATEGORY 2 <i>low risk</i>	CATEGORY 3 <i>high risk</i>
OFFICE HOURS <i>8:00 - 17:00</i>	Working alone permitted	Working alone permitted	Only permitted with a second qualified person present
OUTSIDE OFFICE HOURS <i>17:00 - 8:00 and weekends</i>	Working alone permitted	Only permitted with a second qualified person present	not permitted

Material Safety Data Sheets

Compact Safety Data Sheets (SDS) for each material referenced in this protocol are available in the appendix. For comprehensive information, including supplier data sheets and complete material safety data sheets, refer to the same folder as this protocol.

DISPOSAL CATEGORIES FOR LIQUID LABORATORY WASTE

ACIDIC AND NEUTRAL INORGANIC WASTE

- Inorganic acids
e.g.: hydrochloric acid, phosphoric acid, nitric acid,
- Metallic ions in aqueous solution
e.g.: zinc, copper, lead, nickel

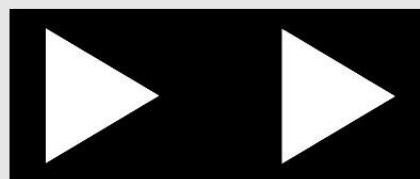
CATEGORY I



ALKALINE INORGANIC WASTE

- Inorganic hydroxides
e.g.: potassium hydroxide, sodium hydroxide
- Ammonia solution
- Sodium hypochlorite

CATEGORY II



ORGANIC WASTE WITHOUT HALOGENS

- Solvents without halogens
e.g.: acetone, ethanol
- Organic acids and bases
e.g.: acetic acid, methyl amine

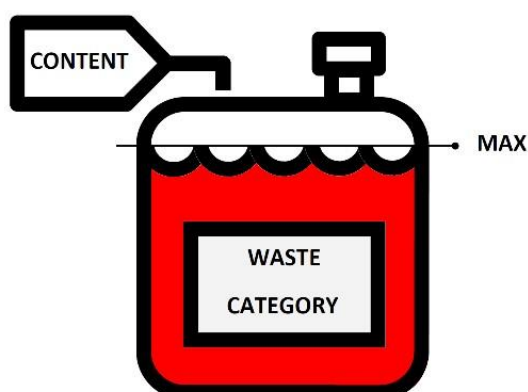
CATEGORY III



ORGANIC WASTE WITH HALOGENS

- Solvents with halogens
(contains: fluorine, chlorine, bromine, iodine)
e.g.: chloroform, dichloromethane

CATEGORY IV



- Write the chemical name of your waste on the cardboard tag
- Do not overfill the waste container (max 80%)
- When full, replace the container. Make sure it has the correct waste category label. Place the funnel on the empty container and the cap on the full one; don't close it completely so that gas could escape. Send email to m.a.leeflang@tudelft.nl with header "waste container full".

MINI SDS

Considered a hazardous mixture according to Reg. (EC) No 1272/2008 and their amendments. Not classified as Dangerous Goods for transport purposes.

316L Stainless Steel

INGREDIENTS	CAS NO	%	8HR OEL
chromium	7440-47-3	10-30	0.5 mg/m3
iron	7439-89-6	>60	-
nickel	7440-02-0	10-30	-
molybdenum	7439-98-7	1-10	-



GHS

DG

UN No: **Not Applicable**DG Class: **Not****Applicable**Subsidiary Risk: **Not****Applicable**Packing Group: **Not****Applicable****HEALTH HAZARD INFORMATION****Signal word:** **Danger****Hazard statement(s):****H317** May cause an allergic skin reaction.**H351** Suspected of causing cancer.**H372** Causes damage to organs through prolonged or repeated exposure.**H412** Harmful to aquatic life with long lasting effects.**PRECAUTIONS FOR USE****Glasses:**

Consider chemical goggles.

Gloves: Leather Gloves.**Respirator:**

Type -P Filter of sufficient capacity. (AS/NZS 1716 & 1715, EN 143:2000 & 149:2001, ANSI Z88 or national equivalent)

Storage and Transportation:

Store in cool, dry, protected area. Keep locked up. Keep out of reach of children. Keep away from living quarters.

Fire/Explosion Hazard:

Toxic smoke/fumes in a fire. In case of fire and/or explosion, DO NOT BREATHE FUMES.

PROPERTIES

Solid.

EMERGENCY**FIRST AID****Swallowed:**

Give water (if conscious). Seek medical advice.

Skin:

Remove contaminated clothing. Wash with soap & water.

Inhaled:

Fresh air. Rest, keep warm. If breathing shallow, give oxygen. Medical attention.

Advice To Doctor:

Treat symptomatically. Supportive care. "metal fume fever". Remove from exposure. Treatment is supportive.

Fire Fighting:

Dry agent. Do NOT fight fire with BCF extinguisher. Do NOT fight fire with water.

Spills and Disposal:

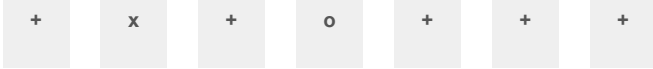
Avoid dust. Sweep shovel to safe place. This material and its container must be disposed of in a safe way. To clean the floor and all objects contaminated by this material, use water and detergent.

Chemwatch:

Print Date:

Issue Date:

SAFE STORAGE WITH OTHER CLASSIFIED CHEMICALS



x — Must not be stored together

0 — May be stored together with specific precautions

+ — May be stored together

Note: Depending on other risk factors, compatibility assessment based on the table above may not be relevant to storage situations, particularly where large volumes of dangerous goods are stored and handled. Reference should be made to the Safety Data Sheets for each substance or article and risks assessed accordingly.

PRECAUTIONS FOR USE



Glasses:	Consider chemical goggles.
Respirator:	Type -P Filter of sufficient capacity. (AS/NZS 1716 & 1715, EN 143:2000 & 149:2001, ANSI Z88 or national equivalent)
Storage and Transportation:	Store in cool, dry, protected area. Keep out of reach of children.
Fire/Explosion Hazard:	Toxic smoke/fumes in a fire.
Environment:	Harmful to aquatic organisms.

PROPERTIES



Solid. Does not mix with water.

EMERGENCY



FIRST AID

66-56739
17/11/2023
23/12/2022

GHS

DG

Chemwatch: 11-91313

2

MINI SDS

Considered a hazardous substance according to Reg. (EC) No 1272/2008 and its amendments. Not classified as Dangerous Goods for transport purposes.

COBALT-CHROMIUM ALLOY

INGREDIENTS

INGREDIENTS	CAS NO	%	8HR OEL
cobalt-chromium alloy	11114-92-4	>98	0,005 mg/m3



UN No: **Not Applicable**
DG Class: **Not Applicable**
Subsidiary Risk: **Not Applicable**
Packing Group: **Not Applicable**

HEALTH HAZARD INFORMATION



Signal word: **Danger**

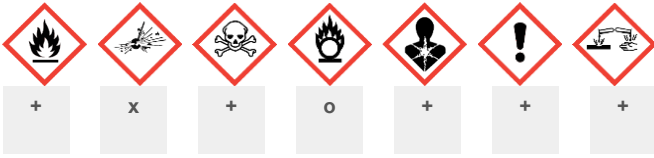
Hazard statement(s):

H317 May cause an allergic skin reaction.
May cause allergy or asthma symptoms or
H334 breathing difficulties if inhaled.
H351 Suspected of causing cancer.

Swallowed:	Give water (if conscious). Seek medical advice.
Eye:	Wash with running water.
Skin:	Remove contaminated clothing. Wash with soap & water.
Inhaled:	Fresh air. Rest, keep warm. If breathing shallow, give oxygen. Medical attention.
Advice To Doctor:	Supportive care. "metal fume fever". Remove from exposure. Treatment is supportive.
Fire Fighting:	Dry agent. Do NOT fight fire with BCF extinguisher. Do NOT fight fire with water.
Spills and Disposal:	Avoid dust. Sweep shovel to safe place. This material and its container must be disposed of in a safe way. To clean the floor and all objects contaminated by this material, use water and detergent.

Chemwatch:
Print Date:
Issue Date:

SAFE STORAGE WITH OTHER CLASSIFIED CHEMICALS



x — Must not be stored together

O — May be stored together with specific precautions

+ — May be stored together

Note: Depending on other risk factors, compatibility assessment based on the table above may not be relevant to storage situations, particularly where large volumes of dangerous goods are stored and handled. Reference should be made to the Safety Data Sheets for each substance or article and risks assessed accordingly.

PRECAUTIONS FOR USE


Appropriate engineering controls:

General Exhaust Ventilation adequate.

Glasses:

Consider chemical goggles.

Respirator:

Type -P Filter of sufficient capacity. (AS/NZS 1716 & 1715, EN 143:2000 & 149:2001, ANSI Z88 or national equivalent)

Storage and Transportation:

Store in cool, dry, protected area.

Fire/Explosion Hazard:

Toxic smoke/fumes in a fire.

PROPERTIES



Solid. Mixes with water. Combustible.

EMERGENCY



FIRST AID

11-91313
17/11/2023
02/06/2023

GHS

DG

Chemwatch: 13583

Not considered a hazardous substance according to Reg. (EC) No 1272/2008 and its amendments. Not classified as Dangerous Goods for transport purposes.

GELATINE

INGREDIENTS	CAS NO	%	8HR OEL
-------------	--------	---	---------

gelatine	9000-70-8	100	-
----------	-----------	-----	---

UN No: **Not Applicable**

DG Class: **Not**

Applicable

Not Applicable Subsidiary Risk: **Not**

Applicable

Packing Group: **Not**

Applicable

HEALTH HAZARD INFORMATION

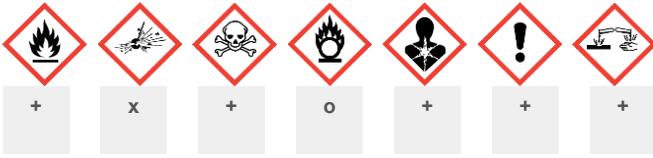
Signal word:

Hazard statement(s): Not Available

Swallowed:	Rinse mouth with water.
Eye:	Wash with running water. For discomfort seek medical advice.
Skin:	Remove contaminated clothing. Wash with soap & water.
Inhaled:	Fresh air. Rest, keep warm.
Advice To Doctor:	Treat symptomatically.
Fire Fighting:	Water spray/ fog.
Spills and Disposal:	Eliminate ignition sources. Avoid dust. Sweep shovel to safe place.

Chemwatch:
Print Date:
Issue Date:

SAFE STORAGE WITH OTHER CLASSIFIED CHEMICALS



x — Must not be stored together

o — May be stored together with specific precautions

+ — May be stored together

Note: Depending on other risk factors, compatibility assessment based on the table above may not be relevant to storage situations, particularly where large volumes of dangerous goods are stored and handled. Reference should be made to the Safety Data Sheets for each substance or article and risks assessed accordingly.

PRECAUTIONS FOR USE



Glasses: Consider chemical goggles.

Respirator: Type -P Filter of sufficient capacity. (AS/NZS 1716 & 1715, EN 143:2000 & 149:2001, ANSI Z88 or national equivalent)

Storage and Transportation: Store in cool, dry, protected area. Keep out of reach of children.

Fire/Explosion Hazard: Toxic smoke/fumes in a fire.

PROPERTIES



Solid. Does not mix with water. Sinks in water.

EMERGENCY



FIRST AID

13583
17/11/2023
20/06/2022

GHS

DG

Chemwatch: 35478

2

MINI SDS

Not considered a hazardous substance according to Reg. (EC) No 1272/2008 and its amendments. Not classified as Dangerous Goods for transport purposes.




IRON

INGREDIENTS	CAS NO	%	8HR OEL
iron, powder	7439-89-6	>99	-
UN No: Not Applicable DG Class: Not Applicable Not ApplicableSubsidiary Risk: Not Applicable Packing Group: Not Applicable	Swallowed:	Rinse mouth with water.	
	Eye:	Wash with running water.	
	Skin:	Wash with soap	
	Inhaled:	Fresh air. Rest, keep warm. If breathing shallow, give oxygen. Medical attention.	
	Advice To Doctor:	Treat symptoms NOT history. Emesis. Deferoxamine may be antidotal. Supportive care. "metal fume fever". Remove from exposure. Treatment is supportive.	
HEALTH HAZARD INFORMATION			
Signal word:			
Hazard statement(s):	Not Available		

Chemwatch:
Print Date:
Issue Date:

Fire Fighting:	Dry agent. Do NOT fight fire with BCF extinguisher. Do NOT fight fire with water.
Spills and Disposal:	Avoid dust. Sweep shovel to safe place. This material and its container must be disposed of in a safe way.

SAFE STORAGE WITH OTHER CLASSIFIED CHEMICALS

						
+	+	+	+	+	+	+

X — Must not be stored together

0 — May be stored together with specific preventions

+ — May be stored together

Note: Depending on other risk factors, compatibility assessment based on the table above may not be relevant to storage situations, particularly where large volumes of dangerous goods are stored and handled. Reference should be made to the Safety Data Sheets for each substance or article and risks assessed accordingly.




35478
17/11/2023
23/12/2022

Chemwatch:
Print Date:
Issue Date:

Chemwatch: 1219

ISOPROPANOL

INGREDIENTS	CAS NO	%	8HR OEL
isopropanol	67-63-0	>99	-


GHS	DG	PROPERTIES
	 <p>UN No: 1219 DG Class: 3 Subsidiary Risk: Not Applicable Packing Group: II</p>	 <p>Liquid. Mixes with water. Highly flammable. May</p>

form explosive peroxides.

EMERGENCY

HEALTH HAZARD INFORMATION	FIRST AID
 <p>Signal word: Danger</p> <p>Hazard statement(s): H225 Highly flammable liquid and vapour. H319 Causes serious eye irritation. H336 May cause drowsiness or dizziness.</p>	 <p>Swallowed: Give water (if conscious). Seek medical advice. Eye: Wash with running water. Skin: Wash with soap Inhaled: Fresh air. Rest, keep warm. If breath shallow, give oxygen. Medical attention. Advice To Doctor: Severe exposure indicated by respiratory distress/hypotension. Management is essentially supportive. Fire Fighting: Keep containers cool. Water spray/ fog. Foam - alcohol type. Spills and Disposal: Eliminate ignition sources. Consider evacuation. Prevent from entering drains. Contain spillage by any means. Control vapour with water spray/ fog. Absorb with dry agent. Stop leak if safe to do so. This material and its container must be disposed of in a safe way. To clean the floor and all objects contaminated by this material, use water.</p>

PRECAUTIONS FOR USE

	<p>Appropriate engineering controls: Local Exhaust Ventilation recommended.</p> <p>Glasses: Consider chemical goggles.</p> <p>Gloves: 1.NITRILE+PVC 2.PE/EVAL/PE</p> <p>Respirator: Type A Filter of sufficient capacity. (AS/NZS 1716 & 1715, EN 143:2000 & 149:2001, ANSI Z88 or national equivalent)</p> <p>Storage and Transportation: Store in cool, dry, protected area. Restrictions on Storage apply. Refer to Full Report. Keep out of reach of children. Keep container in a well ventilated place. Keep away from sources of ignition. No smoking. Handle and open container with care.</p> <p>Fire/Explosion Hazard: HIGHLY FLAMMABLE. Vapours/gas heavier than air. Toxic smoke/fumes in a fire. In case of fire and/or explosion, DO NOT BREATHE FUMES.</p>
------------------------------------------------------------------------------------	-----------------------------------------------------------------------------------------------------------------------------------------------------------------------------------------------------------------------------------------------------------------------------------------------------------------------------------------------------------------------------------------------------------------------------------------------------------------------------------------------------------------------------------------------------------------------------------------------------------------------------------------------------------------------------------------------------------------------------------------------------------------------------------------------------------------------------

SAFE STORAGE WITH OTHER CLASSIFIED CHEMICALS

+	x	+	x	+	+	+	x
							
Must not be stored together							

0 — May be stored together with specific precautions

+ — May be stored together

Note: Depending on other risk factors, compatibility assessment based on the table above may not be relevant to storage situations, particularly where large volumes of dangerous goods are stored and handled. Reference should be made to the Safety Data Sheets for each substance or article and risks assessed accordingly.

Chemwatch:
Print Date:
Issue Date:

Chemwatch: 65527

Not considered a hazardous substance according to Reg. (EC) No 1272/2008 and its amendments. Not classified as Dangerous Goods for transport purposes.

PEEK

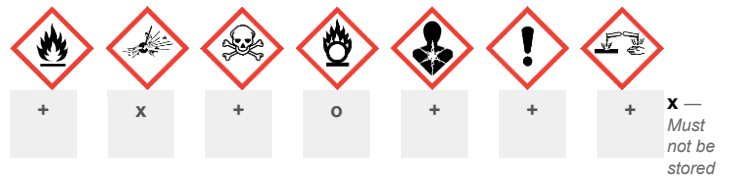
INGREDIENTS	CAS NO	%	8HR OEL
PEEK	29658-26-2	>98	-

PROPERTIES

Solid. Does not mix with water. Sinks in water. Combustible.

EMERGENCY**FIRST AID**

Swallowed:	Rinse mouth with water.
Eye:	Wash with running water. For discomfort seek medical advice.
Skin:	Wash with soap For burns: Apply cold water. Do NOT remove clothes from area. Cover wound. NO OINTMENTS.
Inhaled:	Blow nose. Rinse mouth with water.
Advice To Doctor:	Treat symptomatically.
Fire Fighting:	Foam.
Spills and Disposal:	Eliminate ignition sources. Avoid dust. Sweep shovel to safe place.

SAFE STORAGE WITH OTHER CLASSIFIED CHEMICALS

together

0 — May be stored together with specific preventions**+** — May be stored together

Note: Depending on other risk factors, compatibility assessment based on the table above may not be relevant to storage situations, particularly where large volumes of dangerous goods are stored and handled. Reference should be made to the Safety Data Sheets for each substance or article and risks assessed accordingly.

GHS **DG**

UN No: **Not Applicable**
 DG Class: **Not Applicable**
 Subsidiary Risk: **Not Applicable**
 Packing Group: **Not Applicable**

HEALTH HAZARD INFORMATION

Signal word:

Hazard statement(s): Not Available

PRECAUTIONS FOR USE

Appropriate engineering controls: General Exhaust Ventilation adequate.

Glasses: Consider chemical goggles.

Respirator: Type A-P Filter of sufficient capacity. (AS/NZS 1716 & 1715, EN 143:2000 & 149:2001, ANSI Z88 or national equivalent)

Storage and Transportation: Store in cool, dry, protected area.

Fire/Explosion Hazard: Toxic smoke/fumes in a fire.

Chemwatch:
Print Date:
Issue Date:

65527
17/11/2023

10/10/2019

Chemwatch: 32353

TANTALUM



UN No: 3089

HEALTH HAZARD INFORMATION



INGREDIENTS	CAS NO	%	8HR OEL
-------------	--------	---	---------

tantalum	7440-25-7	>98	-
----------	-----------	-----	---

GHS	DG	PROPERTIES
-----	----	------------

DG Class: 4.1
Subsidiary Risk: Not

Applicable Solid. Does not mix with water. Sinks in water. Highly flammable. Packing Group: II

EMERGENCY



FIRST AID

Signal word: **Danger**

Hazard statement(s):	Description
H228	Flammable solid.
H315	Causes skin irritation.
H319	Causes serious eye irritation.
H335	May cause respiratory irritation.

Chemwatch:
Print Date:
Issue Date:

PRECAUTIONS FOR USE



Glasses:	Consider chemical goggles.
Respirator:	Type -P Filter of sufficient capacity. (AS/NZS 1716 & 1715, EN 143:2000 & 149:2001, ANSI Z88 or national equivalent)
Storage and Transportation:	Store in cool, dry, protected area. Keep out of reach of children. Keep container tightly closed. Keep container dry.
Fire/Explosion Hazard:	HIGHLY FLAMMABLE. Toxic smoke/fumes in a fire. In case of fire and/or explosion, DO NOT BREATHE FUMES.

SAFE	+	x	+	x	+	+	+

Swallowed:	Rinse mouth with water.
Eye:	Wash with running water.
Skin:	Remove contaminated clothing. Wash with soap & water.
Inhaled:	Fresh air. Rest, keep warm. If breath shallow, give oxygen. Medical attention.
Advice To Doctor:	Supportive care. "metal fume fever". Remove from exposure. Treatment is supportive.
Fire Fighting:	Foam. Dry agent. Do NOT fight fire with BCF extinguisher. Do NOT fight fire with water.
Spills and Disposal:	Eliminate ignition sources. Avoid dust. Prevent from entering drains. Contain spillage by any means. Sweep shovel to safe place. Never spray with water. This material and its container must be disposed of in a safe way. To clean the floor and all objects contaminated by this material, use water and detergent.

STORAGE WITH OTHER CLASSIFIED CHEMICALS

0 — May be stored together with specific preventions

x — Must not be stored together

+ — May be stored together

Note: Depending on other risk factors, compatibility assessment based on the table above may not be relevant to storage situations, particularly where large volumes of dangerous goods are stored and handled. Reference should be made to the Safety Data Sheets for each substance or article and risks assessed accordingly.

32353
17/11/2023
20/06/2022

Chemwatch:
Print Date:
Issue Date:

WERKPLEKINSTRUCTIEKAART (MINI SDS)

Niet beschouwd als een gevaarlijke stof volgens Reg. (EG) nr. 1272/2008 en de bijbehorende amendementen. Niet geclassificeerd als gevaarlijke goederen voor transportdoeleinden.

TITANIUM VANADIUM METAL ALLOYS

INGREDIËNTEN	CAS NR	%	8HR OEL
titanium vanadium metal alloys	Niet Beschikbaar	>98	-

GHS	DG
	UN-Nr.: Niet van Toepassing

Toepassing Transportklasse: Niet van Toepassing

Niet van Toepassing

Secundair Risico: Niet van Toepassing Verpakkingsgroep: Niet van Toepassing

INFORMATIE MBT GEZONDHEIDSRISICO'S

Signaalwoord:

Gevarenaanduiding: Niet Beschikbaar

Voorzorgsmaatregelen voor het gebruik



Bril:	Chemische veiligheidsbril.
Handschoenen:	Leren handschoenen.
Ademhalingsstoestel:	Particulate Filter met voldoende capaciteit. (AS / NZS 1716 & 1715, EN 143:2000 en 149:001, ANSI Z88 of nationaal equivalent)
Opslag en transport:	Sla op koele, droge, beschermde plaats op. Buiten bereik van kinderen bewaren.
BRAND-/ONTPLOFFINGSGEVAAR:	Giftige rook/dampen in een brand.
Milieu:	Schadelijk voor in het water levende organismen.

KENMERKEN



Vaste stof.

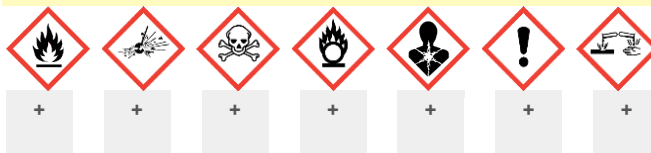
NOODSITUATIE



EHBO

INSLIKKEN:	Geef water (indien bij bewustzijn) Raadpleeg een arts.
Oog:	Was met stromend water.
Huid:	Was met water en zeep.
Inademen:	Frisse lucht. Rusten, warm houden. Indien oppervlakkige ademhaling, zuurstof toedienen. Medische zorg.
advies voor de arts:	Behandel de symptomen. Behandel de symptomen, NIET de geschiedenis. Laten braken. Deferoxamine is een mogelijk tegengif.
BRANDBESTRIJDING:	Bluspoeder. NIET blussen met een BCF (halon) brandblusser. NIET blussen met water.
Opruimen van gemorst materiaal:	Vermijd stof. Veeg/schuif naar een veilige plaats. Deze stof en de verpakking op veilige wijze afvoeren.

VEILIGE OPSLAG MET ANDERE GEKLASSEERDE CHEMICALIËN



x — Niet bij elkaar opslaan

— Kan bij elkaar opgeslagen worden na het treffen van specifieke

0

voorzorgsmaatregelen

+ — Kan bij elkaar opgeslagen worden

Opmerking: Afhankelijk van andere risicofactoren is het mogelijk dat compatibiliteitsbeoordeling op basis van bovenstaande tabel niet relevant is voor opslagsituaties, met name wanneer grote hoeveelheden gevaarlijke goederen worden opgeslagen en gehanteerd. Verwijs naar de veiligheidsinformatiebladen voor elke stof of elk voorwerp en beoordeel de risico's dienovereenkomstig.

TITANIUM



UN No: **2546**
 DG Class: **4.2**
 Subsidiary Risk: **Not Applicable**
 Packing Group: **II**



Signal word: **Danger**

Hazard statement(s):

H228 Flammable solid.

H251 Self-heating; may catch fire.

INGREDIENTS	CAS NO	%	8HR OEL
titanium	7440-32-6	>95	-

GHS	DG	PROPERTIES
-----	----	------------

Solid. Does not mix with water. Sinks in water. Highly flammable. Liable to spontaneous ignition. Spontaneously flammable in air.

HEALTH HAZARD INFORMATION

EMERGENCY

FIRST AID



PRECAUTIONS FOR USE

Swallowed:	Rinse mouth with water.
Eye:	Wash with running water (15 mins). Medical attention.
Skin:	Flood body with water. Remove contaminated clothing. Wash with water For burns: Apply cold water. Do NOT remove clothes from area. Cover wound. NO OINTMENTS.
Inhaled:	Fresh air. Rest, keep warm. If breathing shallow, give oxygen. Medical attention.
Advice To Doctor:	Treat symptomatically. Supportive care. "metal fume fever". Remove from exposure. Treatment is supportive.
Fire Fighting:	Foam. Dry agent. Do NOT fight fire with BCF extinguisher. Do NOT fight fire with water.
Spills and Disposal:	Eliminate ignition sources. Avoid dust. Prevent from entering drains. Contain spillage by any means. Sweep shovel to safe place. Never spray with water. This material and its container must be disposed of in a safe way. To clean the floor and all objects contaminated by this material, use water and detergent.

Glasses:	Consider chemical goggles.
Respirator:	Type -P Filter of sufficient capacity. (AS/NZS 1716 & 1715, EN 143:2000 & 149:2001, ANSI Z88 or national equivalent)
Storage and Transportation:	Store in cool, dry, protected area. Keep out of reach of children. Keep container tightly closed. Keep container dry.
Fire/Explosion Hazard:	HIGHLY FLAMMABLE. In case of fire and/or explosion, DO NOT BREATHE FUMES.

SAFE STORAGE WITH OTHER CLASSIFIED CHEMICALS

X	X	X	X	O	O	X

x — Must not be stored together

0 — May be stored together with specific preventions

+ — May be stored together

Note: Depending on other risk factors, compatibility assessment based on the table above may be relevant to storage situations, particularly where large volumes of dangerous goods are stored and handled. Reference should be made to the Safety Data Sheets for each substance or article and risks assessed accordingly.

Chemwatch: 2878-3
 Print Date: 17/11/2023
 Issue Date: 20/06/2022

This document is copyright. Apart from any fair dealing for the purposes of private study, research, review or criticism, as permitted under the Copyright Act, no part may be reproduced by any process without written permission from CHEMWATCH. TEL (+61 3) 9572 4700.

Chemwatch: 80-9381

Chemwatch Hazard Alert Code: 2

MINI SDS

Considered a hazardous mixture according to Reg. (EC) No 1272/2008 and their amendments. Not classified as Dangerous Goods for transport purposes.

AP&C Advanced Powders Spherical APA Ti-6Al-4V Powder (Coarse) Print

INGREDIENTS	CAS NO	%	8HR OEL
titanium	7440-32-6	>88.75	-
aluminium	7429-90-5	5.5-6.75	-
vanadium	7440-62-2	3.5-4.5	-

GHS

DG



UN No: **Not Applicable** DG Class: **Not Applicable**
 Subsidiary Hazard: **Not Applicable**
 Packing Group: **Not Applicable**



Signal word: **Warning**

Hazard statement(s): May cause damage to organs through H373 prolonged or repeated exposure.

PRECAUTIONS FOR USE



Glasses: Consider chemical goggles.

Gloves: Leather Gloves.

Respirator: Type -P Filter of sufficient capacity. (AS/NZS 1716 & 1715, EN 143:2000 & 149:2001, ANSI Z88 or national equivalent)

Storage and Transportation: Store in cool, dry, protected area. Dispose of this material and its container at hazardous or special waste collection point. Keep out of reach of children.

Fire/Explosion Hazard: Toxic smoke/fumes in a fire. Dispose of this material and its container at hazardous or special waste collection point.

PROPERTIES



Solid.

EMERGENCY



FIRST AID

Swallowed: Give water (if conscious). Seek medical advice.

Eye: Wash with running water.

Skin: Wash with soap For burns: Apply cold water. Do NOT remove clothes from area. Cover wound. NO OINTMENTS.

Inhaled: Fresh air. Rest, keep warm. If breathing shallow, give oxygen. Medical attention.

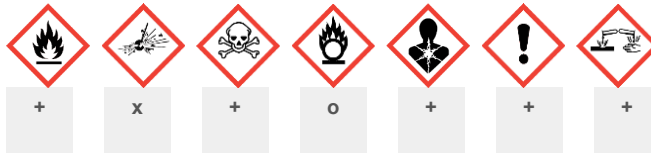
Advice To Doctor: Treat symptomatically. Supportive care. "metal fume fever". Remove from exposure. Treatment is supportive.

Fire Fighting: Dry agent. Do NOT fight fire with BCF extinguisher. Do NOT fight fire with water.

Spills and Disposal:

Avoid dust. Sweep shovel to safe place. Dispose of this material and its container at hazardous or special waste collection point. This material and its container must be disposed of in a safe way. To clean the floor and all objects contaminated by this material, use water and detergent.

SAFE STORAGE WITH OTHER CLASSIFIED CHEMICALS



x — Must not be stored together

o — May be stored together with specific preventions

+ — May be stored together

Note: Depending on other risk factors, compatibility assessment based on the table above may not be relevant to storage situations, particularly where large volumes of dangerous goods are stored and handled. Reference should be made to the Safety Data Sheets for each substance or article and risks assessed accordingly.

Chemwatch: 80-9381

Print Date:

27/11/2023

Issue Date:

04/02/2020

This document is copyright. Apart from any fair dealing for the purposes of private study, research, review or criticism, as permitted under the Copyright Act, no part may be reproduced by any process without written permission from CHEMWATCH. TEL (+61 3) 9572 4700.

Appendix IV: Step-By-Step Derivation of the Analytical Model "Model 1"

$$\nabla \cdot \mathbf{E} = -\frac{\partial B}{\partial t} = \oint \mathbf{E} \cdot d\mathbf{l} = -\frac{d}{dt} \iint \mathbf{B} \cdot d\mathbf{A}$$

- $\oint \mathbf{E} \cdot d\mathbf{l}$ → Line integral of the electric field around the closed loop. Also known as the electric field induced in the loop
- $-\frac{d}{dt} \iint \mathbf{B} \cdot d\mathbf{A}$ → time derivative of the magnetic flux. The magnetic flux through a closed loop bound a surface. "dA".

1. Determine the heat production by multiplying the current density with the resistance heat production. This is the heat production per meter. Now we can calculate the power density $\varepsilon = j(t)^2 \cdot \rho$

2. Derive the formula for the current density

$$j(t) = E(t) \cdot \sigma = \sigma \cdot \left(-\frac{r}{2} \cdot \frac{d}{dt} (\mu_0 j(t) t_t + B_0 \cdot \sin(\omega t)) \right) =$$

$$\frac{d}{dt} \left(-\left(\frac{\sigma r \mu_0 t_t}{2} \right) \cdot j(t) - \left(\frac{B_0 \sigma r}{2} \right) \sin(\omega t) \right) = C_1 \frac{dj(t)}{dt} - C_2 \omega \cos(\omega t)$$

$$C_1 = \frac{\mu_0 \sigma r t_t}{2}, C_2 = \frac{B_0 \sigma r}{2}$$

$C_1 \frac{dj(t)}{dt} + j(t) = -C_2 \omega \cos(\omega t) \rightarrow$ first order differential equation \rightarrow Solve with integrating factor

$$\mu(t) = e^{\int \frac{1}{C_1} dt} = e^{\frac{t}{C_1}} \rightarrow \text{integrating factor}$$

$$e^{\frac{t}{C_1}} \left(C_1 \frac{dj(t)}{dt} + j(t) \right) = -C_2 e^{\frac{t}{C_1}} \omega \cos(\omega t)$$

$$\frac{d}{dt} v \cdot u = u \frac{dv}{dt} + v \frac{du}{dt}, u = e^{\frac{t}{C_1}}, v = j(t)$$

$$\frac{d}{dt} \left(e^{\frac{t}{C_1}} + j(t) \right) = -C_2 e^{\frac{t}{C_1}} \omega \cos(\omega t)$$

$$\int \frac{d}{dt} \left(e^{\frac{t}{C_1}} + j(t) \right) dt = \int -C_2 e^{\frac{t}{C_1}} \omega \cos(\omega t) dt$$

$$e^{\frac{t}{C_1}} j(t) = -\frac{C_1 C_2 \omega^2 e^{\frac{t}{C_1}} \sin(\omega t)}{C_1^2 \omega^2 + 1} - \frac{C_2 \omega e^{\frac{t}{C_1}} \omega \cos(\omega t)}{C_1^2 \omega^2 + 1} + C$$

$$j(t) = -\frac{C_1 C_2 \omega^2 \sin(\omega t)}{C_1^2 \omega^2 + 1} - \frac{C_2 \omega \cos(\omega t)}{C_1^2 \omega^2 + 1} + C e^{-\frac{t}{C_1}}$$

$$j(t) = -\frac{C_1 C_2 \omega^2 \sin(\omega t)}{C_1^2 \omega^2 + 1} - \frac{C_2 \omega \cos(\omega t)}{C_1^2 \omega^2 + 1} + C e^{-\frac{t}{C_1}}, \text{if } t \rightarrow \infty, \text{ then } C e^{-\frac{t}{C_1}} \rightarrow 0$$

Find the amplitude and phase.

$$j(t) = -\frac{C_2\omega}{C_1^2\omega^2 + 1}(C_1\omega \sin(\omega t) + \cos(\omega t))$$

Write in the form $R \cdot \cos(\omega t + \varphi)$, where "R" Is the Amplitude, and " φ " the Phase shift

$$j(t) = -\frac{C_2\omega}{C_1^2\omega^2 + 1}(C_1\omega \sin(\omega t) + \cos(\omega t))$$

$R = \text{sgn}(a) \cdot \sqrt{a^2 + b^2} \rightarrow$ where R is the amplitude

$\varphi = \tan^{-1}\left(-\frac{b}{a}\right) \rightarrow$ where " φ " Is the phase shift

$\text{sgn}(a) = -1 \rightarrow$ if $a < 0$

$\text{sgn}(a) = 1 \rightarrow$ if $a > 0$

$$R = \text{sgn}\left(\frac{C_1C_2\omega^2}{C_1^2\omega^2 + 1}\right) \cdot \sqrt{\left(-\frac{C_1C_2\omega^2}{C_1^2\omega^2 + 1}\right)^2 + \left(-\frac{C_2\omega}{C_1^2\omega^2 + 1}\right)^2}$$

$$\varphi = \tan^{-1}\left(\frac{\frac{C_2\omega}{C_1^2\omega^2 + 1}}{\frac{C_1C_2\omega^2}{C_1^2\omega^2 + 1}}\right)$$

$a \cdot \cos(x) + b \cdot \sin(x) = R \cdot \cos(x + \varphi)$

$$j(t) = \text{sgn}\left(\frac{C_1C_2\omega^2}{C_1^2\omega^2 + 1}\right) \cdot \sqrt{\left(-\frac{C_1C_2\omega^2}{C_1^2\omega^2 + 1}\right)^2 + \left(-\frac{C_2\omega}{C_1^2\omega^2 + 1}\right)^2} \cdot \cos\left(\omega t + \tan^{-1}\left(\frac{\frac{C_2\omega}{C_1^2\omega^2 + 1}}{\frac{C_1C_2\omega^2}{C_1^2\omega^2 + 1}}\right)\right) =$$

$$= \text{sgn}\left(\frac{C_1C_2\omega^2}{C_1^2\omega^2 + 1}\right) \cdot \sqrt{\frac{C_2^2\omega^2}{C_1^2\omega^2 + 1}} \cdot \cos(\omega t + \tan^{-1}(C_1\omega))$$

Substitute C_1 & C_2 in the final equation.

$$j(t) = \text{sgn}\left(\frac{C_1C_2\omega^2}{C_1^2\omega^2 + 1}\right) \cdot \sqrt{\frac{C_2^2\omega^2}{C_1^2\omega^2 + 1}} \cdot \cos(\omega t + \tan^{-1}(C_1\omega)) \rightarrow$$

$$j(t) = \text{sgn}\left(\frac{\left(\frac{\mu_0 \sigma r d}{2}\right) \left(\frac{B_0 \sigma r}{2}\right) \omega^2}{\left(\frac{\mu_0 \sigma r d}{2}\right)^2 \omega^2 + 1}\right) \cdot \sqrt{\frac{\left(\frac{B_0 \sigma r}{2}\right)^2 \omega^2}{\left(\frac{\mu_0 \sigma r d}{2}\right)^2 \omega^2 + 1}} \cdot \cos\left(\omega t + \tan^{-1}\left(\frac{\mu_0 \sigma r d \omega}{2}\right)\right)$$

$$j(t) = \text{sgn}\left(\frac{\mu_0 d B_0 \sigma^2 r^2 \omega^2}{\mu_0^2 \sigma^2 r^2 d^2 \omega^2 + 4}\right) \cdot \sqrt{\frac{B_0^2 \sigma^2 r^2 \omega^2}{\mu_0^2 \sigma^2 r^2 d^2 \omega^2 + 4}} \cdot \cos\left(\omega t + \tan^{-1}\left(\frac{\mu_0 \sigma r d \omega}{2}\right)\right)$$

3. Derive formula for the electric field $\rightarrow E(t) = -\frac{1}{2}r \frac{dB(t)}{dt}$

$$E(t) = -\frac{1}{2}r \frac{dB(t)}{dt} = -\frac{1}{2}r \frac{d}{dt}(\mu_0 j(t) t_h + B_0 \cdot \sin(\omega t))$$

$$\oint \mathbf{E} \cdot d\mathbf{l} = -\frac{d}{dt} \iint \mathbf{B} \cdot d\mathbf{A} = -\frac{d}{dt} \int \mathbf{B} \cdot d\mathbf{A}$$

$$\oint \mathbf{E} \cdot d\mathbf{l} \rightarrow E \int dl \rightarrow E = \text{uniform/constant}$$

$$\int dl = l = 2\pi r \rightarrow \text{for a circle, the circumference}$$

$$\oint \mathbf{E} \cdot d\mathbf{l} \rightarrow E2\pi r \rightarrow \text{for a cylinder}$$

$$-\frac{d}{dt} \iint \mathbf{B} \cdot d\mathbf{A} \rightarrow -\frac{d}{dt} B \iint d\mathbf{A} \rightarrow B = \text{uniform/constant}$$

$$\iint d\mathbf{A} = A = \pi r^2 \rightarrow \text{for a circle}$$

$$-\frac{d}{dt} \int \mathbf{B} \cdot d\mathbf{A} = -\frac{d}{dt} B \pi r^2 \rightarrow \text{for a circle}$$

$$E2\pi r = -\frac{d}{dt} B \pi r^2$$

$$E(t) = -\frac{1}{2}r \frac{dB}{dt}$$

4. Derive formula for the magnetic field $\rightarrow B(t) = \mu_0 j(t) t_t + B_0 \cdot \sin(\omega t)$

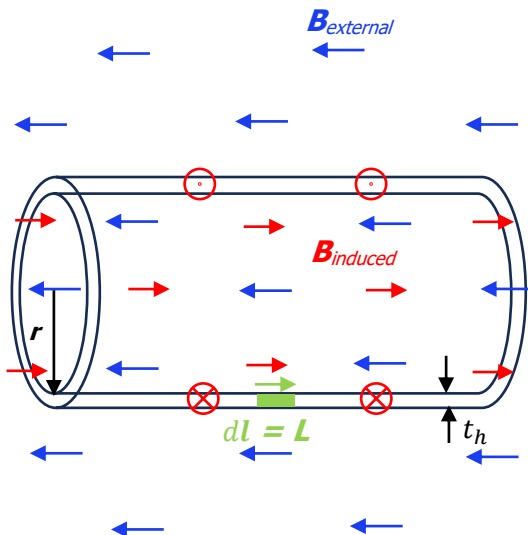
$$B(t) = B_{\text{induced}} + B_{\text{external}}$$

$$\oint \mathbf{B}_{\text{induced}} \cdot d\mathbf{l} = \mu_0 \iint \mathbf{j} \cdot d\mathbf{A}$$

$$B_{\text{induced}} \cdot L = \mu_0 j(t) t_t L$$

$$B_{\text{induced}} = \mu_0 j(t) t_t$$

$$B_{\text{external}} = B_0 \cdot \sin(\omega t)$$



Appendix V: Analytical "Model 1" Python Code

```
import numpy as np
import sympy as sm
import sympy.physics.mechanics as me
from scipy.integrate import quad
import pandas as pd

# Define print settings
me.init_vprinting(use_latex='mathjax')

# Create an empty list to store the data
data = []

# Define symbols
t = me.dynamicsymbols._t
sigma, rho, C, k, x = sm.symbols('sigma rho C k x')

# Define constants
r_outer = 0.002 #outer radius of the tube [m]
r_inner = 0.0015 # inner radius of the tube [m]
r_tube = (r_outer + r_inner)/2 # average radius of tube in [m]
d = 0.0005 # thickness of tube in [m]
L = 0.04 # length of the tube in [m]
volume_specimen = np.pi * (r_outer**2 - r_inner**2) * L # volume of
the specimen in [m^3]
t_exp = 300 # exposure time in [s]
mu_0 = 4e-7 * np.pi # permeability of free space [N/A^2]

# Surrounding medium constants
C_water = 4184 # specific heat capacity of water in [J/(kg*K)]
density_water = 998.2 # [kg/m^3]
volume_water = 3.15e-6 # volume of water in [m^3]
mass_water = density_water * volume_water # mass of the water in
[kg]

# Materials properties
materials = [
    {'name': 'Copper SFCu - ECu', 'sigma': 1/(2.14e-8), 'rho': 8683,
     'C': 385, 'k': 388},
    {'name': 'Low Carbon Steel ST37', 'sigma': 1/(1.54e-7), 'rho':
     7892, 'C': 461, 'k': 76.2},
    {'name': 'Stainless Steel 316L', 'sigma': 1/(7.48e-7), 'rho':
     7942, 'C': 500, 'k': 16.3},
    {'name': 'Ti grade 2', 'sigma': 1/(4.64e-7), 'rho': 4614, 'C':
     523, 'k': 16.4},
]

frequencies = [103.5e3, 155.3e3, 262.7e3, 371.6e3, 601.6e3] #
frequencies in [Hz]
Field_strengths = [2e-3, 4e-3, 8e-3] # field strengths in [T]

# Loop over materials, frequencies, and field strengths
for material in materials:
    for freq in frequencies:
```

```

for B_0 in Field_strengths:
    sigma_val = material['sigma']
    rho_val = material['rho']
    C_val = material['C']
    k_val = material['k']

    omega = 2 * np.pi * freq
    Critical_Frequency = 2/(mu_0 * sigma_val * d *
r_tube)/2*np.pi
    # Calculate current density
    j = -(B_0 * sigma_val * r_tube * 0.5 * omega) / (((mu_0
* sigma_val * r_tube * d * 0.5)**2) * omega**2 + 1)**0.5) *
sm.cos(omega * t + sm.atan(-1 / mu_0 * sigma_val * r_tube * d * 0.5
* omega))
    # Calculate power density
    p = (j**2) / sigma_val
    # Calculate average power density
    p_av = (sm.integrate(p, (t, 0, t_exp))) / t_exp
    # Calculate power of specimen
    P_spec = p_av * volume_specimen
    # Calculate the energy produced by the specimen
    E_spec = P_spec * t_exp
    # Calculate the temperature rise of the specimen
including the water surrounding it
    dT_min = E_spec / ((C_val * volume_specimen * rho_val) +
(C_water * mass_water)) # minimal temperature increase

    # Append numerical results to data list including
Critical_Frequency
    data.append([material['name'], float(sigma_val),
float(E_spec), float(P_spec), float(dT_min), freq / 1000, B_0 *
1000, float(Critical_Frequency)])

    # Print statement with formatted Critical Frequency
    print("{:<25} {:<15.2e} {:<20} {:<20} {:<20} {:<20.1f}
{:<20.1f} {:<20.2f}".format(material['name'], sigma_val, '%.2f' %
E_spec, '%.2f' % P_spec, '%.2f' % dT_min, freq / 1000, B_0 * 1000,
Critical_Frequency))

# Create dataframe
df = pd.DataFrame(data, columns=["Material", "Sigma", "Energy (J)",
"Average Power (W)", "Temperature Rise (°C)", "Frequency (kHz)",
"Field Strength (mT)", "Critical Frequency"])

# Write and save the Excel file
with pd.ExcelWriter('Specimen_data.xlsx', engine='openpyxl') as
writer:
    df.to_excel(writer, index=False, sheet_name='Specimen Data')

print("Data exported to Excel sheet successfully.")

```

Appendix VI: FreeFem++ Code

```
// ***** FreeFEM++ Simple electrostatic problem *****
// Induced current in hollow cylinder with uniform oscillating field
// parallel to long axis
// http://www.freefem.org/ff++/ for software and manual
// Simplest way to run is from command line:
// $ FreeFem++ electrostatic_example.edp
// Also interactive environments exist, try FreeFem-cs for example.
// Leon Abelmann, Apr 2024
// *****

// ***** Geometry definition *****
// Dimensions of problem
// Simulation area, cylindrical coordinates
real h0 = 60; //height (mm)
real r0 = 20; // radius (mm)

// Cylinder
real h = 40; // Height of cylinder (mm)
real ri = 1.5; // Radius of inner wall of cylinder (mm)
real ro = 2.0; // Radius of outer wall
real sigma = 1/(4.64e-7); // Conductivity of CP Ti Gr.2 (1/Ohm.m)
real B0 = 2e-3; // Uniform magnetic field B0*exp(i*omega*t)
real omega = 601e3*2*pi; // Drive frequency in rad/s

// Simulation parameters
real s = 15; // Mesh refinement
wait = false;

// Auxliliary variables
real mu0 = (4e-7)*pi;
real k = omega*sigma*mu0 * 1e-6; // mu0*sigma*omega in /mm2

// Define simulation area
// The lines are parameterized with variable t, the direction is
important!
border bottom(t = 0 , r0 ) { x = t ; y = -h0/2 ; }
border right( t = -h0/2 , h0/2 ) { x = r0 ; y = t ; }
border top( t = r0 , 0 ) { x = t ; y = h0/2 ; }
border left( t = h0/2 , -h0/2 ) { x = 0 ; y = t ; }

// Cylinder wall has own area to allow for integration of A over
wall
border cbottom(t = ri , ro ) { x = t ; y = -h/2 ; }
border cright( t = -h/2 , h/2 ) { x = ro ; y = t ; }
border ctop( t = ro , ri ) { x = t ; y = h/2 ; }
border cleft( t = h/2 , -h/2 ) { x = ri ; y = t ; }

// Show simulation border
// wait: user has to hit return in output graph
// Type ? in graph window to access keyboard/mouse shortcuts (manual
page 166)
plot(bottom(s*r0)+right(s*h0) + top(s*r0) + left(s*h0))
```

```

+ cbottom(s*(ro-ri))+cright(s*h)
+ ctop(s*(ro-ri)) + cleft(s*h), wait=wait, ps="borders.eps");

// Mesh the simulation area
// Just mesh everything if you don't need to integrate A over wall:
//mesh Th = buildmesh(bottom(s*r0)+right(s*h0) + top(s*r0) +
left(s*h0));
// Mesh everything outside cylinder wall (note - sign):
mesh Th1 = buildmesh(bottom(s*r0)+right(s*h0) + top(s*r0) +
left(s*h0)
                + cbottom(-s*(ro-ri))+cright(-s*h)
                + ctop(-s*(ro-ri)) + cleft(-s*h));
// Mesh cylinder wall:
mesh Th2 = buildmesh(cbottom(s*(ro-ri))+cright(s*h)
                + ctop(s*(ro-ri)) + cleft(s*h));
// Combine both meshes
mesh Th = Th1 + Th2;

// Show mesh
plot(Th, wait=wait, ps="mesh.eps");

// Define finite elements
fespace Vh(Th,P1);          // P1 FE-space (See manual 6.3)

// Define conductivity of cylinder with parameter k
// (outside cylinder sigma=0, so k=0)
func f = k * (x < ro)*(x > ri)*(y < h/2)*(y > -h/2);
Vh kappa = f;
//Show kappa constant
plot(kappa, fill=true, wait=wait, ps="kappa.eps");

// ***** Induction problem
// *****
// Define problem
Vh<complex> A,vh; // potential A and test function vh.
problem Induction(A,vh) = // definition of the problem
    int2d(Th) (dx(A)*dx(vh)*x + dy(A)*dy(vh)*x + (A*vh)/x) // del x del
x A
    + int2d(Th) ( 1i*kappa*A*vh*x ) // induced current
    - int1d(Th, right) (r0*(B0/2)*vh) // uniform background field B=B0
    + on(left, A = 0); // ground somewhere

// ***** Solve
// *****
// Run FE simulation
Induction;

// // ***** Analyse output
// *****

// Plot vector field A
Vh Areal = real(A), Aimag=imag(A), Aabs=abs(A);
//plot(Areal, wait=true);
//plot(Aimag, wait=true);
plot(Aabs, wait=wait, ps="Aabs.eps");

```

```

// Rotation in cylindrical coordinates
fespace Vi(Th,P1);
func rotAr = -dy(A)(x,y);
func rotAz = (x>0) ? (1/x)*A(x,y) + dx(A)(x,y) : 2*dx(A)(x,y);

// Plot abs value of vector field B = rot(A)
Vi<complex> Br=rotAr(x,y), Bz=rotAz(x,y);
plot([Br,Bz], coef=0.1, wait=wait); // coef: vector length

// Quantitative analysis and checks:
cout << "*****" << endl
<< endl;

// Print field at some location
real r = ri-0.01;
real z = 0;
cout << "at (r,z) = (" << r << " , "<< z << ") Bz = " << Bz(r,z) <<
endl;

r = ro+0.01;
cout << "at (r,z) = (" << r << " , "<< z << ") Bz = " << Bz(r,z) <<
endl ;

r = ri+(ro-ri)/2;
z = 0;
cout << "at (r,z) = (" << r << " , "<< z << ") Ain = " << A(r,z) <<
endl<< endl;

cout << "Check for very thin wall:" << endl << endl;
// Check if B agrees with j, oint(B.dl) = mu0*int2d(j.d0):
complex Bin = Bz(ri-0.1,0);
complex Bout = Bz(ro+0.1,0);
complex Ain = A(ri+(ro-ri)/2,0); // A in center of cylinder wall
complex Aav = int2d(Th2)(A) / ((ro-ri)*h); // Average A over
cylinder wall
cout << "These should be close: " << endl;
cout << "Ain : " << Ain << endl;
cout << "Aav : " << Aav << endl << endl;

cout << "These should be close: " << endl;
cout << "Oint(B) = Bout - Bin : " << (Bin - Bout) << endl;
cout << "j*t = -i kappa Ain t : " << -1i*k*Ain*(ro-ri) << endl;
cout << "j*t = -i kappa Aav t : " << -1i*k*Aav*(ro-ri) << endl;

cout << endl << "*****"
<< endl;

// Write potential to file
{
  ofstream gnu("FreeFemA.csv");
  real n=100;
  real t;
  // Column headers
  gnu << "r, Areal, Aimag, Aabs" << endl;
  // Simulation parameters

```

```

gnu << "# kappa: " << k << " , s: " << s << " , B0: " << B0 <<
endl;
// Data, comma separated
for (int i=0; i<=n; i++)
{
    t = (i/n) * r0;
    gnu << t << " , " << real(A(t,0)) << " , " << imag(A(t,0)) << "
, " << abs(A(t,0)) << endl;
}
}

cout << "Press ESC in graph area to quit" << endl;

// For unix-savvy: this is how you call gnuplot from inside freefem
// See manual 7.2
// exec("echo 'set datafile separator comma \
// plot \"plot.csv\" using 1:2 w p title \"real\", \"plot.csv\"
using 1:3 w p title \"imag\" \
// pause 5 \
// set term post eps \
// set output \"gnuplot.eps\" \
// replot \
// set output \
// quit' | gnuplot");

```


Appendix VII: Source Code Calculating and Plotting Vector Potential "Model 1"

```
#!/usr/bin/env python3
#####
# CompareVectorPotential
# Use: ./CompareVectorPotential <file.csv>
# Plot vector potentials and compare to output of FreeFEM++
calculations
# located in <file.csv>
# Generates <file>.pdf output file
# Leon Abelmann, April 2024
#####
import sys # Enable reading parameters from command line
from pathlib import Path # To handle filenames from arg list

# Numerical Libraries
import numpy as np
from numpy import pi, sqrt
# from scipy.special import jv, yv

# Plotting:
import matplotlib
import matplotlib.pyplot as plt
from matplotlib.ticker import (MultipleLocator, AutoMinorLocator)

# Vector field calculation for infinitely long hollow cylinder
from hollowcyl import Aphi, AphiThin

# Parameters used for the comparison with the analytical solution:

R1 = 1.5e-3          # Inner diameter hollow cylinder in m
R2 = 2.0e-3          # Outer diameter
sigma = 1 / (4.64e-7) # Conductance of CP Ti Gr.2 in 1/Ohm.m
omega = 601e3 * 2 * pi # Frequency of applied magnetic field in
rad/s
Bapp = 2e-3          # Applied magnetic field in T
d = 0.5e-3           # Example thickness or another relevant
parameter
mu0 = (4e-7)*pi      # Vacuum permeability
kappa = sqrt(-1j*mu0*sigma*omega)

mu0 = (4e-7)*pi      # Vacuum permeability
kappa = sqrt(-1j*mu0*sigma*omega)
print("Kappa : %g + j%g, abs:
%g"%(kappa.real,kappa.imag,np.abs(kappa)))
print("Kappa^2 : %g"%(np.abs(kappa)**2))

#####
# PlotComparison
# Generate graph
# Generates InfinitelyLongCylinder.pdf output file
#####
```

```

def PlotComparison():

    # Setup figure
    fig, ax1 = plt.subplots(nrows=1,ncols=1)
    fig.set_figwidth(4)
    fig.set_figheight(3)

    # Set up axes
    ax1.set_xlim(left = 0, right = 2.5)
    ax1.set_xlabel("r / mm", fontsize=12)
    ax1.xaxis.set_major_locator(MultipleLocator(0.5))
    ax1.xaxis.set_minor_locator(MultipleLocator(0.1))

    ax1.set_ylim(bottom=-0.001, top=0.002)
    ax1.set_ylabel("A $\{\_\phi\}$  / (mVs/m)", fontsize=12)
    ax1.yaxis.set_major_locator(MultipleLocator(0.0002))
    ax1.yaxis.set_minor_locator(MultipleLocator(0.0001))

    # Tics on all axes
    ax1.tick_params(which='both',top=True,right=True)

    # Horizontal line at y = 0
    plt.axhline(linewidth=0.5, color='k')

    # Vertical line at x = R1 and R2
    plt.axvline(x = R1*1000, linewidth=0.5, color='k')
    plt.axvline(x = R2*1000, linewidth=0.5, color='k')

    #Text instead of legend
    plt.text(4.5,0.6,"R $\_1$ ", fontsize=12)
    plt.text(4.5,0.2,"R $\_2$ ", color = "r", fontsize=12)

    # For model lines
    x = np.arange(0.01e-3,2.5e-3,0.01e-3)

    # Plot analytical for infinitely long hollow cylinder
    plt.plot(x*1000, (1000*Aphi(x, kappa, R1, R2, Bapp)).real, 'k',
             linewidth=1, label="finite wall tichkness Real")
    plt.plot(x*1000, (1000*Aphi(x, kappa, R1, R2, Bapp)).imag, 'r',
             linewidth=1, label="finite wall tichkness Imag")
    plt.plot(x*1000, (1000*abs(Aphi(x, kappa, R1, R2, Bapp))), 'b',
             linewidth=1, label="finite wall tichkness")

    # Plot approximation for infinitely long thin-walled cylinder
    k = mu0*sigma*omega
    plt.plot(x*1000, (1000*AphiThin(x, k, R1, R2-R1, Bapp)).real,'k-
- ',
             linewidth=1, label="infinite wall tichkness Real")
    plt.plot(x*1000, (1000*AphiThin(x, k, R1, R2-R1, Bapp)).imag,
'r--',
             linewidth=1, label="infinite wall tichkness Imag")
    plt.plot(x*1000, (1000*abs(AphiThin(x, k, R1, R2-R1, Bapp))),
'b--',
             linewidth=1, label="infinite wall tichkness Abs")

    # Plot legend

```

```
plt.legend(fontsize=14)

# Make sure everything fits
fig.tight_layout()

# Show on screen and/or pdf file
plt.show()
plt.savefig("InfinitelyLongCylinder.pdf", format="pdf")

PlotComparison()
```

Appendix VIII: Source Code Calculating and Plotting the Vector Potential of Various Models

```
#!/usr/bin/env python3
#####
#####
# CompareVectorPotential
# Use: ./CompareVectorPotential <file.csv>
# Plot vector potentials and compare to output of FreeFEM++
calculations
# located in <file.csv>
# Generates <file>.pdf output file
# Leon Abelmann, April 2024
#####
#####
import sys # Enable reading parameters from command line
from pathlib import Path # To handle filenames from arg list

# Numerical Libraries
import numpy as np
from numpy import pi, sqrt
# from scipy.special import jv, yv

# Plotting:
import matplotlib
import matplotlib.pyplot as plt
from matplotlib.ticker import (MultipleLocator, AutoMinorLocator)

# Vector field calculation for infinitely long hollow cylinder
from hollowcyl import Aphi, AphiSolid

# Parameters used for the comparison with the analytical solution:
R1 = 1.5e-3 # Inner diameter hollow cylinder in m
R2 = 2.0e-3 # Outer diameter
sigma = 1 / (4.64e-7) # Conductance of CP Ti Gr.2 in 1/Ohm.m
omega = 601e3 * 2 * pi # Frequency of applied magnetic field in
rad/s
Bapp = 2e-3 # Applied magnetic field in T
d = 0.5e-3 # Example thickness or another relevant parameter
mu0 = (4e-7)*pi # Vacuum permeability
kappa = sqrt(-1j*mu0*sigma*omega)

#####
#####
# PlotComparison
# Generate graph
# filename : FreeFEM++ output file in csv format
# Generates <filename>.pdf output file
#####
#####
def PlotComparison(filename):
    # Load data from simulation
    data = np.genfromtxt(filename, delimiter=",", comments="#",
names=True)
    # print(data)
```

```

r = data['r']
Areal = data['Areal']
Aimag = data['Aimag']
Aabs = np.sqrt(Areal**2 + Aimag**2)

# Setup figure
fig, ax1 = plt.subplots(nrows=1, ncols=1)
fig.set_figwidth(4)
fig.set_figheight(3)

# Set up axes
ax1.set_xlim(left=0, right=2.5)
ax1.set_xlabel("r / mm", fontsize=12)
ax1.xaxis.set_major_locator(MultipleLocator(0.5))
ax1.xaxis.set_minor_locator(MultipleLocator(0.1))

ax1.set_ylim(bottom=-0.001, top=0.002)
ax1.set_ylabel("A $\{\_phi\}$  / (mVs/m)", fontsize=12)
ax1.yaxis.set_major_locator(MultipleLocator(0.0002))
ax1.yaxis.set_minor_locator(MultipleLocator(0.0001))

# Tics on all axes
ax1.tick_params(which='both', top=True, right=True)

# Horizontal line at y = 0
plt.axhline(linewidth=0.5, color='k')

# Vertical line at x = R1 and R2
plt.axvline(x=R1*1000, linewidth=0.5, color='k')
plt.axvline(x=R2*1000, linewidth=0.5, color='k')

# For model lines
x = np.arange(0.01e-3, 2.5e-3, 0.01e-3)

# Plot analytical
plt.plot(x*1000, (1000*Aphi(x, kappa, R1, R2, Bapp)).real, 'k',
linewidth=1, label="finite wall thickness Real")
plt.plot(x*1000, (1000*Aphi(x, kappa, R1, R2, Bapp)).imag, 'r',
linewidth=1, label="finite wall thickness Imag")
plt.plot(x*1000, (1000*abs(Aphi(x, kappa, R1, R2, Bapp))), 'b',
linewidth=1, label="finite wall thickness Abs")

# Plot analytical for solid
plt.plot(x*1000, (1000*AphiSolid(x, kappa, R2, Bapp)).real,
'k:', linewidth=1, markersize=1, label="Solid Cylinder Real")
plt.plot(x*1000, (1000*AphiSolid(x, kappa, R2, Bapp)).imag,
'r:', linewidth=1, markersize=1, label="Solid Cylinder Imag")
plt.plot(x*1000, (1000*abs(AphiSolid(x, kappa, R2, Bapp))),
'b:', linewidth=1, markersize=1, label="Solid Cylinder Abs")

# Plot simulation results
plt.errorbar(r, Areal, xerr=0, yerr=0, label='FEM Real',
fmt='k', linestyle='', marker='s', markersize=1, elinewidth=1,
capsize=2, capthick=1)

```

```

plt.errorbar(r, Aimag, xerr=0, yerr=0, label='FEM Imag',
fmt='r', linestyle='', marker='s', markersize=1, elinewidth=1,
capsize=2, capthick=1)
plt.errorbar(r, Aabs, xerr=0, yerr=0, label='FEM Abs', fmt='b',
linestyle='', marker='s', markersize=1, elinewidth=1, capsize=2,
capthick=1)

# Plot legend
plt.legend(fontsize=14)

# Make sure everything fits
fig.tight_layout()

# Show on screen and/or pdf file
# plt.show()
plt.savefig(filename.with_suffix('.pdf'), format="pdf")

if __name__ == "__main__":
    filename = Path(sys.argv[1]) if len(sys.argv) > 1 else
Path("FreeFemA.csv")
    print("Processing", filename)
    PlotComparison(filename)

for arg in sys.argv[1:]:
    # Get filename with path and extension
    filename = Path(str(arg))
    print("Processing ", filename)
    PlotComparison(filename)

```